Wp-1 reference cases of laminar and turbulent interactions

Dussauge, Jean Paul; Bur, Reynald; Davidson, Todd; Babinsky, Holger; Bernardini, Matteo; Giepman, Rogier; Schrijer, Ferry; Oudheusden, Bas van; Sidorenko, Andrey; More Authors

DOI
10.1007/978-3-030-47461-4_2

Publication date
2021

Document Version
Final published version

Published in
Transition Location Effect on Shock Wave Boundary Layer Interaction

Citation (APA)
Dussauge, J. P., Bur, R., Davidson, T., Babinsky, H., Bernardini, M., Giepman, R., Schrijer, F., Oudheusden, B. V., Sidorenko, A., & More Authors (2021). Wp-1 reference cases of laminar and turbulent interactions. In P. Doerffer (Ed.), *Transition Location Effect on Shock Wave Boundary Layer Interaction* (pp. 25-127). (Notes on Numerical Fluid Mechanics and Multidisciplinary Design; Vol. 144). SpringerOpen. https://doi.org/10.1007/978-3-030-47461-4_2

WP-1 Reference Cases of Laminar and Turbulent Interactions

Jean-Paul Dussauge, Reynald Bur, Todd Davidson, Holger Babinsky, Matteo Bernardini, Sergio Pirozzoli, Pierre Dupont, Sébastien Piponniau, Lionel Larchevêque, Rogier Giepman, Ferry Schrijer, Bas van Oudheusden, Pavel Polivanov, Andrey Sidorenko, Damien Szubert, Marianna Braza, Ioannis Asproulias, Nikos Simiriotis, Jean-Baptiste Tô, Yannick Hoarau, Andrea Sansica, and Neil Sandham

Abstract In order to be able to judge the effectiveness of transition induction in WP-2, reference flow cases were planned in WP-1. There are two obvious reference cases—a fully laminar interaction and a fully turbulent interaction. Here it should be explained that the terms "laminar" and "turbulent" interaction refer to the boundary layer state at the beginning of interaction only. There are two basic configurations of shock wave boundary layer interaction and these are a part of the TFAST project. One is the normal shock wave, which typically appears at the transonic wing and on the turbine cascade. The characteristic incipient separation Mach number range is about $M = 1.2$ in the case of a laminar boundary layer and about $M = 1.32$ in the case of turbulent boundary layer. The second typical flow case is the oblique shock wave reflection. The most characteristic case in European research is connected to the 6th FP IP HISAC project concerning a supersonic business jet. The design speed of this airplane is $M = 1.6$. Therefore the TFAST consortium decided to use this Mach number as the basic case. Pressure disturbance at this Mach number is not very

J.-P. Dussauge (✉) · P. Dupont · S. Piponniau · L. Larchevêque
Aix-Marseille University, CNRS, IUSTI, Marseille, France
e-mail: jean-paul.dussauge@univ-amu.fr

R. Bur
Office National d'Etudes et de Recherches Aérospatiales, Meudon, France

T. Davidson · H. Babinsky
University of Cambridge, Cambridge, UK

M. Bernardini · S. Pirozzoli
University of Rome, La Sapienza, Rome, Italy

R. Giepman · F. Schrijer · B. van Oudheusden
Delft University of Technology, Aerodyn. Lab., Delft, The Netherlands

P. Polivanov · A. Sidorenko
Russian Academy of Sciences, Siberian Branch, Inst.of Theor. App. Mech., Novosibirsk, Russia

D. Szubert · M. Braza · I. Asproulias · N. Simiriotis · J.-B. Tô · Y. Hoarau
Institut de Mécanique des Fluides de Toulouse, UMR 5502 CNRS-INPT-UT3, Toulouse, France

A. Sansica · N. Sandham
University of Southampton, Southampton, UK

P. Doerffer et al. (eds.), *Transition Location Effect on Shock Wave Boundary Layer Interaction*, Notes on Numerical Fluid Mechanics and Multidisciplinary Design 144,
https://doi.org/10.1007/978-3-030-47461-4_2

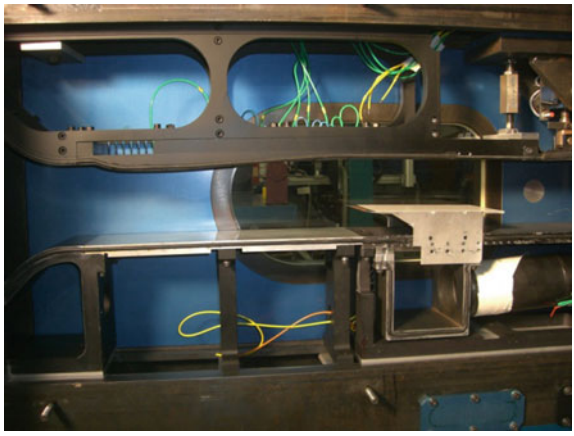

Fig. 1 Test set-up with the Mach 1.3 half nozzle in the S8Ch wind tunnel (w/o shock generator wedge)

high and can be compared to the disturbance of the normal shock at the incipient separation Mach number mentioned earlier. As mentioned earlier, shock reflection at M = 1.6 may be related to incipient separation. Therefore two additional test cases were planned with different Mach numbers. ITAM conducted an M = 1.5 test case, and TUD an M = 1.7 test case. These partners have also previously made very specialized and successful contributions to the UFAST project.

1 Normal Shock Wave

1.1 Test Section Design and Construction

1.1.1 ONERA M = 1.3

A test set-up has been manufactured to study the effect of a normal shock on the boundary layer transition process. Figure 1 shows the test set-up with the Mach 1.3 half nozzle configuration in the S8Ch wind tunnel. This half nozzle configuration (compared to the full nozzle one for the Mach 1.6 case) is imposed by the characteristics of the wind tunnel pumps: $Q = f(\Delta p)$.

1.1.2 UCAM M = 1.3

Supersonic Wind Tunnel
Experiments were conducted in the CUED No. 1 Supersonic Tunnel (pictured in Fig. 2), an intermittent blow-down facility with run times up to 30 s, a working section 179 mm high & 114 mm wide and capable of operating at Mach numbers between 0.5 and 3.5. Free-stream Reynolds numbers are between 13 and 55 million

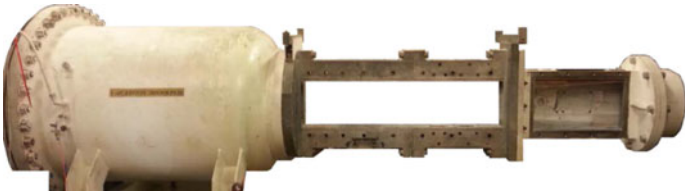

Fig. 2 CUED No. 1 SST, showing the settling chamber, working section and first diffuser

per metre, with the stagnation pressure measured in the settling chamber and manually kept constant by trained technicians, with <0.1% fluctuation. The stagnation temperature (measured as the average of four T-type thermocouples in the settling chamber) increases during a typical run from around 294 K to 300 K. The free-stream turbulence level of the tunnel in transonic mode was measured as 0.7% at Mach 0.7 (WP-5) and 0.5% at Mach 0.8 (WP-1&2) [1].

Experimental methods

A 'Z-type' schlieren system with a horizontal knife-edge is used to visualise the flow, with high frame rate images captured by a Photron FASTCAM ultima APX high speed camera. Imperfections in the optical path are removed by subtracting a 'wind off' background image from each 'wind on' picture. Variation in intensity along a row of pixels for each frame is used to extract shock position versus time, and the fluctuation throughout a run is analysed to measure any oscillation amplitudes and frequencies.

Pressures are recorded with small tappings in the walls and test models connected to a NetScanner 9116 pressure transducer system with a quoted accuracy of 0.05%. The total experimental error of measured pressures is then <0.2%, and as such the error in calculated Mach numbers is <0.5%. A greater contribution to inaccuracy in Mach number is slight fluctuations in free-stream conditions, which for the most unsteady flows can result in r.m.s. variations of ± 0.03. Surface pressure data can be taken over a wide area by using pressure sensitive paint (PSP). When illuminated with UV, the paint luminesces with an intensity related to surface pressure. An ISSI LM2x-400 serves as the light source, with images taken by an Apogee Alta U2000 cooled CCD camera. The intensity also varies with the thickness of the paint layer, so 'wind on' images are referenced to 'wind off' background images to remove this dependency, and additional images are taken without UV to subtract any stray light. The relative intensity is then calibrated with pressure taps. The paint coat is rougher (Ra 0.8 μm) than the hand polished surface, and so causes the boundary layer to transition (evidenced by the lack of lambda structure seen in schlieren imaging).

A two-component laser Doppler velocimetry (LDV) system from TSI is used in forward-scatter mode to measure velocities. The current implementation uses a Coherent Innova 70C-5 Argon- Ion laser at 1.5 W, with beam wavelengths of 514.5 & 488 nm; an FBL-2 fiberlight box for beam manipulation, containing a 40 MHz Bragg cell; and a TR260 emitter with a TLN06-350 lens (focal length 363 mm), mounted so the measured vectors are at 45° to x & y and the lower beam pair is angled

slightly below horizontal. This lens is chosen for its small measurement volume, producing beam overlap waists of 90 & 85 μm for the two wavelengths respectively. The corresponding fringe spacings are 3.7 & 3.6 μm, and the beam overlap lengths are 1.3 & 1.2 mm (span-wise). A band pass filter of 40–120 MHz allows velocities from 0 m/s up to 300 & 284 m/s respectively to be measured. A TLN06-500 lens (focal length 512 mm) is used for the aerofoil wake traverses, where instantaneous velocities can frequently be negative, as at the maximum bandwidth setting (20–175 MHz) this allows velocities between-106/-100 & 712/675 m/s to be measured. This lens gives beam waists of 127 & 120 μm, with fringe spacings of 5.3 & 5.0 μm, and overlap lengths of 2.6 & 2.5 mm.

The receiving head is an RV70 with a 500 mm lens, mounted to point 11.25° down and 10° downstream which reduces reflections and decreases the effective length of the measurement volume. The receiver is connected to a PDM 1000-2 photo-detector box and an FSA 4000-2 frequency/burst spectrum analyser, with data recorded by TSI's FlowSizer software.

Droplets of paraffin, 0.5 μm in diameter (as determined by a shock-lag method), are injected through a rake in the settling chamber and provide good seeding levels around the centre-span, following the flow well. [2] In the free stream, valid burst rates are in the range of 25–40 kHz, although this drops dramatically in the boundary layer. Averages are taken over 0.2 s at each point of the traverse, which typically ensures at least 5,000 samples in the bulk flow. However, very near the wall (within a few dozen microns) this can fall as low as 500 per data point. Samples outside of three standard deviations are rejected for the purposes of determining the mean and r.m.s. velocities.

The manufacturer's quoted accuracy for the optics and burst analysis is 0.1%, but larger errors are present due to the physical geometries of the emitting head (for example, aligning the emitter with the flow and determining in the angle between the beams), which result in an estimated uncertainty of 1.5% for measured velocity components away from the wall [2]. Of greater impact are the difficulties in measuring the flow within a millimetre or so of the wall. Here, errant reflections contribute to a drop in signal-to-noise ratio; low seeding levels reduce particle counts and the accuracy of the measured mean and fluctuating velocities; velocity variation across the measurement volume can be significant in smaller boundary layers, giving increased scatter; and at the extreme end of the measurement range the volume can actually intersect with the floor, exacerbating all of these problems. As such, when the boundary layer thickness is under 0.5 mm (as is typical upstream of the shock in the clean cases), confidence in the data is much reduced and the technique is only trusted to give an indication of δ, and not expected to accurately determine profiles and integral parameters.

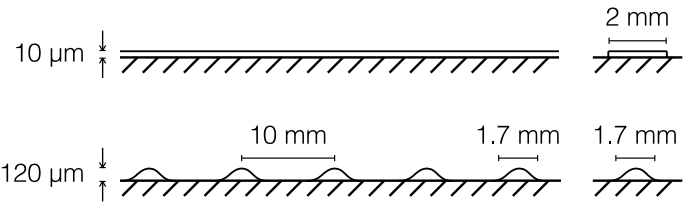

Fig. 3 Sketches of the two trip styles: (top) 2D trip—paint strip; (bottom) 3D trip—glue dots (mean values given); (left) stream-wise view; (right) span-wise view

Integral quantities (δ_i^*, θ_i & $H_i = \delta_i^*/\theta_i$) are important parameters in understanding the boundary layer health. Incompressible quantities are used here as they are less dependent on Mach number and so a better universal parameter, [3]. The resolution of LDV measurements is too low to integrate directly and so where the boundary layer is turbulent, profiles are fitted according to the theories of Sun & Childs [4] for the logarithmic law-of-the-wall & the Coles wake function; and of Musker [5] for the viscous sub-layer. For full details, see Davidson & Babinsky [6].

Two styles of trip were added to the models during the experimental campaigns, sketched in Fig. 3. The first is a two-dimensional step, created by a strip of gloss spray paint approximately 2 mm wide and 10 μm high. The second tripping method is three-dimensional and involves carefully applying drops of poly (vinyl acetate) glue at centre-span ($z = 0$) and then at 10 mm intervals along the span. Dot heights are between 90 and 180 μm with an average of 120 μm, and the diameters vary from $1.4 - 2.2$ mm with a mean of 1.7 mm.

Experimental configuration

The transonic test section used for the flat plate study is sketched in Fig. 4. The plate has a 6:1 elliptical profile around the leading edge, shaped by wire-erosion; is 12 mm thick; and was hand-polished to a surface roughness of Ra < 0.5 μm. The subsonic free-stream is accelerated by the curvature of the ellipse and a supersonic region develops around the leading edge of plate, terminated by a shock. The profile ensures a favourable pressure gradient (FPG) throughout the initial boundary layer development to maintain laminarity. The rest of the plate has a flat surface, to remove any effects of curvature from the SBLI. The plate has a slight angle of attack (∼+0.2°) to counteract the blockage effect of boundary layer growth along the tunnel side-walls and the floor below is cut away to avoid choking the flow.

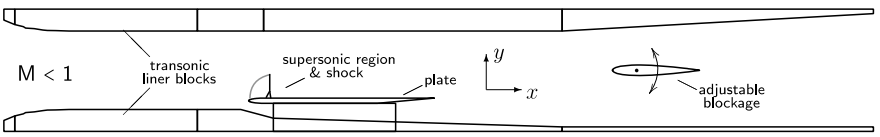

Fig. 4 Tunnel layout for the transonic flat plate investigation. The co-ordinate system is shown, with $x = 0$ at the leading edge, $y = 0$ at the plate's flat surface & $z = 0$ at centre-span

The experiment as first planned employed a sharp leading-edge plate mounted in a supersonic flow, with a shock-holding plate installed above, as sketched in Fig. 5. However, initial testing revealed that the boundary layer developing on the lower plate was turbulent, as detailed in Davidson & Babinsky (2014) [1], in spite of a very smooth surface finish. Natural transition is thought to have been promoted by instabilities arising as the flow negotiated the leading edge. Results from this configuration are discussed below as an example of a turbulent SBLI at similar Mach and Reynolds numbers to the transonic plate experiments.

A third plate was manufactured with a modified super-ellipse (MSE) profile around the leading edge. This shape, defined by Eq. (1) and sketched in Fig. 6a, avoids the discontinuity in curvature at the end of the ellipse (as shown in Fig. 6b) and so has had success in other experiments in further delaying natural transition and maintaining laminarity [7].

$$\left(\frac{y}{b}\right)^2 \tag{1}$$

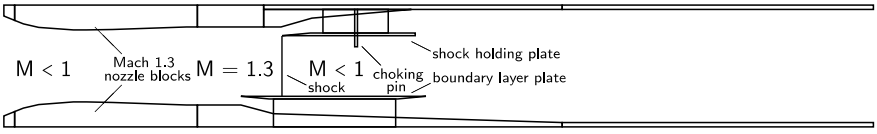

Fig. 5 The supersonic flat plate configuration that gave rise to the turbulent interaction

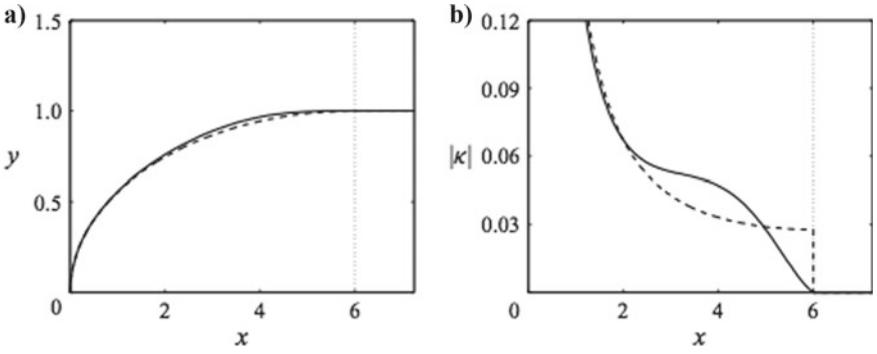

Fig. 6 Modified super-ellipse details: **a** Leading edge profiles for MSE (–) and ordinary ellipse (- -) shapes with an aspect ratio of 6. **b** Surface curvature. **c** Equation [7].

1.2 Experimental Investigation at Laminar and Turbulent Conditions

1.2.1 ONERA-DAFE (M = 1.3)

Tests of feasibility have been made on: (1) wind tunnel start; (2) control of the blockage effect only due to the flat plate, without the shock generator wedge into the test section. Figure 7 shows Schlieren visualizations for the natural boundary layer transition case. At the beginning of the tests, one has noticed the presence of humidity into the wind tunnel due to a failure of its drying device. A large quantity of particles of water leads to a strong modification of the flow pattern (see Fig. 7a): curvature of shock and waves, dissipation of the Mach wave at the leading edge of the flat plate. Moreover, one observes a blockage of the secondary flow, even if the suction device under the flat plate is active. So, one has to stop the tests in order to repair the drying device of the wind tunnel. The flow pattern has been improved when the atmospheric air is correctly desiccated but a blockage effect persists (see Fig. 7b). To suppress it, a suction device has been installed on the upper wall of the test section, above the flat plate: the shock moves downstream thanks to the suction, but stays into the test section far from the trailing edge of the flat plate, even for the maximum mass flow rate available.

At this nominal Mach number of 1.3, the theoretical ratio between the section of the exit nozzle plane and the throat section of the nozzle, A/A_{throat}, is equal to 1.07 (very close to 1). So, the presence of the flat plate (with a thickness of 3 mm) into the test section strongly contributes to the appearance of blockage, strengthened by the viscous effects. Moreover, it will be impossible to install the shock holder to generate the normal shock-wave. To conclude, the lack of power of the set of pumps avoids to successfully start the wind tunnel.

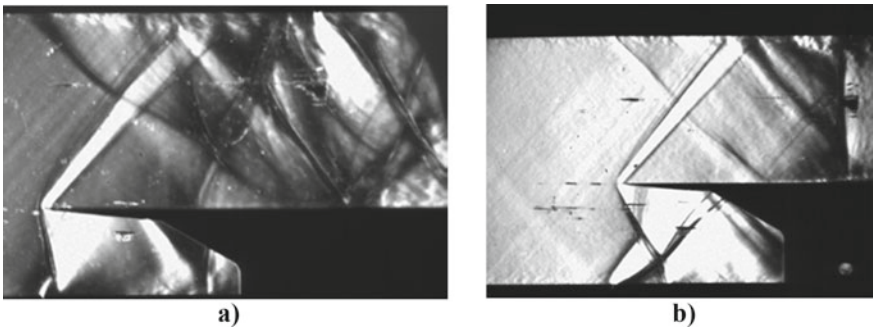

Fig. 7 Schlieren visualizations for the natural boundary layer transition case **a**—before reparation of the drying device, **b**—after reparation of the drying device

1.2.2 UCAM

Results

A schlieren image of the interaction on the clean transonic plate is shown in Fig. 8 (a). White expansion waves can be seen around the elliptical profile up to the start of the flat section of the plate (x = 36 mm, marked by a vertical white line on the image) as the flow accelerates up to supersonic speeds. Four millimetres downstream of this there is a dark wave (from x = 40 mm at the plate) which forms the front leg of a lambda shock structure (which has its intersection around y = 18 mm), implying the presence of a separation bubble, just as in Ackeret [8]. The rear leg of the shock structure appears stronger than the front leg, and is rotated back to point slightly downstream from the intersection. There is no secondary shock present, contrary to the observations of Ackeret et al., which suggests that it was induced by the curvature of the plate in that experiment and was not inherent to the laminar SBLI.

Measuring the wave angle at the end of the end of the expansion fan in the schlieren image predicts a Mach number around 1.16. A lambda shock has never been observed at a Mach number below 1.29 for a turbulent boundary layer [2], indicating that the boundary layer here ahead of the shock is laminar, or possibly transitional. The schlieren image also suggests that the boundary layer ahead of the shock is less than 1 mm thick, whereas the interaction is more than 10 mm long, and so several times larger, providing further confirmation that the boundary layer is not turbulent, as even separated turbulent interactions are rarely more than O (5δ) and attached turbulent interactions are typically even smaller [9, 10].

LDV can be employed to gather more information about the strength of the interaction. Figure 9a presents a traverse at 1 mm above the plate surface through the flow of Fig. 8a, which gives the shock Mach number as 1.18. Further traverses are built into a pressure contour map in Fig. 9b. Much as in Ackeret et al.'s total pressure survey, the front wave is much more smeared in quantitative measurements than in the schlieren image. The results indicate that Mach number drops to 1.14 through the first wave and from 1.11 down to 0.93 through the rear wave, giving nominal pressure rises of 5 & 23% in p/p_0 respectively.

This provides further evidence that the boundary layer is laminar or transitional, as it has only required a small pressure increase to separate, characteristic of laminar behaviour. In contrast, separated turbulent interactions have a larger pressure jump across the leading shock leg due to turbulent boundary layers' greater resistance to APGs.

This low pressure rise through the front leg also provides an explanation as to why the separation of Fig. 8a is benign (without the extreme flow deviation and unsteadiness that was feared) and very shallow: a weak oblique separation shock corresponds to a small amount of flow turning, and so the bubble only grows gradually. With hindsight, this was also apparent in the experiments of Ackeret et al., but its significance remained unnoticed. As such, the separation can be many boundary layer thicknesses long, but the LDV results (Fig. 10) and schlieren image suggest the bubble height is still less than δ_1 by the rear leg location (as the boundary layer edge has only reached twice the original thickness).

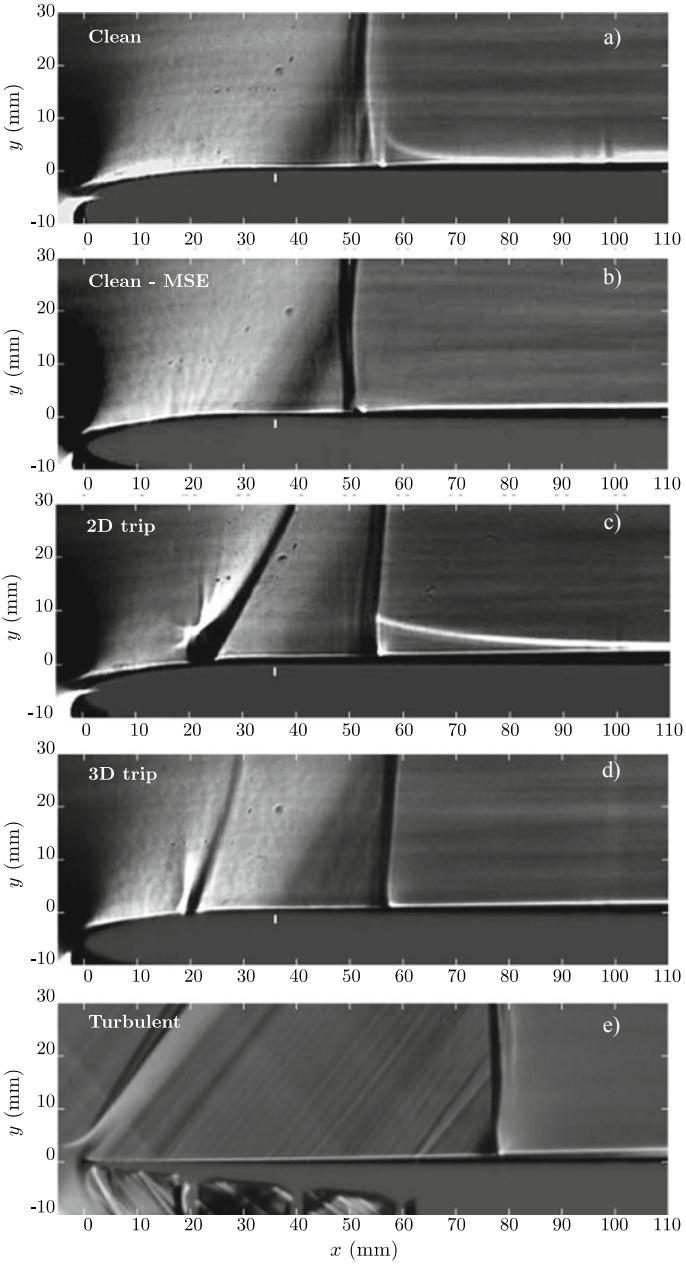

Fig. 8 Schlieren images of interactions on: **a** the clean ellipse plate; **b** the clean MSE plate; **c** the standard ellipse with paint strip at x = 20 mm; **d** the standard ellipse with trip dots at x = 20 mm, z = …, −10, 0, 10,… mm; **e** the supersonic plate of Fig. 5. (The start of the flat surface on the transonic plates, at x = 36 mm, is marked with a white line in (**a**−**d**))

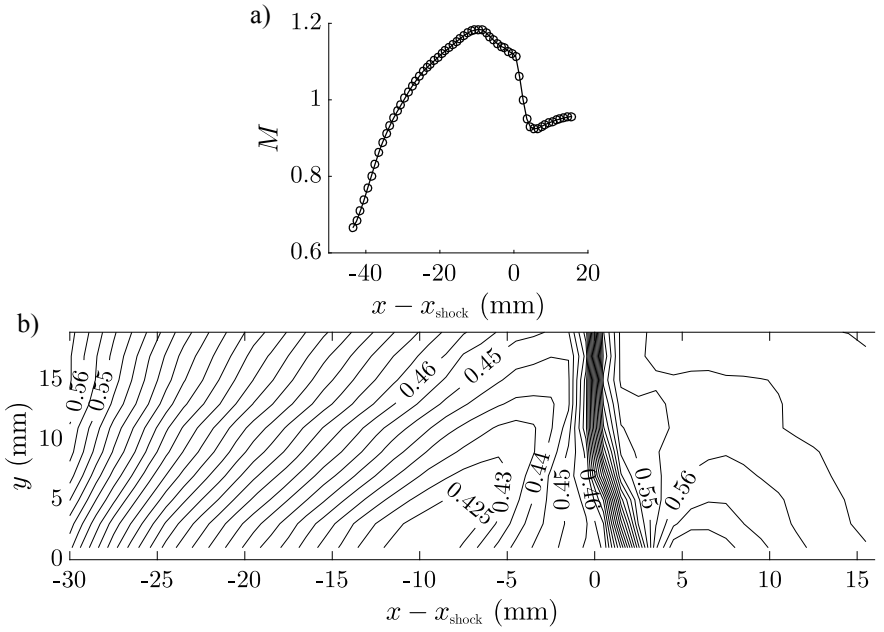

Fig. 9 LDV traverses through the clean interaction of Fig. 8a: **a** at y = 1 mm; **b** calculated isobars of p/p_0 (0.005 between contours)

It is difficult to determine where transition occurs in the flow, as upstream of and through the interaction the LDV system is only trusted to give an indication of the boundary layer height, due to the seeding problems associated with laminar flow and separation bubbles and compounded by the small size of the flow features. However, the presence of a lambda shock structure many times larger than δ, at a low Mach number, with little pressure rise through the front leg, effectively implies that the boundary layer is not turbulent ahead of the shock. By contrast, LDV shows a nominal 23% rise in p/p_0 through the rear leg, with no dramatic increase in thickness or separation size in the schlieren image, which suggests that transition has occurred by this location: if the boundary layer were not turbulent, a much greater impact would be expected at the pressure jump. It is suspected that transition is promoted by the front shock and the shear layer at the edge of the separation bubble, allowing the boundary layer to uneventfully navigate the rear shock.

Figure 8b shows a schlieren image of the flow with the MSE profile for comparison with the standard ellipse, with little variation seen between the two interactions. The expansion fan seems to end before the start of the flat surface of the plate, but this is because, as seen in Fig. 6b, the curvature significantly drops off towards the end of the profile.

Figure 8c shows the resulting flow when a stripe of paint is added at x = 20 mm to cause transition. Although the trip is only 10 μm high, a dramatic wave is seen in the schlieren, possibly indicating a small local separation, along with an increase

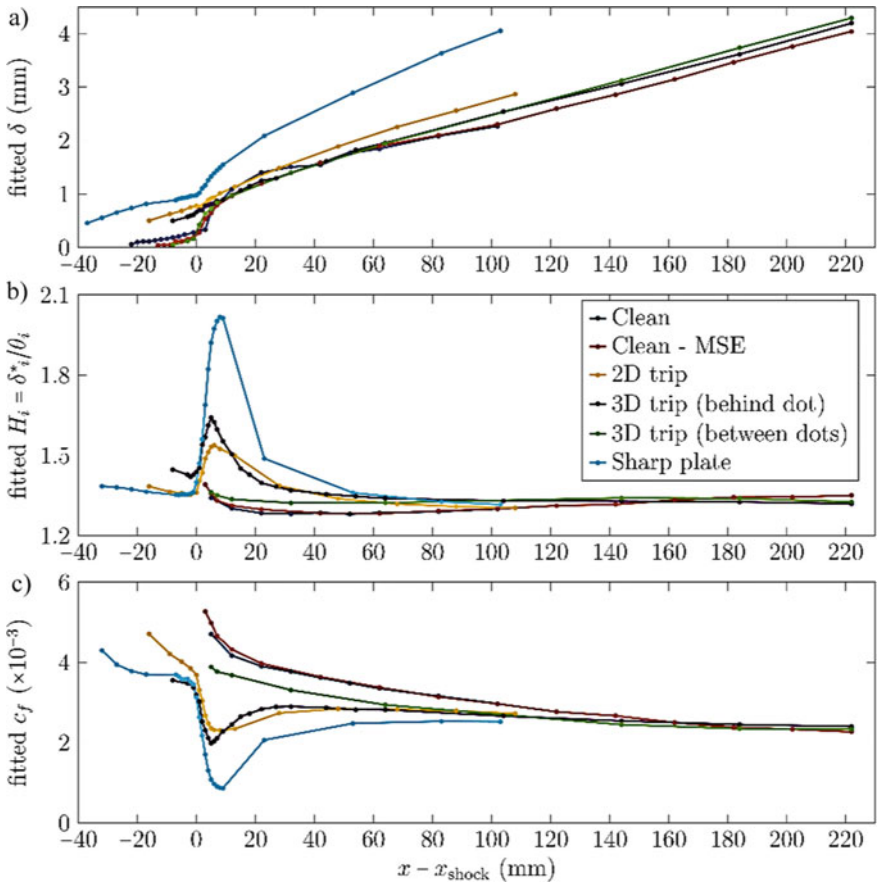

Fig. 10 Boundary layer properties for the flat plate interactions: **a** δ; **b** Hi; **c** c_f. (Other parameters shown only where δ < 0.5 mm.)

in boundary layer thickness (whilst not a direct measurement, the boundary layer increases from 6 to 9 pixels across the trip in the schlieren image). The interaction between the normal shock and the boundary layer is then much smaller than in the clean cases, with only a small amount of smearing visible at the shock foot. A very similar interaction is seen in both Fig. 8d, e on the standard ellipse plate with trip dots (Fig. 2) and the supersonic configuration of Fig. 5 (where the boundary layer is turbulent soon after the leading edge [1] respectively.

The LDV system has been used to investigate the boundary layer development for each flow case. Figure 10 shows the measured boundary layer thicknesses and calculated incompressible shape factors. In many of the traverse locations, δ is under 1 mm (compared to a measurement volume height of 0.09 mm) and so these data points have a high degree of uncertainty, particularly for integral properties, and are marked with dotted lines in the figure. This fact notwithstanding, in both the

naturally turbulent and the tripped cases, the boundary layer becomes less full through the interaction and then fills out again in a long post-shock rehabilitation process, only reaching an equilibrium turbulence state a long way downstream. Conversely (although the measurements are less trustworthy due to the smaller δ) the boundary layer downstream of the clean interactions are most full just after the shock, and then relaxes back to a higher Hi profile. This is corroborated in Figs. 11 and 12, which show normalised profiles and fluctuation intensities at two locations downstream of the shock. Every boundary layer is turbulent downstream of the interactions, with transition in the clean cases presumed to occur as the flow is lofted over the separation bubble.

Crucially though, at the far downstream locations the boundary layer state is the same for the clean and the tripped interactions, as evidenced by the shape factors. This suggests that the presence of separation in the clean cases has had no long-term effect on the flow. This is attributed to the small size of the separation, which is due to the low pressure rise required for a laminar/transitional boundary layer to separate, whereas it was anticipated that the ease of separation would cause a large bubble,

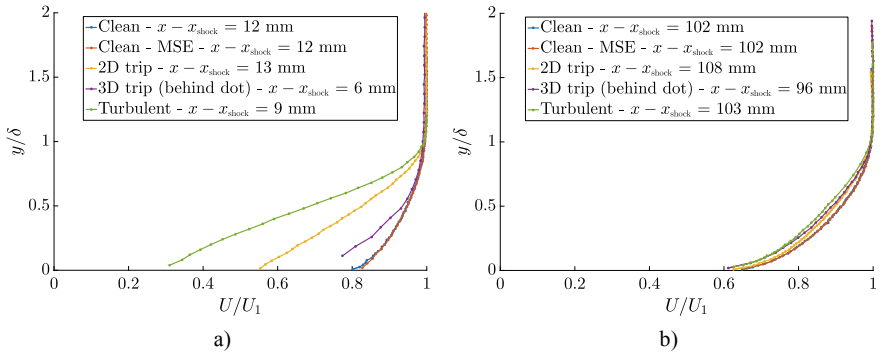

Fig. 11 Flat plate boundary layer profiles: **a** x − x_{shock} ∼ 10 mm; **b** x − x_{shock} ∼ 100 mm

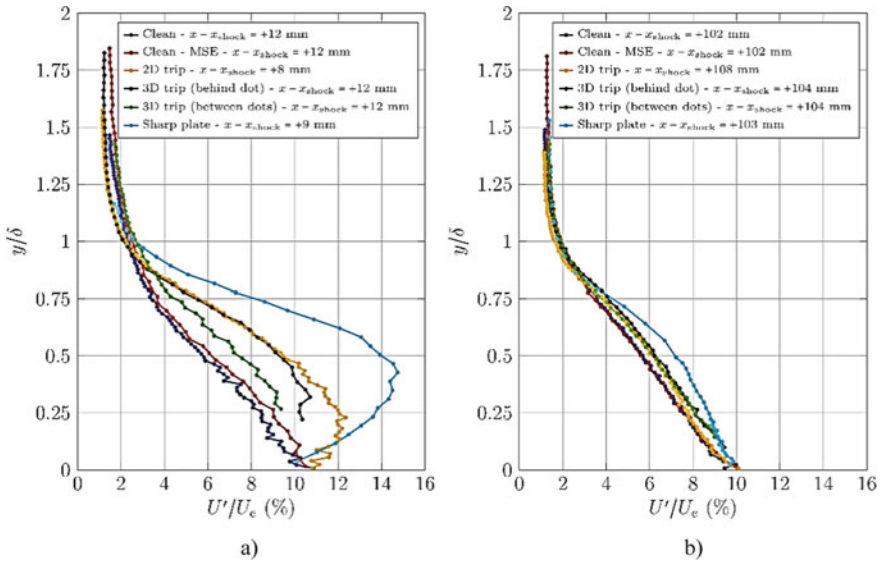

Fig. 12 Boundary layer fluctuation profiles:) x − x_{shock} ∼ 10 mm; **b** x − x_{shock} ∼ 100 mm

with associated losses and unsteadiness. In fact, due to the increase in δ across the paint strip, the 2D tripped case is actually less desirable than the clean cases, contrary to expectations (Table 1).

Table 1 Flat plate interaction details calculated from LDV & pressure data (δ_1 is the boundary layer thickness measured just upstream of the interaction), and so its value has a high degree of uncertainty in the 'Clean' and 'MSE' cases)

Interaction	M_∞	M_{shock}	P_0 (bar)	Unit Re (/m)	Re_{xshock}	$Re_{\delta 1}$	δ_1(mm)
Clean	0.85	1.18	2.05	28.9×10^6	1.59×10^6	2,800	0.1
MSE	0.81	1.22	2.05	28.1×10^6	1.35×10^6	<2,800	<0.1
2D trip	0.85	1.19	2.05	28.9×10^6	1.50×10^6	20,200	0.7
3D trip	0.82	1.21	2.05	28.3×10^6	1.53×10^6	8,500	0.3
Turbulent	1.3	1.27	1.7	26×10^6	2.00×10^6	23,400	0.9

1.3 CFD of the Laminar and Turbulent Interaction

1.3.1 URLMS

Physical model and numerical method

The numerical code of URMLS solves for the full three-dimensional Navier-Stokes equations for a compressible, viscous, heat-conducting gas

$$\frac{\partial \rho}{\partial t} + \frac{\partial \left(\rho u_j\right)}{\partial x_j} = 0 \tag{2}$$

$$\frac{\partial (\rho u_i)}{\partial t} + \frac{\partial \left(\rho u_i u_j\right)}{\partial x_j} + \frac{\partial p}{\partial x_i} - \frac{\partial \sigma_{ij}}{\partial x_j} = 0 \tag{3}$$

$$\frac{\partial (\rho E)}{\partial t} + \frac{\partial \left(\rho E u_j + p u_j\right)}{\partial x_j} - \frac{\partial \left(\sigma_{ij} u_i - q_i\right)}{\partial x_j} = 0 \tag{4}$$

where ρ is the density, u_i is the velocity component in the i-th coordinate direction, E is the total energy per unit mass, p is the thermodynamic pressure, and

$$q_j = -\lambda \frac{\partial T}{\partial x_j} \tag{5}$$

$$\sigma_{ij} = 2\mu S_{ij} - \frac{2}{3}\mu S_{kk}\delta_{ij} \tag{6}$$

are the heat flux vector and the viscous stress tensor respectively, and S_{ij} is the strain-rate tensor. The molecular viscosity is a function of the temperature T through the Sutherland's law, and the thermal conductivity λ is related to μ through the relation $\lambda = \frac{c_p \mu}{P_r}$ (the molecular Prandtl number P_r is assumed to be 0.72).

The Navier-Stokes equations are discretized on a Cartesian mesh and solved by means of a conservative finite-difference approach. The current version of the flow solver, extensively used in the past for the analysis of wall-bounded flows [11] and shock wave/boundary layer interactions [12] relies on sixth-order central discretization of the convective terms of the Navier-Stokes equations cast in split form [13], and it allows shock capturing through localized application of fifth-order WENO reconstructions controlled by the Ducros shock sensor. The diffusive terms are expanded to Laplacian form for improved stability, and also approximated with sixth-order central-difference formulas. The resulting semi-discrete ODE system is advanced in time through an explicit low-storage third-order Runge-Kutta algorithm [14]. We point out that the numerical methods particularly suitable for the simulation of transitional flows (which are expected in WP-2), because it is based on the concept of preservation of the total kinetic energy at the discrete level (in the limit of inviscid, incompressible flow and vanishing integration time step), thus yielding stable numerical solutions without needing extra numerical dissipation. In our opinion this

is a mandatory pre-requisite for numerical simulations of transitional flows to be reliable, since spurious numerical dissipation can artificially impact the evolution of disturbances, thus preventing or delaying the (possible) breakdown to turbulence. As explained in the next Section, boundary layer transition is promoted in the computations through vortex generators. In our numerical approach the presence of such devices is handled through the immersed-boundary (IB) method, which allows to deal with embedded geometries with arbitrary shape on a Cartesian mesh. The IB method is here implemented according to the approach proposed by [15] and adapted to steady compressible flows by [16]. Specifically, at each Runge-Kutta sub-step the velocity at grid points lying inside the body is modified to make it consistent with the local body velocity, which is zero in the case of a stationary body. Furthermore, the velocity at the fluid points nearest to the body surface is extrapolated in such a way that the no-slip condition is satisfied at the boundary points, thus providing second-order accuracy in the boundary treatment.

Computational arrangement and simulation parameters
The numerical simulations foreseen in WP-1 and WP-2 include the presence of a normal shock wave that interacts with a boundary layer which can be fully laminar, fully turbulent or transitional.

Results for laminar interaction
A sequence of flow snapshots for the $M = 1.2$ interaction are shown in Fig. 13, where we show contours of the density fields. In the same figure results are also shown from a purely two-dimensional simulation, to more clearly highlight the effects of three-dimensionality within the interaction zone. Starting from the same (unbalanced) initial conditions, the two simulations exhibit in the first stages ($t = 113$) the formation of a lambda-shock structure, and a precursor shock traveling to the right.

No difference is observed between 2D and 3D at this stage. Further on ($t = 284$), the lambda shock is seen to be expanded significantly. Clear Tollmien-Schliching waves are observed at this time in the 2D simulation, with matching pattern of eddy radiating waves, whereas the 3D simulation already shows signs of break-up to a three-dimensional state, and TS waves are much fuzzier in this case.

At $t = 454$ a distinct turbulent pattern is observed past the shock foot, whose effects translate into reduced spreading of the lambda pattern. At later times the reduced size of the interaction zone in the 3D case is more evident. Further, it is interesting to note the apparent alternation between periods characterized by the formation of large rollers (as at $t = 625$), which periodically break up into developed turbulence (as at $t = 795$). From a qualitative standpoint it appears that the most important effect of flow three-dimensionality is a reduction of the region of flow reversal in the 3D case, which implies that the shock foot remains much flatter than in the strictly 2D case, and it reached very close to the wall. A closer view of the interaction zone is shown in Fig. 14, which more clearly highlights the transition of the boundary layer to a turbulent state taking place shortly upstream of the impinging shock foot, which, at this specific instant, is seen to be bent somewhat downstream. It is interesting to observe that transition occurs well within the region of flow reversal, and reattachment follows quite rapidly, followed by an extended recovery region in

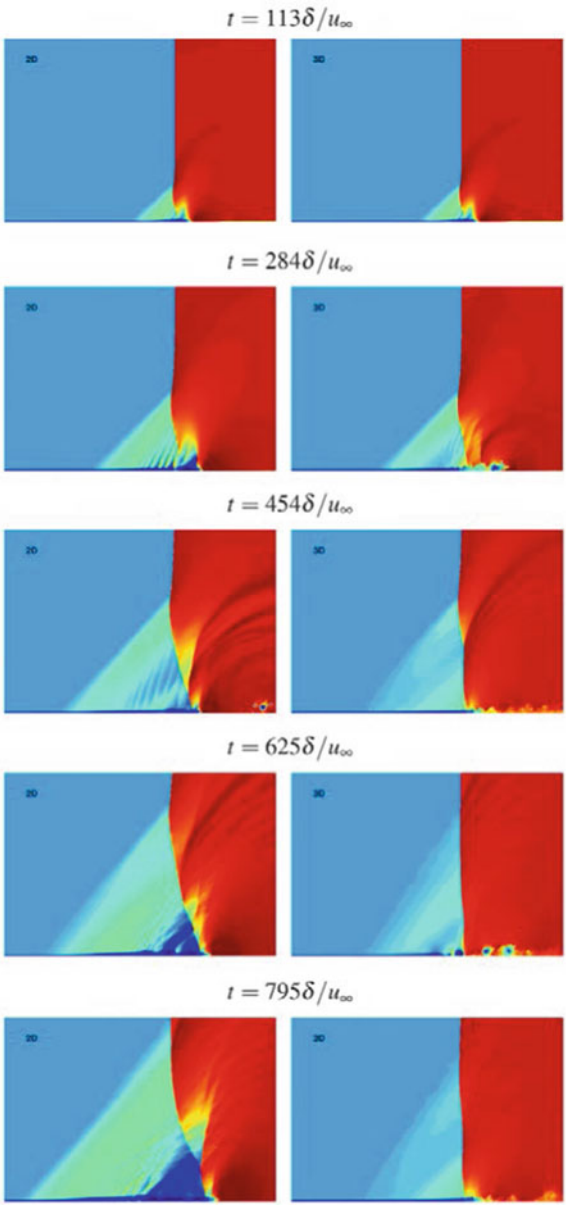

Fig. 13 Sequence of flow snapshots for numerical simulations of fully laminar interaction at $M_s = 1.2$. Two dimensional simulation result are shown in the left column, and three-dimensional results are shown in the right column. Density contours are shown in colour scale from blue (low density) to red (high density)

which large structures (see the organization of the pressure field) develop. The time-average skin friction and pressure coefficients, shown in Fig. 15, further highlight the complex, transitional nature of the interaction. Specifically, the pressure rise starts at about 150 δ upstream of the nominal impingement point, and flow separation occurs at x = 200 δ well in the laminar regime. A long shallow laminar separation

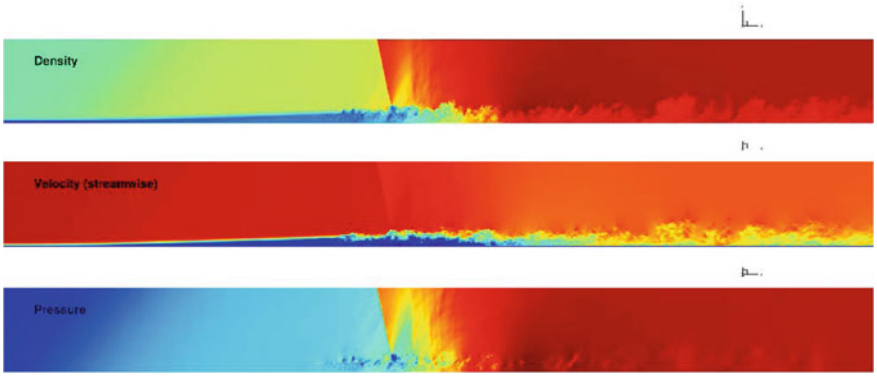

Fig. 14 Instantaneous x-y slices of density, streamwise velocity, and pressure in the vicinity of the shock foot, for fully laminar interaction at $M_s = 1.2$

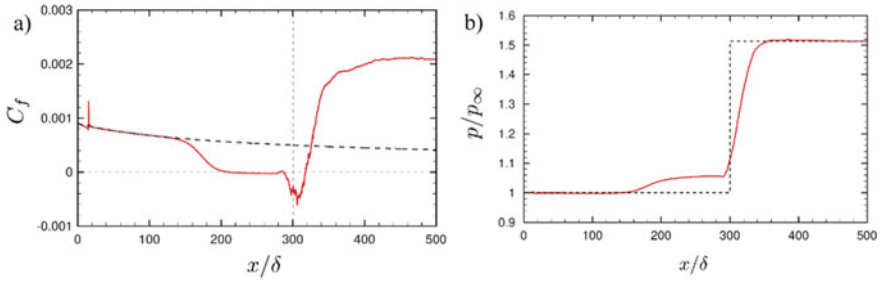

Fig. 15 Distribution of average skin friction (**a**) and pressure (**b**) in fully laminar interaction at $M_s = 1.2$

bubble is observed, in which pressure attains a plateau, and the friction coefficient has small negative values. Transition to turbulence takes place at $x - x_s = 12\delta$, where the friction coefficient is nearly zero, and then undergoes an abrupt increase in absolute value. Turbulent reattachment takes place at $x - x_s = 17\delta$, followed by a recovery region where the skin friction significantly overshoots its laminar value, indicating that the state of the downstream boundary layer is turbulent. A slight overshoot of pressure in the recovery region is also interesting, which is typical of shock/turbulence interactions. Overall, the observed pattern closely corresponds to the one observed in transitional separation bubbles in the incompressible regime [17, 18].

Turbulence statistics in the interaction zone are shown in Fig. 16. Notably, inception of transition to turbulence is associated with a distinct increase of the streamwise velocity fluctuations just above the separated shear layer. On the other hand, all other Reynolds stress components are only excited after the transition process is completed, and their amplification is clearly connected with the sudden reattachment of the boundary layer past the shock foot. An instantaneous three-dimensional view of

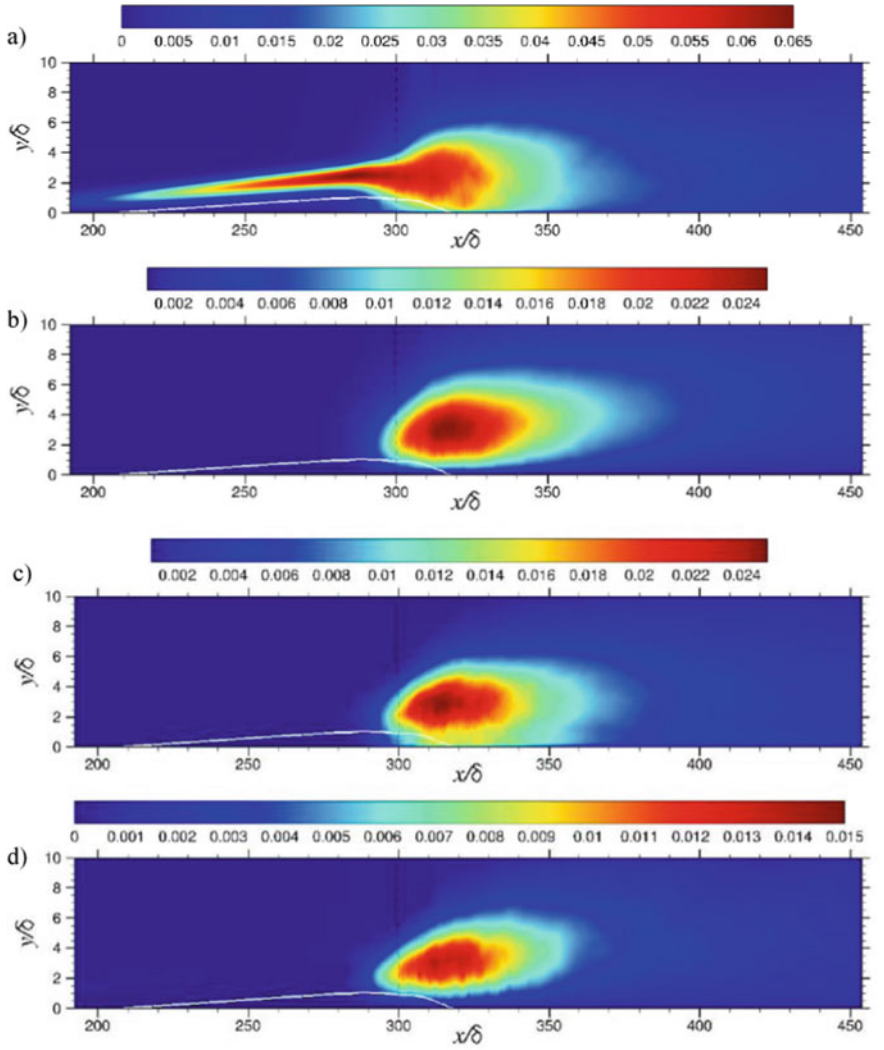

Fig. 16 Distribution of Reynolds stresses for laminar interaction at $M_s = 1.2$. **a** $\overline{u'^2}$; **b** $\overline{v'^2}$; **c** $\overline{w'^2}$; **d** $-\overline{u'v'}$. All stresses are scaled with respect to u_∞^2. The white line mars the boundary of the region of flow reversal ($\overline{u} = 0$). The vertical line denotes the nominal location of the interacting shock

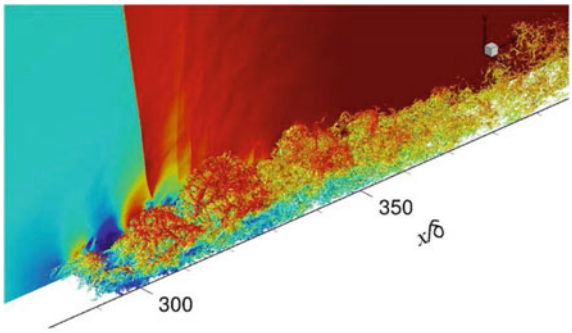

Fig. 17 Flow visualization for laminar interaction at $M_s = 1.2$. Vertical structures are educed through iso-surfaces of the swirling strength. The pressure field in also shown in a $x - y$ plane slice

the interaction zone at M = 1.2 is shown in Fig. 17, where we show iso-surfaces of the imaginary part of the complex conjugate eigenvalue pair of the velocity gradient tensor, or swirling strength [19]. Hairpin-shaped vortex tubes are observed to be generated near the transition point, at some distance from the wall, as in the typical by-pass scenario of all shear flows. The hairpin vortices are observed to form clusters downstream, which correspond to the rollers previously noticed in the instantaneous side views of the interaction. This 2D-like organization is lost further downstream, where no large-scale structures are observed, corresponding to the typical pattern observed in wall turbulence.

Results for turbulent interaction

Numerical parameters

The computation of the fully turbulent interaction has been carried out for a value of the normal shock strength equal to M = 1.3.

The computational domain employed for the simulation has a size 150 × 200 × 11 δ and it has been discretized with a grid consisting of 10240 × 640 × 1024 points. The mesh points are non-uniformly spaced in the streamwise direction to allow better resolution in the region occupied by the VGs. Points are also clustered in the wall-normal direction to resolve the boundary layer, and the compression fan of the shock wave up to y = 5 δ. Finally, the grid points are equally spaced in the spanwise direction. The size of the computational domain has been selected through a series of preliminary calculations. In particular, the length of the computational domain is dictated by the necessity to accommodate the entire interaction zone, including the upstream influence region and a large part of the recovery zone past the impinging shock. With regard to the extent of the domain in the wall-normal direction, we have found that it is critical to have it as large as possible to prevent choking of the computational duct, thus avoiding bulk motion of the impinging shock. Placing the upper boundary of the domain at y = 200 δ prevents the occurrence of computational

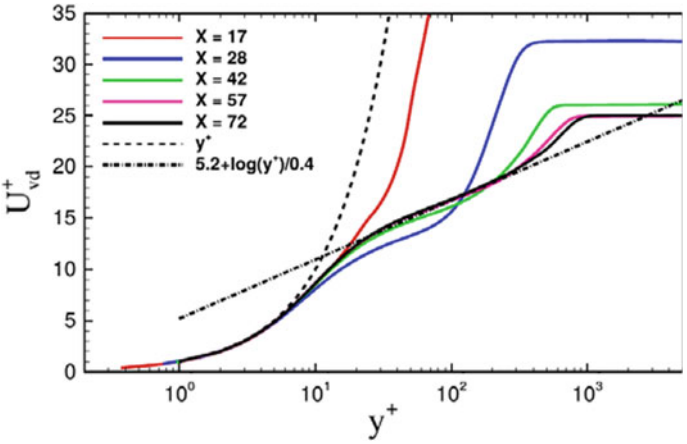

Fig. 18 Distribution of Van Driest transformed mean streamwise velocity in inner scaling at reference stations

Table 2 Properties of incoming boundary layer at the reference station $x_{ref} = 17.3\ \delta_{in}$. $Re_\theta = \rho_e u_e \theta/\mu_e$; $Re_{\delta 2} = \rho_e u_e \theta/\mu_w$; $Re_\tau = \rho_e u_\tau \theta/\mu_w$; $H = \delta^*/\theta$; $H_i = \delta_i^*/_i\theta$

M_e	Re_θ	$Re_{\delta 2}$	Re_τ	Cf	δ^*/δ	θ/δ	H	H_i
1.2	3770	3020	1003	2.73×10^{-3}	0.381	0.188	2.03	1.36

choking over much longer times than those necessary to achieve stationarity of the flow and statistical convergence.

Characterization of the incoming boundary layer

The statistics of the incoming flow are first analyzed to check that the structure of the boundary layer immediately upstream of the interaction is that of a canonical zero-pressure-gradient (ZPG) boundary layer. To that purpose, the distribution of the Van Driest-transformed mean streamwise velocity

$$U_{vd} = \int_0^u \sqrt{\rho/\rho_w}\, du \tag{7}$$

is reported in Fig. 18 in inner scaling at some streamwise stations taken past the vortex generators. The figure well describes the evolution of the (initially laminar) boundary layer in the streamiwse direction, which, owing to the presence of disturbances generated by the VGs, experience transition to a fully turbulent state, which is achieved approximately at x = 57 δ, where the shape of the velocity profile well conforms to that of a canonical TBL, with a nearly logarithmic region between $y^+ = 30$ and $y^+ = 200$, characterized by a von Karman constant k = 0.41 and additive constant C = 5.2. The global boundary layer properties at a location immediately upstream of the interaction (x = 80 δ), are listed in Table 2. The thickness of the boundary layer is determined as the point where u = 99% u_e, and the displacement

(δ^*) and momentum (θ) thicknesses are defined as

$$\delta^* = \int_0^{\delta_e} \left(1 - \frac{\overline{\rho}}{\rho_e}\frac{\overline{u}}{u_e}\right) dy \tag{8}$$

$$\theta = \int_0^{\delta_e} \frac{\overline{\rho}}{\rho_e}\frac{\overline{u}}{u_e}\left(1 - \frac{\overline{u}}{u_e}\right) dy \tag{9}$$

where δ_e is the edge of the rotational part of the flow field, and u_e and ρ_e are the corresponding external mean velocity and density. The 'incompressible' boundary layer thicknesses (pedex i) and the associated shape factor (H_i) are also determined from the above equations by setting the density ratio to unity.

Mean wall properties

The mean wall pressure across the interaction zone is here compared with the experimental data of Delery & Marvin. Note that the former were obtained in a transonic channel with a wall-mounted bump to accelerate the flow and form a supersonic region terminated by a quasi-normal shock wave. Hence, owing to the presence of the bump, the boundary layer upstream of the shock wave develops under favourable pressure gradient, and it exhibits a fuller profile than in a ZPG boundary layer at the same Reynolds number. As a consequence, the wall pressure distribution is not constant upstream of the interaction, and the incompressible shape factor has a relatively small value (see Table 2). Because of the differences in the Reynolds numbers, and the sensitivity of the flow details on the downstream conditions, comparison with experiments should only be interpreted in qualitative sense.

Let the interaction length-scale L be defined as the distance between the sonic point location x_1 (i.e. the streamwise station where the mean wall pressure equals the critical pressure $p^* = 1.46 p_e$ at M = 1.3), and the origin of the interaction x_0 (i.e. the point where the wall pressure starts to rise) For weak-to-moderate interactions, Delery & Marvin showed that scales with the upstream boundary layer properties according to

$$L \approx 70\delta_0^*(H_{i0} - 1) \tag{10}$$

As observed in Table 3, the computed interaction length-scale agrees fairly well with the equation above; Delery & Marvin also showed collapse of the wall properties

Table 3 Interaction parameters for DNS and experiments (the subscript refers to the orgin of the interaction)

	M_0	$Re_{\theta 0}$	H_{i0}	L/δ_0^*	$L/\delta_0^*/(H_{i0}-1)$
DNS	1,3	3770	1,36	25,5	70
Delery and Marvin [1986]	1,3	7526	1,3	21	70

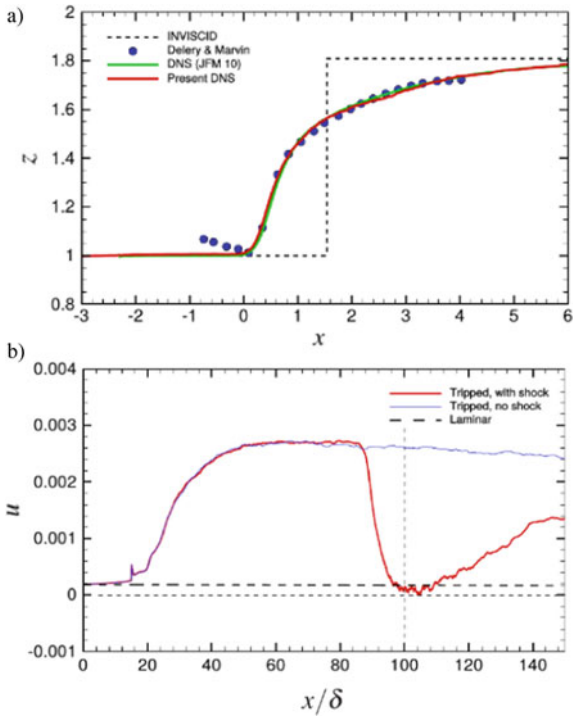

Fig. 19 Distribution of mean wall pressure (**a**) and skin friction coefficient (**b**). *R—H* denotes the inviscid distribution resulting from the Rankine-Hugoniot jump conditions. Refer to Table 3 for nomenclature of symbols

(at various Re and M) when reported in the scaled interaction coordinates $x^* = \frac{x-x_0}{L}$, $y^* = y/L$. In the following, for comparison purposes, the results are then reported in terms of x^* *and* y^* and we refer to three distinct zones: the upstream ZPG region ($x^* < 0$); the supersonic adverse-pressure-gradient (APG) region ($0 < x^* < 1$); and the subsonic APG region ($x^* > 1$).

The scaled mean wall pressure is reported in Fig. 19a together with the inviscid pressure jump predicted by the Ranking-Hugoniot relations. It exhibits a sharp rise in the supersonic APG region, in excellent agreement with experiments, and a milder increase in the subsonic APG region. Note that, remarkably, the distribution obtained in the present DNS is nearly identical to that of a previous computation [12], performed with the recycling/rescaling method, without taking into account the full spatial evolution of the incoming boundary layer, from a laminar to a fully turbulent state. This agreement confirms the validity of the approach here followed, which has the advantage to be more general and to allow the opportunity of simulating transitional interactions.

The distribution of the mean skin friction coefficient is reported in Fig. 19b together with that obtained in the absence of the normal shock. These curves are nearly identical up to (), which marks the location of the shock upstream influence and are characterized by a rapid rise of the friction coefficient at x, corresponding to the flow breakdown and the transition to a turbulent state. While in the absence of

the normal shock the skin friction slightly decreases in the fully developed turbulent region, in the case of SBLI, starting from x = C_f exhibits a sudden drop, and attains a minim (close to zero), before showing a slow recovery past the interaction zone. According to Delery & Marvin the present case is to be classified as an incipient separation one.

Flow visualizations: instantaneous fields
The computed instantaneous density, streamwise velocity and pressure fields are reported in Fig. 14 in the streamwise, wall-normal plane at a given time frame.

As observed by [20] in the case of an impinging shock/boundary layer interaction at supersonic Mach number, and by [21] for a low-speed turbulent boundary layer under adverse pressure gradient, the instantaneous pressure field highlights the formation of pressure minima associated with the shedding of eddies that form in the proximity of the outermost inflection points of the mean velocity profiles. As better appreciated from inspection of the flow animations (available on the TFAST website), such vortices lift off from the wall approximately in the middle of the interaction zone, and propagate downstream giving rise to a turbulent mixing layer. Sharp density interfaces are also observed in the outermost part of the boundary layer, separating boundary layer turbulence from the outer, essentially inviscid flow, and that become more convoluted past the interaction zone.

2 Oblique Shock Wave Reflection

2.1 Test Section Design and Construction

2.1.1 IUSTI M = 1.6

Experiments are performed in the S7 test section of the IUSTI supersonic wind tunnel. It is a closed-loop continuous hypo-turbulent facility (intensity of the pressure fluctuations is 0.12% for a stagnation pressure of 0.4 *atm*); it can be operated continuously during several hours without pressure drift. The operating points correspond to stagnation pressures ranging from 0.15×10^5 to 0.9×10^5 *Pa*. The stagnation temperature depends on the ambient temperature, and it is maintained nearly constant by a cooling water system, with a typical drift less than 1 K/hour, The test section is 150 mm wide (spanwise) and 80 mm high and the nominal Mach number is 1.68.

The studies deal with a laminar boundary layer developed over a flat plate on which an oblique shock wave impinges. The model is composed of a flat plate of 175 mm long and 150 mm wide. Its leading edge is placed at 110 mm from the exit of the wind tunnel nozzle and it is placed at 20 mm above the wind tunnel bottom wall. A sharp-edged shock generator 30 mm long is installed at 72 mm downstream of the leading edge of the flat plate and at a distance of 30 mm above the flat plate. The shock generator and the flat plate span entirely the test section. For such Mach numbers, special attention must be paid to reduce the risks of blockage

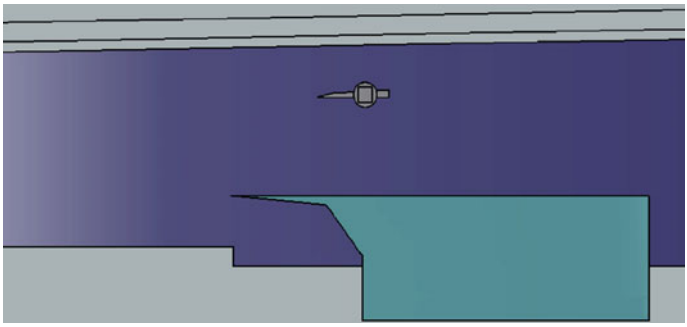

Fig. 20 Sketch of the test section with the model

effects. RANS simulations were used to obtain a design minimizing blockage effects. The final design is reported in Fig. 20. The leading edge of the flat plate makes an angle less than 5° and a cavity is placed underneath the flat plate to avoid chocking this secondary channel. A progressive recompression is generated downstream of the plate. The shock generator is directly housed in the Plexiglas windows: this suppresses the presence of masts to fix the generator and contributes to avoid blockage of the flow over the shock generator; of course, this design precludes to use Schlieren visualizations. The origin of the abscissa is taken at the leading edge of the flat plate.

Total pressure was measured with a flattened Pitot probe: the thickness of the probe is of 0.3 mm, and its opening is of 0.1 mm high. As the boundary layer thickness is very small (typically less than 0.7 mm) only external measurements, over the shear layer, have been performed. Hot wire measurements have been made at the same positions than the pressure measurements with a "StreamLine" Constant Temperature Anemometer (CTA) system from *Dantec Dynamics*. The wire length is 1 mm, its diameter is 5 μm. It is operated with an overheating ratio $a_w = 0.8$. These external measurements have been supplemented with in-flow Laser Doppler Anemometry measurements. One component system has been used in order to allow very near wall measurements. An Argon-ion laser from *Spectra-Physics (6 W, Stabilite 2017)* has been used. Only the most energetic wave length ($\lambda = 514.5\,nm$) is used, to measure the longitudinal component of the velocity. The emitted beam is of 2.25 mm in diameter and a FiberFlow system from *Dantec Dynamics* is used. A Bragg Cell imposes a shifting frequency of 40 MHz to one of the beam, allowing the system to resolve negative velocities. A beam-spacer is used to adjust the distance between the two beams to 19.2 mm. Two different emitting head have been used, with respectively one and two beam expanders with 1.98 ratio, both with a 50 *cm* converging lens, leading to a measurement volume of respectively 70 μm and 38 μm diameter. The fringe spacing is respectively 6.70 and 5.97 μm. The 70 μm was initially used for mean velocity measurements. Unsteady measurements (second to fourth order moments) have been obtained with the 38 μm system. The laminar state of the boundary layer has been validated from LDA measurements. The profiles obtained in various location and for stagnation pressures ranging from 0.4 to 0.8 atm are

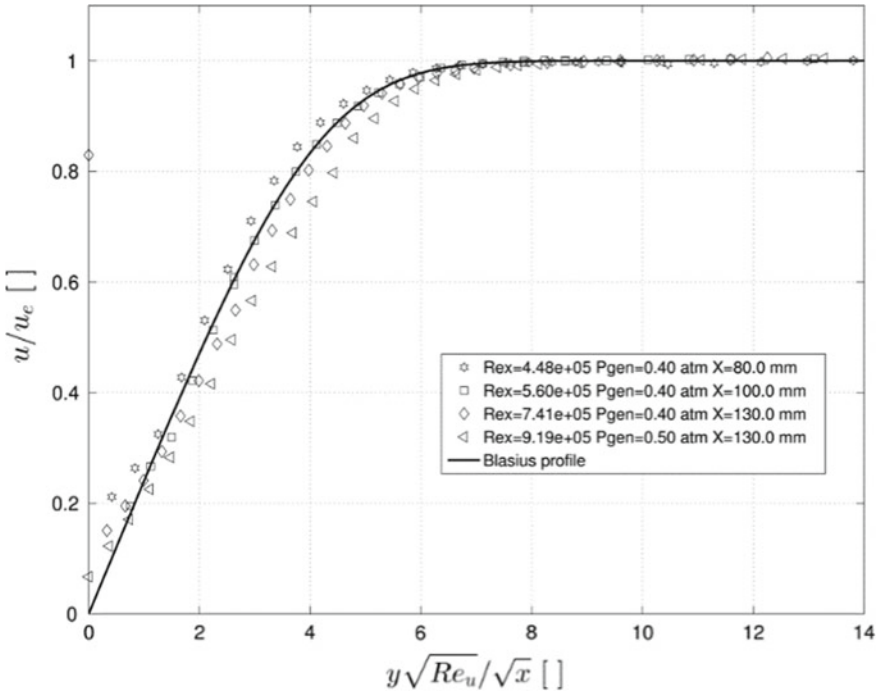

Fig. 21 Velocity profiles in normalized representation—LDA measurements

reported in Fig. 21 similarity variables. They compare very well with the theoretical Blasius profile. The dimensionless thickness of the boundary layer has been derived:

$$\widetilde{\delta} = \delta\sqrt{\frac{\mathrm{Re}_u}{x}} = 6.67 \tag{11}$$

The receptive head is positioned backward and off-axis. The off-axis angle is about, in order to receive the maximum light emanating from particles in the backward configuration and then to optimize the signal-to-noise ratio. We used particles of incense smoke whose average size is less than one micrometer to seed the flow. Particles are injected through a seeding cane placed at the end of the plenum chamber, on the wind tunnel axis. The seeding system is adjustable vertically in order to seed the interaction zone.

2.1.2 ONERA-DAFE M = 1.6

Introduction

Shock-wave/boundary layer interaction plays a major role in any circumstances where the flow becomes supersonic, either locally or in totality. This phenomenon

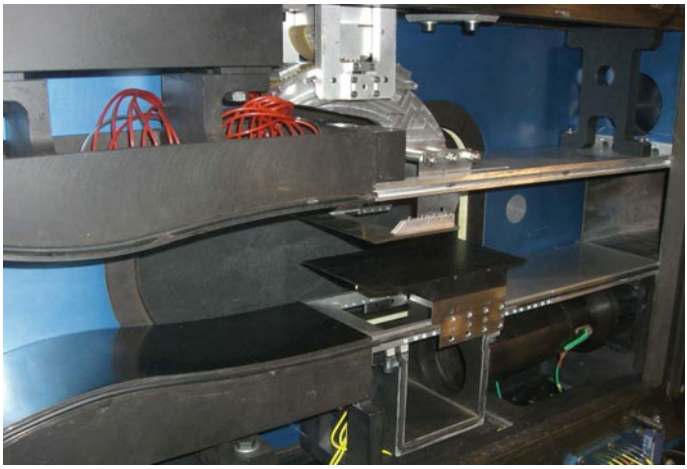

Fig. 22 Test set-up with the Mach 1.6 full nozzle in the S8Ch wind tunnel

is not clearly understood when the transitional regime (from laminar to turbulent) of the boundary layer appears during the interaction process, which is the case for compressor or turbine cascades configurations and for laminar transport/business aircraft wing. It is proposed to execute an experimental investigation of the shock-wave effect on the boundary layer transition occurring at a moderate supersonic Mach 1.6 number. Then, control devices—two types of 3-D turbulator—are tested to act on the boundary layer transition submitted to a shock-wave.

Firstly, the test set-up arrangement in the wind tunnel with means of investigation and flow parameters are presented. The boundary layer transition is detected by using several techniques: Schlieren visualizations, IR (Infra-red) thermography and TSP (Temperature Sensitive Paint) measurements. Results on the natural boundary layer transition are discussed. Then, the transitional interaction is described with respect to variation of flow parameters and to influence of control devices.

Test set-up arrangement and means of investigation

Wind tunnel and test set-up arrangement

The experimental investigation is executed in the S8Ch wind tunnel of the ONERA Meudon Centre. This facility is a continuous wind tunnel supplied with desiccated atmospheric air. The stagnation conditions are near ambient pressure and temperature: $p_{st} = 0.96 \times 10^5 \pm 300$ Pa and $T_{st} = 300 \pm 10$ K. It is constituted by a rectilinear channel having a test section with a height of 120 mm and a span of 120 mm (in full nozzle configuration). The test section side walls and upper wall are equipped with high quality glass windows to allow using optical techniques, mainly to detect the location of the boundary layer transition.

Figure 22 shows the test set-up with the Mach 1.6 full nozzle configuration, the unit Reynolds number being around 14×10^6 m^{-1} for this Mach number. The shock generator wedge (with its displacement device) has been installed on the upper wall of the test section. It is supported by lateral masts and has reduced dimensions to alleviate the aerodynamic loads when the angle of attack is increasing during the run. The flat plate under study is mounted above the lower wall and the re-generated boundary layer will interact with the shock-wave. The location of the flat plate has to be movable in both the longitudinal and vertical directions to allow the study of the boundary layer behaviour with respect to the shock impingement. The leading edge shape of the flat plate is designed to take into account of the bluntness effect on the boundary layer transition and to allow the shock to stay attached: the flat plate thickness is equal to 3 mm; its leading edge radius is around 20 μm and the bevel angle is equal to 6°. The flat plate length, equal to 200 mm, is dimensioned by both the location of the natural transition and the side wall boundary layers contamination, and its span is equal to the test section width (120 mm). In order to perform IR (Infra-red) thermography measurements, the material of the flat plate is chosen as Ino × 304L. The surface finish is achieved by hand work using emery cloth and the averaged rugosity (Ra) is estimated at 0.8 μm. Moreover, the expansion fan emanating from the shock generator trailing edge influences the flow on the study plate far downstream of the region of interest. Lastly, the test set-up is located in such a way that the leading edges of the two plates remain in the Mach number rhombus, in order to avoid any perturbation of the flow.

Suction through the upper and lower walls of the test section is necessary to remove the incoming wind tunnel floor boundary layer and to avoid blockage effect of the flow due to the presence of the flat plate and the shock generator wedge. Auxiliary pumps and high pressure air supply are available to perform this fluidic control of the flow (see the open areas, the cavity and the duct on Fig. 22). Despite the beneficial effect of suction, several modifications of the test set-up are carried out to postpone blockage effect of the secondary flow under the flat plate; i.e., a reduction of the lateral masts section supporting the flat plate and a 12°-inclination of the lower wall upstream of the cavity to accelerate the secondary flow. Finally, the suction mass flow rate necessary to maintain the secondary flow supersonic is equal to 120×10^{-3} kg/s under the flat plate and 50×10^{-3} kg/s above the shock generator wedge.

Means of investigation

The detection of the boundary layer transition region is performed by using several techniques whose results will be compared and cross-checked to accurately determine the transition process on the flat plate. So, these techniques are:

- Schlieren visualizations (continuous and spark) obtained by using an high-speed Phantom V710 camera located on the side of the wind tunnel.
- IR (Infra-red) thermography measurements. Figure 23 shows the IR thermography arrangement used. It is constituted of a camera FLIR SC7000 (size image: 640 × 512 pixels with 1 pixel equal to 14 μm; lens of 50 mm; integration time: 2 ms and frame rate: 100 Hz) and of a IR window mounted on a sidewall of the test set-up.

- TSP (Temperature Sensitive Paint) measurements. Figure 24 shows the TSP arrangement used. It is constituted of a UV-lights source located in one side of the test set-up (right picture) and of a camera placed in the other side (left picture). The flat plate is entirely painted excepted near the leading edge in order to not modify its shape, because the bluntness effect is sensitive on the transition location.

2.1.3 TUD M = 1.7

The experiments were performed in the blow-down transonic-supersonic wind tunnel (TST-27) of Delft University of Technology. The facility is able to generate flows in the Mach number range 0.5 to 4.2 in the test section. The Mach number is set by means of a continuous variation of the throat section in combination with flexible nozzle

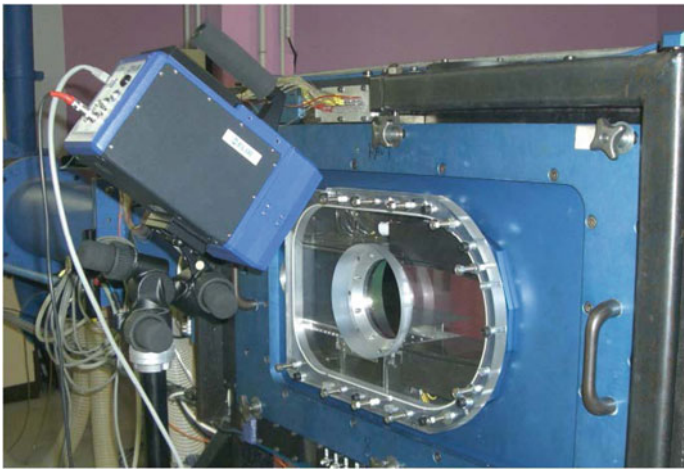

Fig. 23 Infra-red thermography arrangement near the test set-up of the S8Ch wind tunnel

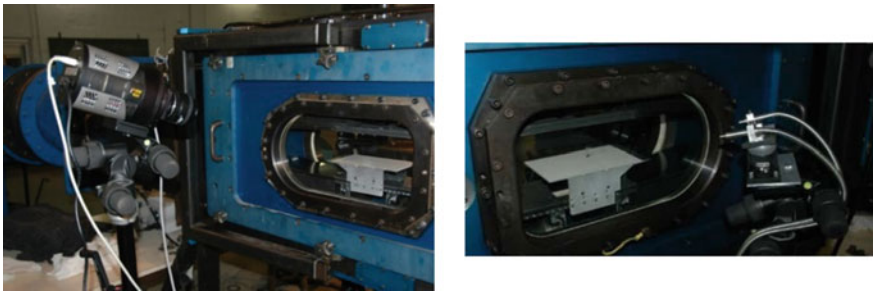

Fig. 24 Temperature Sensitive Paint arrangement near the test set-up of the S8Ch wind tunnel

walls. Air is supplied from a storage vessel of 300 m^3 charged to 42 bar and stored at ambient temperature (280–290 K typical), which allows a blow-down operating use of the tunnel of approximately 300 s maximum (depending on operating conditions), before recharging is required. In the present experiments, the tunnel is operated in the low-supersonic regime at a Mach number of 1.7. In order to reliably operate the wind tunnel at this Mach number a (minimum) stagnation pressure of 230 kPa is required which yields a unit Reynolds number in the test section of approximately 34×10^6 m^{-1}.

The settling chamber of the wind tunnel has a square cross section of 800 × 800 mm. In the first section of the converging nozzle the flow channel contracts in lateral direction only, to the final (constant) channel width of 280 mm. Subsequently, the nozzle upper and lower walls provide the (continuously adjustable) contoured converging-diverging shape, symmetrical with respect to the tunnel centre line, to produce the required Mach number in the test section. The distance from the throat to the centre of the test section measures approximately 2 meters. The major components and dimensions of the nozzle and test section are indicated in the technical drawing of Fig. 25.

The SWBLI geometry consists of a full-span flat plate with a sharp leading edge ($R \sim 150$ μm), which is used for generating a laminar boundary layer, and a symmetric partial-span shock generator (see Fig. 26). The relative longitudinal position of these elements can be adjusted to locate the incident shock wave in the laminar, transitional or turbulent region of the boundary layer. The angle of attack of the shock generator can be changed, allowing the investigation of shock strengths in the range of 1° – 6°. For the baseline TFAST experiments, the flow deflection angle is set to 3°, which corresponds to an inviscid pressure ratio of $p_3/p_\infty = 1.35$. After several iterations a flat plate—shock generator configuration was obtained which achieved a correct (non-chocked) operation of the wind tunnel, as can be verified from the Schlieren visualization in Fig. 27.

A combination of experimental techniques has been employed to characterize boundary layer transition and the shock wave-boundary layer interactions. Particle

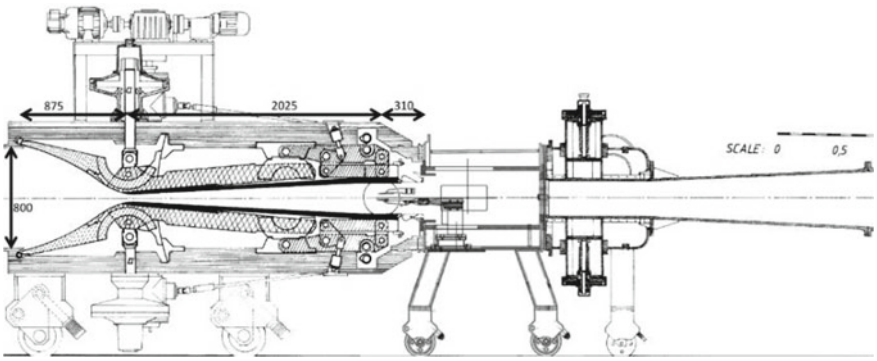

Fig. 25 Characterization of wind tunnel overall geometry

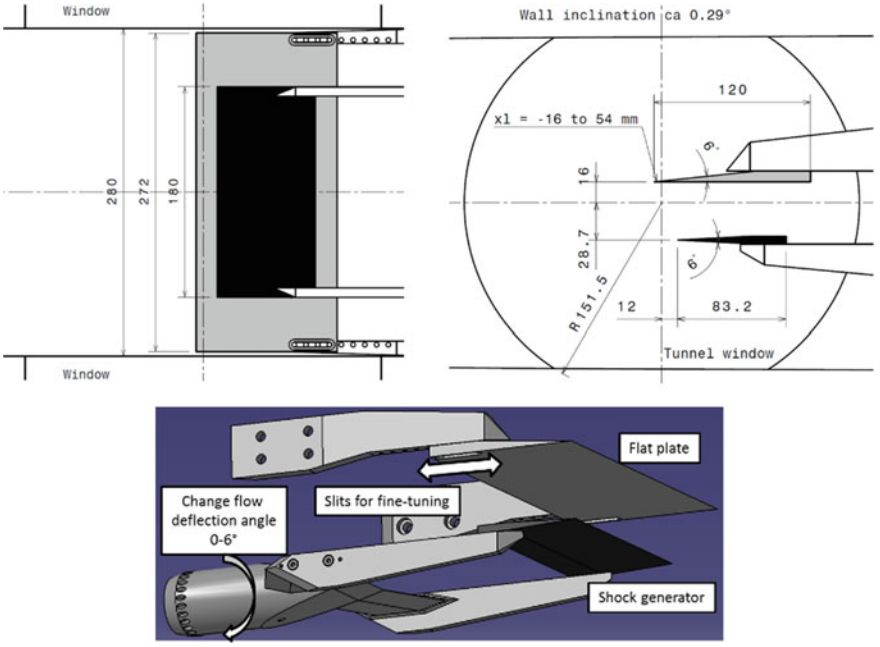

Fig. 26 Side view (top left) and bottom view (top right) of the wind tunnel configuration (in grey: flat plate model, in black: shock generator), all dimensions are in mm; the bottom picture shows an isometric view of the flat plate, shock generator and supports (Catia model)

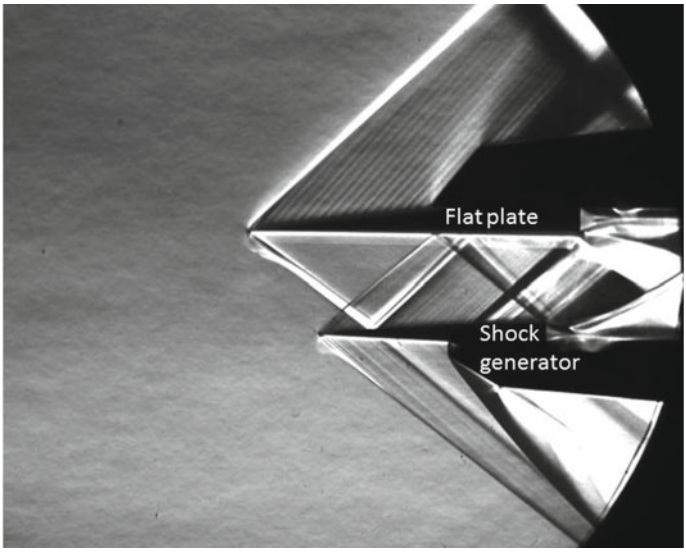

Fig. 27 Schlieren visualization of the full configuration

image velocimetry (PIV) was used as the main diagnostic tool. Additional use was made of hot wire anemometry to determine the freestream turbulence level. Spark-light Schlieren visualizations and infrared thermography measurements were used to determine the transition location. Oil-flow visualizations were performed to assess the two-dimensionality of the interaction and to reveal the wall flow-topology.

2.1.4 ITAM M = 1.5

The experiments were performed in wind tunnel T-325 of ITAM for Mach number $M_\infty = 1.47$, total temperature $T_0 = 291$ K and total pressure $P_0 = 0.55 \div 1.0 \times 10^5$ Pa. The test section of the wind tunnel had a rectangular cross section of 160 × 200 mm. The nozzle was specially designed and manufactured for TFAST experiments. It consists of symmetric upper and lower parts providing uniform flow with designed Mach number. The experimental setup is presented in Fig. 28. Experimental setup consisted of a plate with sharp leading edge occupying full span of the test section and a wedge generating a shock wave. The flat plate and the wedge were attached to the lower and upper boxes extending the nozzle halves and used for the flow bypass. There were two bypass channels providing start of supersonic flow in the test section: one beneath the model and another above the wedge. The flow bypass was designed so that does not influence the flow in the area of interest. The boundary layer formed on the lower wall of the nozzle went to the channel below the model and did not influence the flow in the interaction zone. The boundary layer developed on the upper nozzle wall went above the wedge. The channels were shaped to provide supersonic

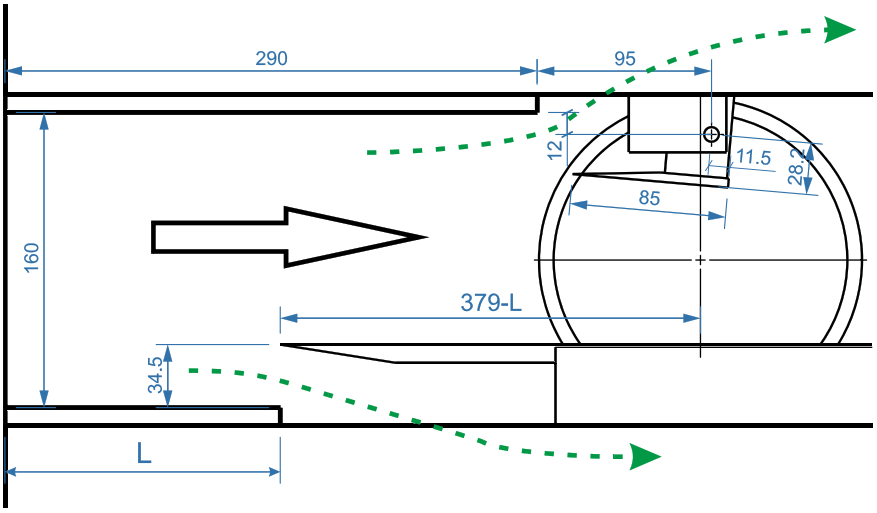

Fig. 28 Draft of the experimental setup

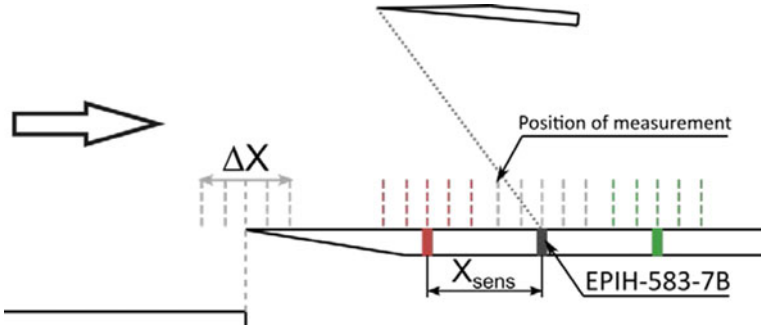

Fig. 29 Scheme of the experiment

flow at least in their intake regions so the shock at the wedge is attached to its leading edge. The flow near the model LE was supersonic too.

There were three flat plate models of the same shape prepared for the experimental campaign. The first model was made from steel and intended for PIV measurements, hot-wire and BL transition measurements. The second model (see Fig. 29) was equipped by pressure ports for static pressure measurements and EPIH sensors for unsteady surface pressure measurements. It had a line of pressure ports for static pressure measurements displaced from the centerline for 14 mm. The line of unsteady pressure sensors EPIH-583-7B was placed parallel to centerline at a distance 14 mm. The third model was made from plastic and was intended to install plasma control devices. The flat plate models were installed by means of two long pylons and could be fixed in any desired streamwise position.

The wedge assembly was installed in the upper box. To provide the space for the flow bypass in the box, the wedge was held by two pylons of streamlined cross-section. Position of the wedge rotation axis was chosen to provide minimum shift of the interaction point with variation of the wedge angle of incidence. The wedge frame was driven by pneumatic cylinder and could be fixed in two extreme positions defined by the stoppers. The range of wedge position was $-2 \div +5°$. The wedge was initially installed in the nose-down position providing start of the flow in the test section and then rotated to the test position (for example $+4°$) for the measurements.

The optical windows of diameter 220 mm were installed into the side walls. Position of the wedge was chosen to provide intersection of the shock wave with the flat plate model approximately in the center of the optical window. These windows were used for schlieren visualization and PIV measurements. The laser sheet for PIV entered through the window downstream and reflected by the prism attached to the traversing gear.

PIV was chosen as the main flow diagnostic technique. The flow seeding was performed in the wind tunnel settling chamber by DEHS particles of diameter 0.9 μm. PIV measurements were done in the region of the interaction at the centreline of the model. In the case of flow control experiments the PIV measurements were synchronized with plasma discharge.

2.2 *Experimental Investigation at Laminar and Turbulent Conditions*

2.2.1 IUSTI

The experiments performed at IUSTI are summarized Table 4. For each experiments, the flow deviation angle is fixed at an angle Θ_i by use of the shock generator. The real flow deviation has been defined Pitot measurements trough the incident shock wave, by analysis of the pressure jump, at each stagnation pressure. The real flow deviation angle is then reported for each experiment (see Table 4). A slight influence of the stagnation pressure on the effective flow deviation has been observed: about $\pm$ 0.5° from the intermediate pressure of 0.6 *atm*.

As previously mentioned, no Schlieren visualizations were available, therefore Pitot measurements have been used to derive the global organization of the interaction. The pressure measurements along the interaction, performed at 5 mm from the wall, are plotted on Fig. 30. In this figure, a first smooth pressure rise corresponding to reflected compression waves can be observed. This area is followed by a pressure plateau, characteristic of separated interactions (Délery and Marvin [22]), which is

Table 4 Matrix of experiments

Pgen Θ	Θ_1	Θ_2	Θ_3
0.4	3.67 ▼	4.40 ■	4.96 ●
0.6	4.30 ▼	4.92 ■	5.08 ●
0.8	4.62 ▼	5.28 ■	5.88 ●

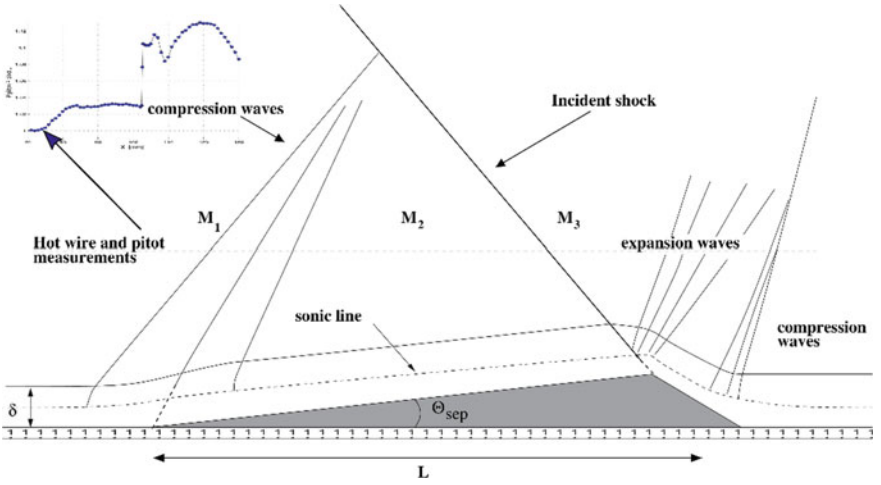

Fig. 30 Sketch of a separated laminar boundary layer interaction and longitudinal Pitot pressure through the interaction, measured at 5 mm from the wall. $P_0 = 0.8$ *atm*, Θ_3

ended by the incident oblique shock wave. The plateau pressure extends downstream from the incident shock up to the expansion wave. The last pressure rise corresponds to the reattachment compression waves.

The flow deviation at the separation point (Θ_{sep}) can be derived from the Pitot measurements, as well as from the Mach numbers downstream from the compression waves (M_2) and from the incident shock (M_3). The length of interaction L is defined as the distance between the extrapolation down to the wall of the center of the compression waves and the incident shock. The associated sketch of the interaction is presented in Fig. 30.

Length scales characterization

The locations of the inflection point of the compression waves and of the incident shock have been carefully evaluated. For the compression waves and the incident shock, the equivalent angles of deviation were derived from Pitot measurements. Then, the extrapolation down to the wall has been evaluated using the theoretical angles of the equivalent shock waves. Additionally, the length L deduced from Pitot measurements and from Hot Wire measurement are in a good agreement. The non-dimensional longitudinal coordinate X^* is used and is defined as:

$$X^* = \frac{X - X_{imp}}{L} \tag{12}$$

The position of the incident shock at the wall is then $X^* = 0$ and the compression waves are centred around $X^* = -1$. An important parameter to evaluate to compare the different experiments is the separation criterion, meaning the minimum pressure jump that separates the boundary layer. The pressure jump required for boundary layer separation is higher in turbulent case than in the laminar one: velocity profiles are fuller near the wall and the boundary layer can sustain larger positive pressure gradients.

Katzer et al. [23] proposed a formula based on free interaction theory to estimate the pressure jump for incipient separation in laminar flow:

$$\frac{p_{inc} - p_0}{p_0} = \frac{1}{2}\gamma M_0^2 K_{inc}\left[C_{f_{imp}} / (M_0^2 - 1)^{1/2}\right]^{1/2} \tag{13}$$

where $C_{f_{imp}}$ is the skin friction coefficient of an undisturbed flat-plate boundary layer at shock impingement x_{imp}, and the subscript 0 designates the upstream conditions. The constant K_{inc} is: $K_{inc} = 1.85\sqrt{2}$.

Others authors have attributed a different value to this constant: for Greber et al. [24], $K_{inc} = 2\sqrt{2}$ whereas Rizzeta et al. [25] proposes $K_{inc} = 1.57\sqrt{2}$. For our conditions, the relation (13) suggests an onset of separation of about 1°. It is worth notice that such small angles are not realized with the current experimental set-up: the flow over the shock generator is blocked. Nevertheless, TU-Delft achieved experiments which seem to validate the relation (13) for large unit Reynolds numbers.

This expression is based on similar assumptions than used to derive the classical Free Interaction Theory (Chapman et al. [26]). This theory suggests that separation

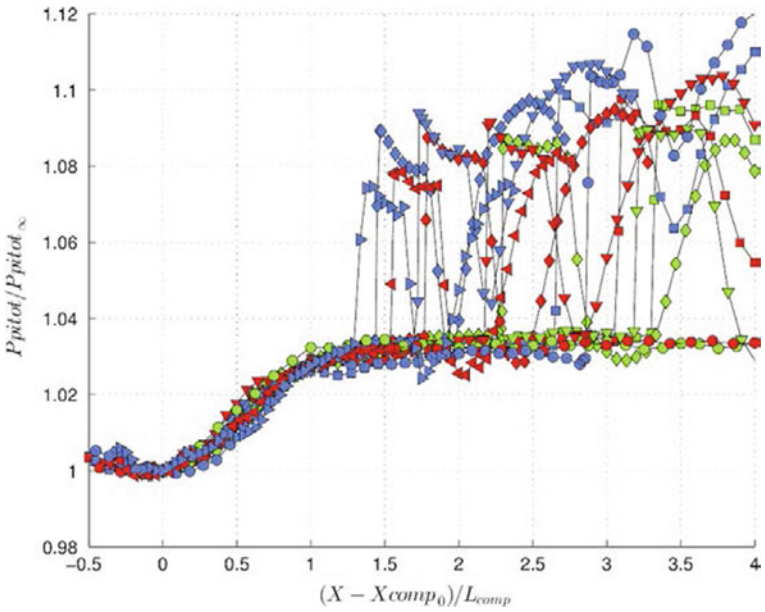

Fig. 31 Longitudinal Pitot profiles measured at $y = 5$ mm from the wall for different stagnation pressures and shock generator angles

conditions (pressure, flow deviation) are independent from the imposed flow deviation (Θ_{sg}): this is clearly verified by the present longitudinal Pitot measurements as shown Fig. 31. The section x is centered on the initial rise of pressure and normalized by the length of compression L_{comp}: the compression waves extend from 0 to 1 in this representation.

In Fig. 32, is plotted the non-dimensional interaction length L/δ^*_{0i} against the separation parameter. The dimensionless separation parameter is calculated as $Se = \Delta p/(p_{inc} - p_0)$. Here, Δp is defined as the equivalent total pressure jump of an inviscid interaction. δ^*_{0i} is the compressible displacement thickness of the unperturbed laminar boundary layer at the location X_0. Experiments with tripping devices (symbols labeled B2 and B3, see 32) are also reported. We notice a very large aspect ratio for all interactions configurations, varying between 120 and 170, and a nearly linear increase of the dimensionless interaction length with the separation criteria.

Mean velocity fields and standard deviation longitudinal velocity profiles are reported on Fig. 33a for several sections along the interaction for a Θ_3 flow deviation and total pressure 0.4 atm. Superimposed on the figure, the blue line represents the location of the 99% boundary layer thickness, and the black line give a first approximation of the recirculation zone: it corresponds to the location of the first positive velocity measured. Technically, in the first part of the recirculation zone, no—or very few- particles are present, and the black line is located at the last position where measurements were possible. At the end of the recirculation, the black line

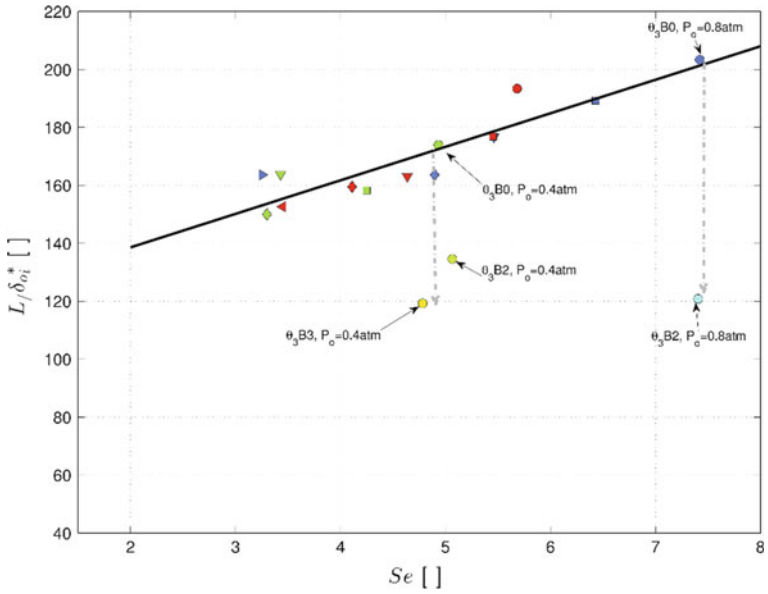

Fig. 32 Influence of interaction strength on separation length. Symbols as Table 4

match the zero-velocity line. The apex (maximum elevation of the separated bubble) is found at $X^* = -0.2$ at $y = 1.3$ mm.

Downstream from the separation point, typical profiles of mixing layer can be observed. The maxima of the longitudinal velocity RMS levels are reported in the figure (magenta curve): they follow an exponential shape. They vary from about 1% of the external upstream velocity (which is the noise level of these LDA measurements) to 17% near the reattachment region. This behavior is in agreement with an amplification of perturbations along the shear layer. The longitudinal evolution of the maxima of the RMS longitudinal velocity fluctuations are reported Fig. 33b. They are normalized with the saturation level (maximum of the RMS along the interaction). An exponential amplification is observed in the second part of the interaction ($X^* > 0.5$). Superimposed on the figure are the IUSTI's LES simulations results for similar interactions. Very similar observations can be derived from numerical results.

Unsteadiness characterization

The LDA measurements provided broadband velocity fluctuations energies. In order to describe in more details the longitudinal amplification of the shear layer fluctuations, hot wire measurements have been carried out. Measurements have been done at $y = 5$ mm above the wall along the interaction to evaluate the pressure fluctuations radiated in the supersonic part of the flow. A longitudinal space correction has been done, using the characteristic angles. The Power Spectral Density (PSD) of the external radiated fluctuations have been documented. We report on Fig. 34 the pre-multiplied PSD for positions located in the upstream boundary layer and

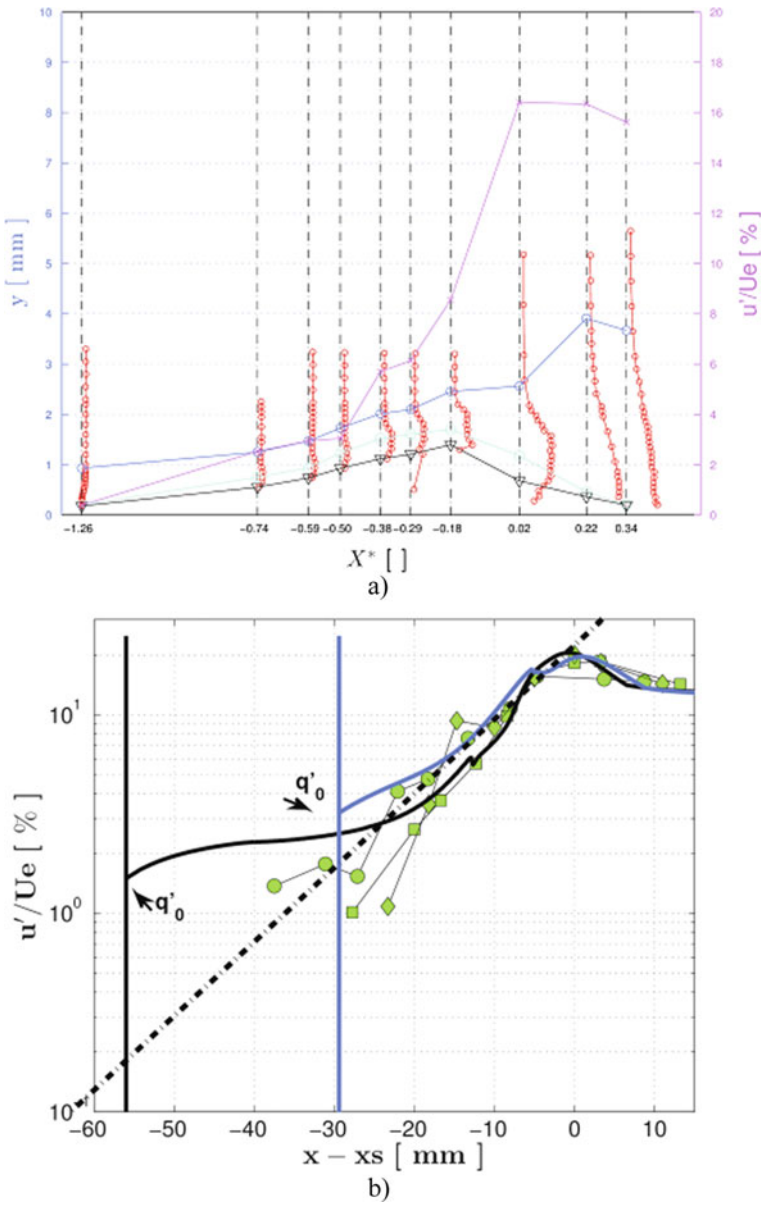

Fig. 33 Turbulent longitudinal velocity LDA measurements with the 38 μm probe volume, Θ_3 angle, $p_0 = 0.4\ atm$. **a** profiles along the interaction; **b** longitudinal evolution of the maxima of RMS along the interaction. Symbols: experiments; lines: Large Eddy Simulations

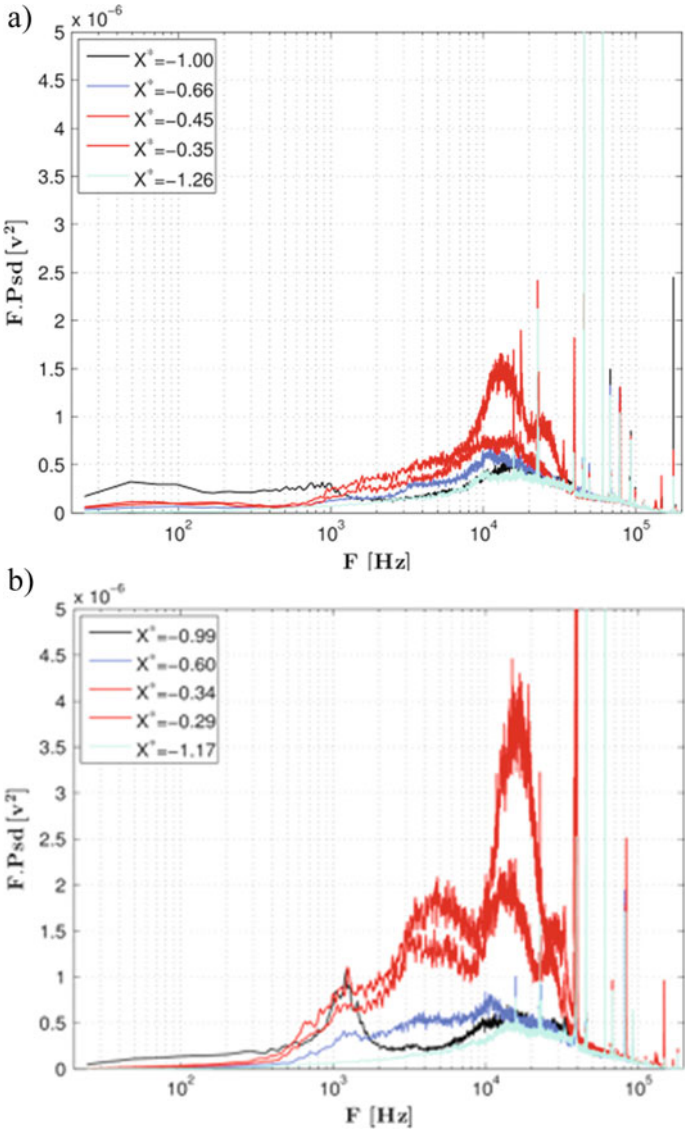

Fig. 34 Pre-multiplied PSD through the interaction for the for the reference flow deviation Θ_1 (**a** $p_0 = 0.4\ atm$, $p_0 = 0.8\ atm$) and for the largest flow deviation Θ_3 (**b** $p_0 = 0.4\ atm$, **d** $p_0 = 0.8\ atm$)

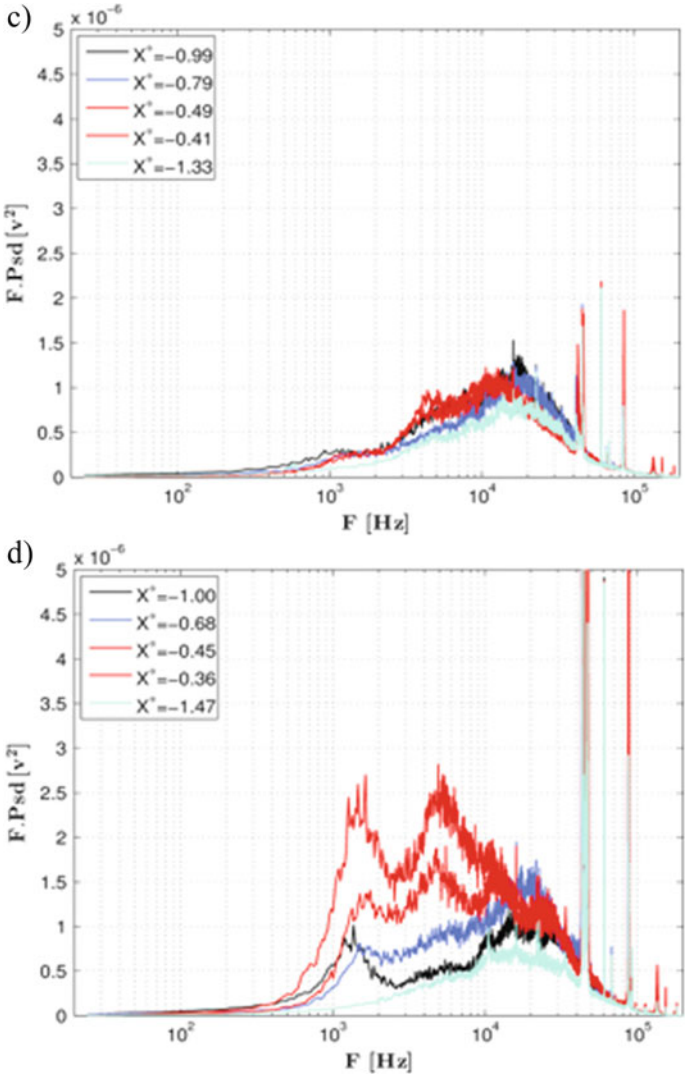

Fig. 34 (continued)

along the interaction, for several stagnation pressure, and for the angles Θ_1 and Θ_3 respectively. In this representation, the energy is proportional to the area under the curve. The upstream boundary layer frequencies ($X^* < -1$) involve energetic scales over 10 kHz, whatever the unit-Reynolds number. For the Θ_1 case, these scales are amplified along the shear regions of the interaction, but lower frequency scales (ranging from 1 to 10 kHz) are also developed. Same results are observable for the largest flow deviation Θ_3. It is clear that for such flow deviation, the amplification rate of the different frequency scales is larger: in case of the largest flow deviation

and largest unit Reynolds number, the low frequency scales ($1 < f < 10$ kHz) become even more energetic than the high frequency scales ($f > 10$ kHz) which were already developed in the upstream boundary layer (see Fig. 34d).

To quantify these different amplification rates, the transfer function $H(f)$ has been evaluated for the same cases as in Fig. 35. The transfer function is defined as the ratio of the local PSD with the referent one, measured in the upstream boundary layer. Results are reported on Fig. 36.

These figures put in evidence the dependence of the amplification rate on the flow deviation. It is also clear that the lowest frequencies (around 1 kHz) are most amplified in the initial compression waves, then are only slightly amplified along the interaction. On the opposite, frequencies between these lowest frequencies and the upstream energetic scales of the boundary layers (frequencies ranging between 2 and 10 kHz) are amplified only in the interaction, downstream from the compression waves.

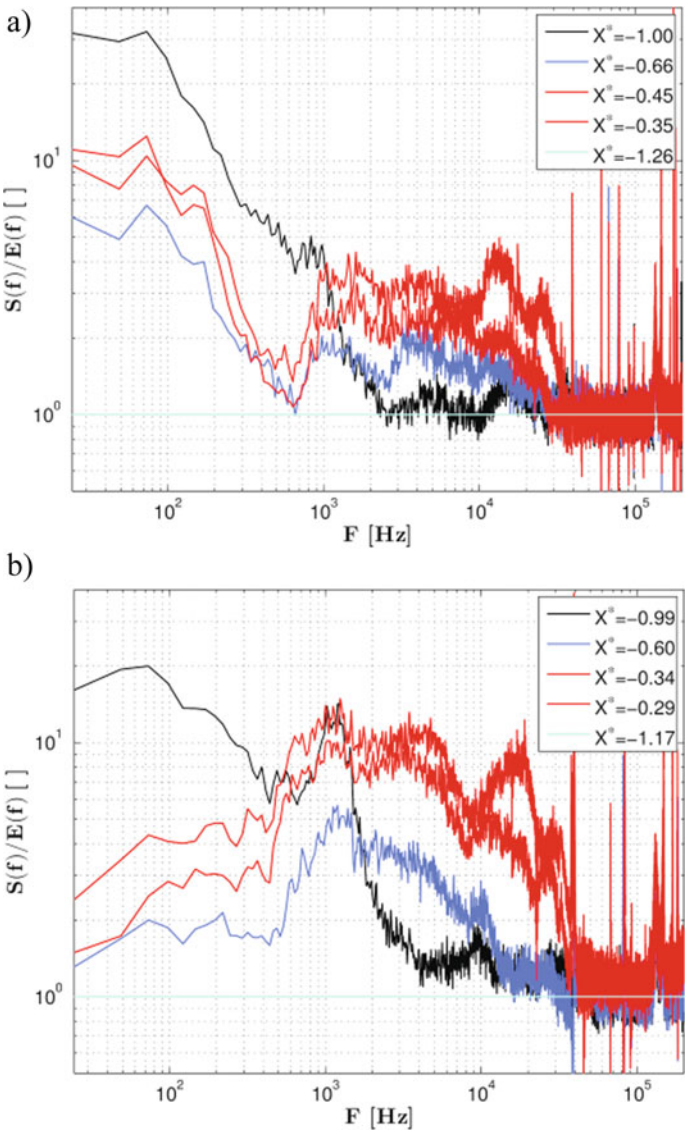

Fig. 35 Transfer function through the interaction for the reference flow deviation (**a** $p_0 = 0.4\ atm$, **c** $p_0 = 0.8\ atm$) and for the largest flow deviation Θ_3 (**b** $p_0 = 0.4\ atm$, **d** $p_0 = 0.8\ atm$)

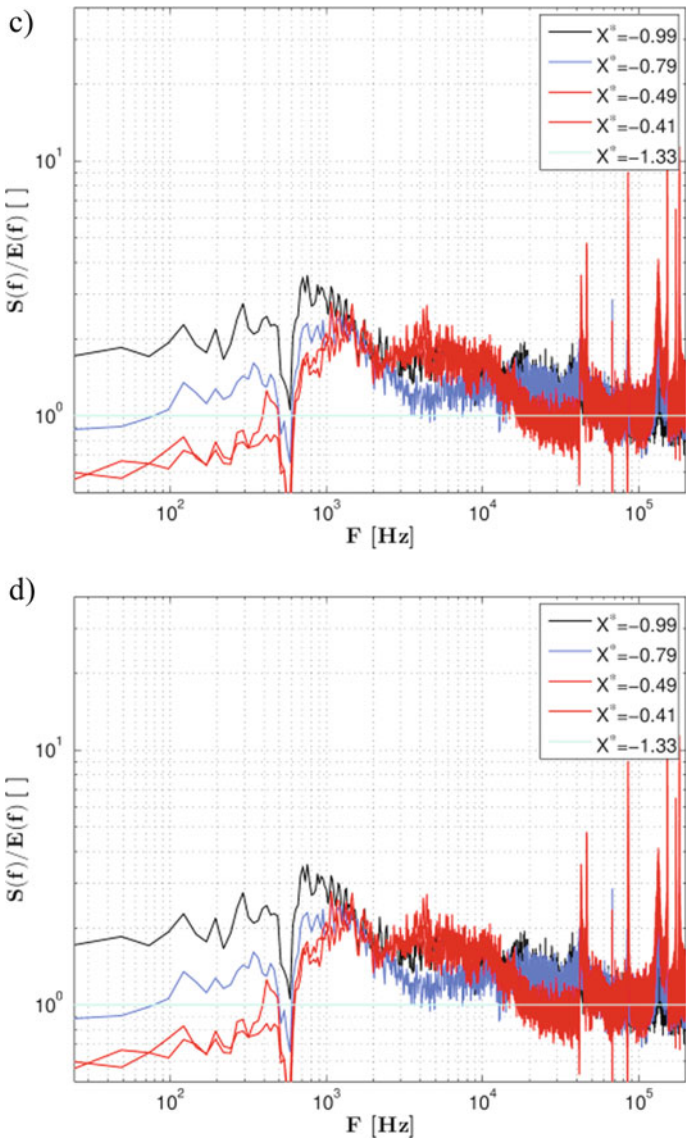

Fig. 35 (continued)

These results show that transitional interactions are clearly unsteady and involve characteristic scales that are about one decade lower than the upstream energetic scales. Moreover, these unsteadiness depend clearly on the flow deviation (or the interaction intensity): the amplification is about 10 time larger for the largest flow deviation.

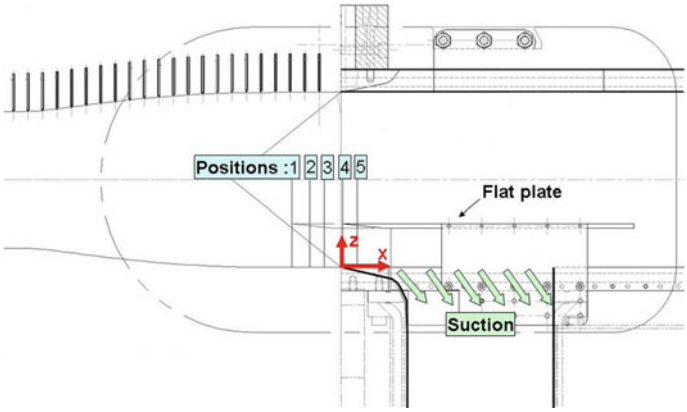

Fig. 36 Sketch of the test set-up with the five flat plate longitudinal positions under study

2.2.2 ONERA-DAFE

Tested configurations and flow parameters under study
Emphasis is placed on parameters influencing the viscous interaction, namely:

- The location of the theoretical (i.e., for a non-viscous flow) shock impingement point by translating the flat plate. This location is characterised by its abscissa X_I from the study plate leading edge, or in a non-dimensional form, by the Reynolds number computed with X_I. For the five longitudinal positions of the flat plate under study (see Table 5), the corresponding values of X_I lead to a related Reynolds number range of: $0.42 \leq Re_{XI}\ (\times 10^6) \leq 1.12$.
- The shock wave intensity, represented by the value of the flow deflection through the incident shock. For each position of the flat plate (and corresponding value of X_I), the angle of attack α of the shock generator wedge is increased from 0 to 5°.

Figure 36 shows a sketch of the test set-up with the flat plate longitudinal positions and the open cavity under the flat plate to control the secondary flow. Table 5 summarizes the longitudinal and vertical positions of the flat plate that have been tested in order to check if the secondary flow is staying supersonic thanks to flow control. For the flat plate at the altitude of $Z = 30$ mm, only three longitudinal positions are available. When the flat plate is at the more upstream location, the secondary flow is choked. On the contrary, when the flat plate is moving in the downstream

Table 5 Longitudinal and vertical positions of the flat plate under study

Z(mm)\X(mm)	−33.95	−21.6	−11.45	0.9	11.05
30		×	×	×	
40	×	×	×	×	×
50	×	×	×	×	×

direction, it is very difficult to start the wind tunnel because the static pressure in the cavity is of the same order as in the test section ahead of the flat plate, i.e., too weak with respect to the auxiliary pumps capacity. When the flat plate is elevated to $Z = 40$ and 50 mm, the needed minimum value of the suction mass flow rate is decreasing and, so, the range of longitudinal locations of the flat plate is increasing from $X = -33.95$ mm to $X = 11.05$ mm. Moreover, the reflected shocks could disturb the flow in the vicinity of the flat plate in a more upstream region if the flat plate is at the altitude of $Z = 50$ mm. Then, the retained altitude of the flat plate is at $Z = 40$ mm for the five longitudinal positions under study (see Table 5). The leading edge of the shock generator wedge is located near the test section entrance plane, at $X = 3$ mm and $Z = 84.5$ mm.

Detection of the natural boundary layer transition on the flat plate

Before testing the shock wave impact on the boundary layer properties, a detection of the natural transition location on the flate plate is carried out by removing the shock generator wedge from the test set-up.

Figure 37 shows a Schlieren visualization of the flowfield along the flat plate under study. Reflected oblique waves under the flat plate indicate that the secondary flow is staying supersonic. The reflection (barely visible) on the upper wall of the oblique shock emanating from the flat plate leading edge (i.e., a Mach wave) is far downstream of the flat plate. However, one has to take care to perturbations emanating from compression waves generated by the junction between the nozzle exit and the test section walls: they accelerate the triggering of the boundary layer transition. Moreover, the Schlieren apparatus is adjusted with the vertically-oriented

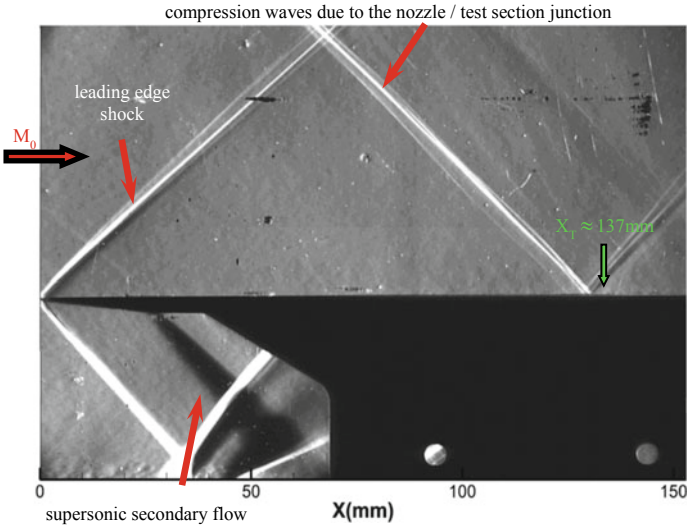

Fig. 37 Schlieren visualization used to detect the natural transition of the flat plate boundary layer

knives position in order to mainly visualize the X-gradient of the flow and, then, to point out the emergence of vortex structures in the boundary layer transition region.

Finally, the transition « point » of the boundary layer is estimated at $X_T \approx 137$ mm from the flat plate leading edge, which may in fact correspond to the end of the transition process (see the green arrow location on Fig. 37). So, the corresponding Reynolds number of transition is equal to: $Re_{XT} \approx 1.9 \times 10^6$.

This first result on the boundary layer transition location has to be strengthened by IR thermography and TSP measurements on the flat plate. Indeed, the transition process is developing along the plate according to a longitudinal range $[X_t, X_T]$. This range is obtained by extracting some temperature profiles along the plate near the mid-span test section. At the abscissa X_t, it corresponds the starting process of transition with a rapid increase of the wall temperature and at the abscissa X_T, the wall temperature does not change which means the end of the transition process and the emergence of vortex structures visible in the Schlieren visualization.

Main results obtained by both IR thermography and TSP measurements are shown in Figs. 38 and 39, respectively. Figures 38a and 39a show a IR thermography image and a TSP one on the flat plate (its leading edge being at $X = 0$) obtained after a registration process and scaled in temperature. For both measurements, the boundary layer seems to stay laminar at least for $X \leq 95$ mm (colour moving from blue to red), then the wall temperature is increasing due to the starting of the transition process. Moreover, a spanwise evolution of the temperature is observed due to the sidewall boundary layers contamination.

A more precise analysis is carried out by extracting the temperature profile along the mid-span of the flat plate (at $Y = 0$, see Figs. 38b and 39b), and by quantifying the slope variation in using its derivative versus the longitudinal direction, $\partial T/\partial X$. At the beginning of the plate (for $X \leq 20$ mm, not plotted here), temperature is rapidly decreasing from the stagnation temperature value to an equilibrium value behind the leading edge shock. Near $X = 30$ mm, temperature fluctuations are observed for the TSP case: at this abscissa starts the paint of the flat plate, which generates a compression wave clearly visible on the Schlieren visualization (see Fig. 39a). This low-intensity wave does not affect the flow properties; the boundary layer is in a laminar state and the temperature is staying at the same value since $X = 40$ mm. However, the longitudinal evolution of the temperature is very sensitive to the plate flatness: one notices a temperature variation from $X = 40$ to 85 mm due to a slight bump-shaped form of the Ino $\times$ 304 L plate used for IR thermography measurements (see Fig. 38b). Then, temperature is increased for $X > 95$ mm which means that the transition process has started, and the increasing is stopped around $X = 125$ mm, just downstream of the impingement of compression waves emanating from the nozzle/test section junction. Finally, the longitudinal range for the transition region $[X_t, X_T]$ is estimated by both measurement techniques around 30 mm. The temperature drop ΔT during the transition process is measured at 1.5° by IR thermography and at 2.5° by TSP. For comparison, the Crocco's law based on adiabatic assumption of the flow gives: $\Delta T \approx 5°$ at Mach number of 1.6. Finally, the Reynolds number Re_{Xt} related to the starting process of transition is equal to 1.3×10^6 and the one Re_{XT} related to the end of transition is estimated in the range of 1.75×10^6 to 1.9×10^6.

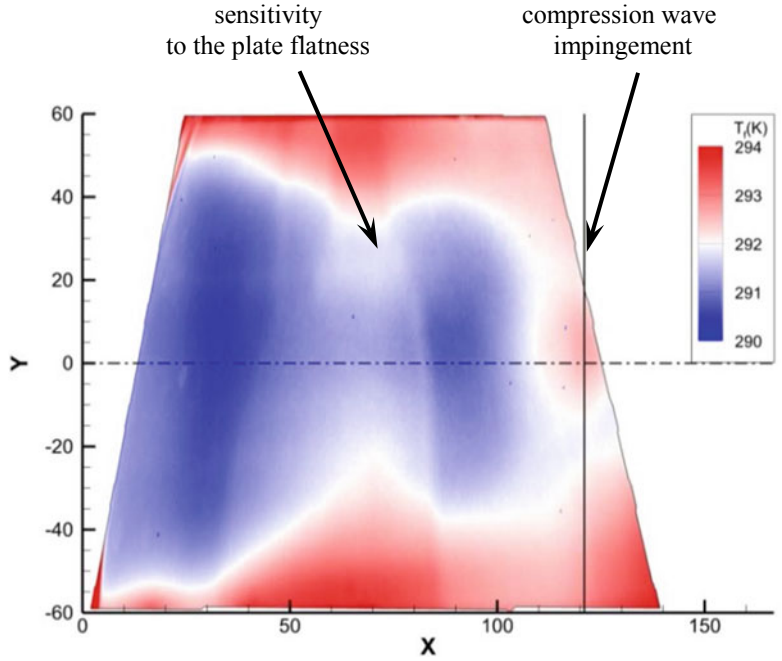

a - IR thermography image

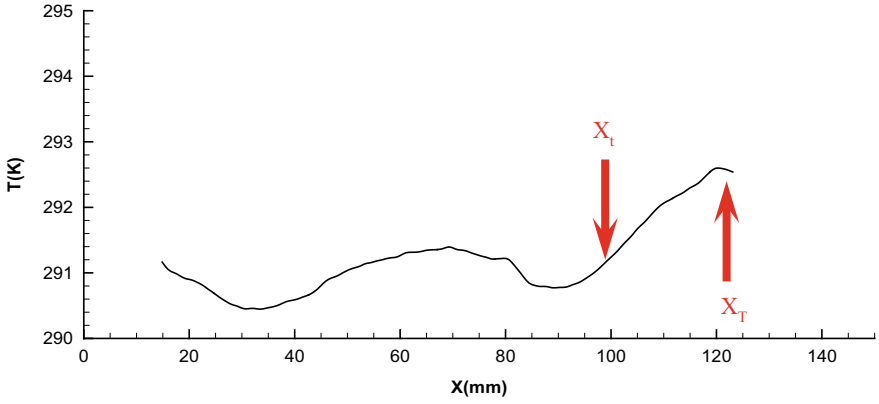

b - Temperature profiles along the mid-span of the flat plate (Y = 0)

Fig. 38 Infra-red thermography measurements. **a**—IR thermography image, **b**—Temperature profiles along the mid-span of the flat plate (Y = 0)

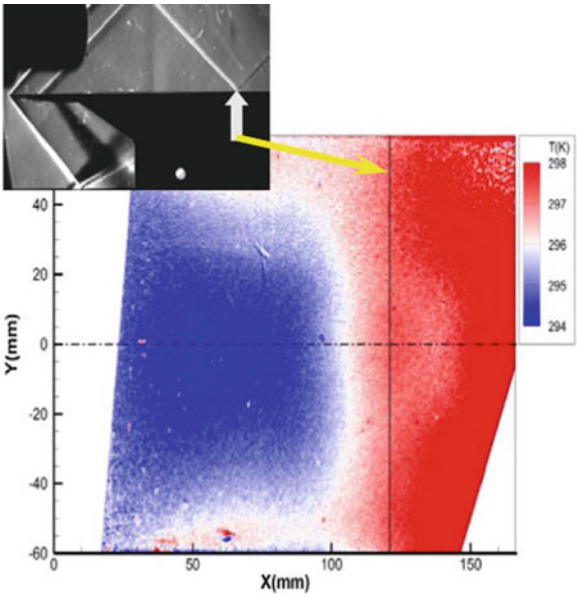

a - TSP image (with corresponding Schlieren visualization)

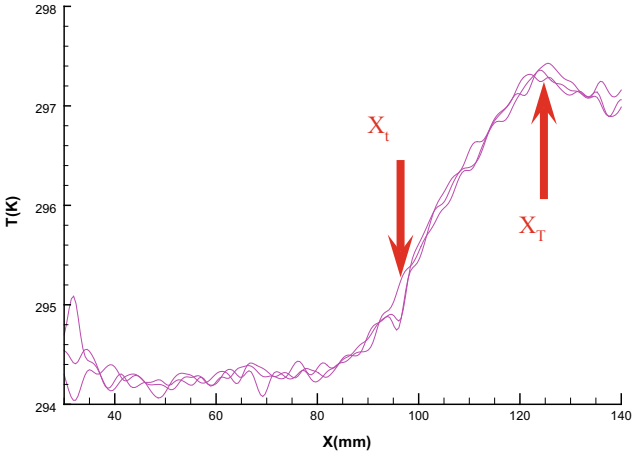

b - Temperature profiles along the mid-span of the flat plate (Y = 0)

Fig. 39 Temperature Sensitive Paint measurements. **a**—TSP image (with corresponding Schlieren visualization). **b**—Temperature profiles along the mid-span of the flat plate (Y = 0)

Shock intensity effect and flat plate location influence on the boundary layer transition

Effect of the impinging shock intensity

Figure 40 shows Schlieren visualizations for a fixed flat plate location near the test section entrance plane, at $X = 0.9$ mm (see on Table 6), and for several angles of attack of the shock generator wedge (from $\alpha = 1.5°$ to 4°) to quantify the effect of the impinging shock intensity on the incoming boundary layer. For these configurations, the Reynolds number based on the impact location of the oblique shock on the flat plate, X_I, is nearly constant and equal to: Re_{XI} 0.61×10^6. In fact, a slight

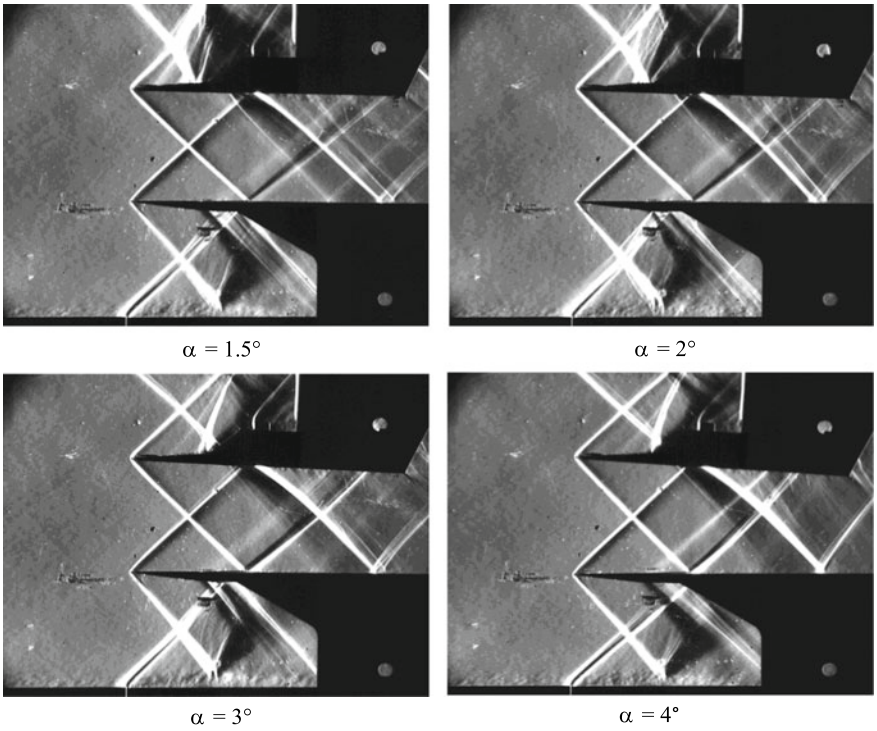

Fig. 40 Schlieren visualizations for a fixed flat plate location at X = 0.9 mm. Effect of the impinging shock intensity—$Re_{XI} \approx 0.61 \times 10^6$

Table 6 Evolutions of the boundary layer separation (X_S), the shock impingement (X_I) and the transition point (X_T) abscissas with respect to the shock intensity (α)

α(°)	1.5	2	3	4
X_S (mm)	34	33	32	31
X_I (mm)	46	45	44	43
X_T (mm)	55	53	47	43

displacement of X_I around its mean location when the angle of attack α varies is inherent to the experimental arrangement in which the shock intensity is adjusted by a simple rotation of the shock generator wedge. The apparent spreading of the shock waves observable in the pictures is due to the interaction with the boundary layer of the test section sidewalls. Experiments confirm that the destabilization of the laminar boundary layer in the interaction domain linked to the shock reflection has a determining effect on transition, which in turn can notably modify the flow structure. Moreover, the turbulence of the non-viscous part of the flow is modified by the crossing of the shocks.

As illustrated in Table 6, an in-depth analysis of the images indicates that the laminar boundary layer is separated due to the impact of the shock wave, even for the weaker shock strength tested ($\alpha = 1.5°$); the interaction length is growing with the shock intensity. For very small shock intensities ($\alpha = 1.5°$ and $2°$), a laminar course seems to remain downstream of the interaction domain which is typically laminar with incipient separation. An expansion fan is generated by the propagation of the shock in the boundary layer and induces, as the incident shock, a deviation of the flow towards the wall. The initial direction is finally recovered through a spread out compression. If the shock intensity is progressively increased, transition very rapidly moves upstream and reaches the interaction domain to which it remains attached for moderate shock intensity corresponding to $\alpha \geq 3°$. Then, its upstream displacement becomes very slow and is strongly linked to the increasing extent of the interaction region. For the strongest shock strength tested ($\alpha = 4°$), one observes a laminar separation well upstream of the shock impact with an associated compression wave propagating in the outer flow, and the emergence of large vortex structures behind the interaction domain. The destabilisation due to separation and the extent of the separated region is sufficient for the compression at reattachment to trigger transition. So, the perturbation imparted by the shock to the boundary layer contributes to the destabilisation process and to the creation of turbulence.

Influence of the flat plate location

Figure 41 shows Schlieren visualizations for a fixed shock intensity (angle of attack of the shock generator wedge equal to: $\alpha = 3°$), and for several flat plate locations corresponding to a range of Reynolds number at the shock impact point: $0.61 \times 10^6 \leq Re_{XI} \leq 1.09 \times 10^6$. This range of the Reynolds number allowed by the test set-up was roughly equal to half the values for the natural transition range, ignoring the small values of X_I which would introduce a coupling between shock interaction and leading edge phenomena.

As summarized in Table 7, transition is always attached to the viscous interaction during which it takes place for all the tested Reynolds number Re_{XI}. It reveals that the transition abscissa X_T is close to the abscissa X_I of the theoretical reflection and that the Reynolds number effect is almost inexistent. Moreover, the distance between the separated point X_S and the impingement point of the shock X_I is growing when the incoming boundary layer is developed on a greater longitudinal range. This means that the size of the laminar separated bubble, and associated viscous domain, is increasing with the Reynolds number Re_{XI}.

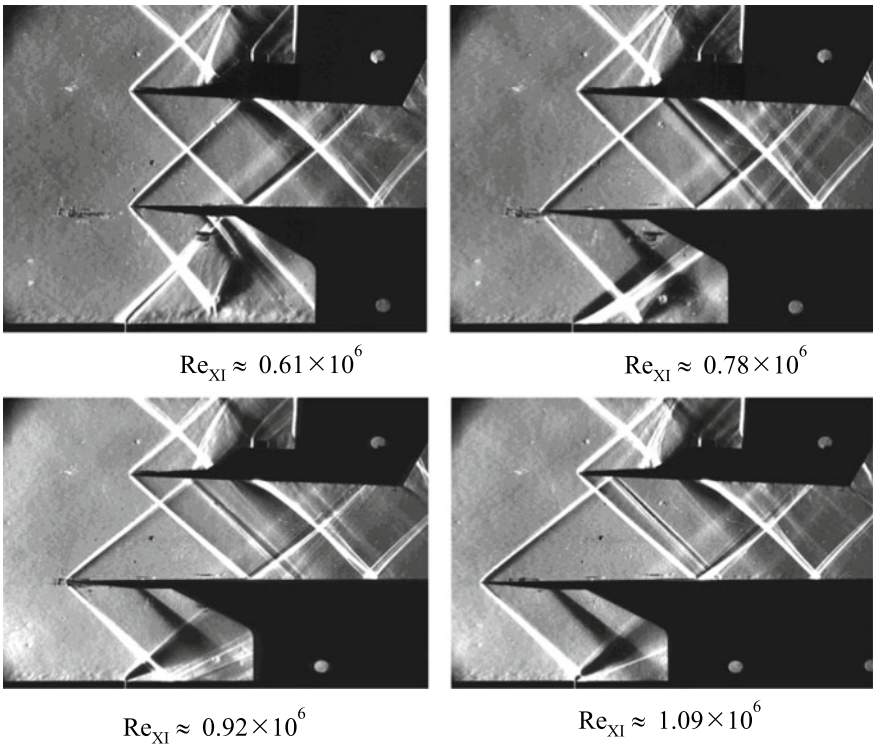

Fig. 41 Schlieren visualizations for a fixed shock intensity (alpha = 3°). Influence of the flat plate location and related Reynolds number at the shock impact point Re_{XI}

Table 7 Evolutions of the boundary layer separation (X_S), the shock impingement (X_I) and the transition point (X_T) abscissas with respect to the Reynolds number at the shock impact point (Re_{XI})

$Re_{XI} \times 10^6$	0.61	0.78	0.92	1.09
X_S (mm)	32	42	51	60
X_I (mm)	44	56	66	78
X_T (mm)	47	59	69	79

Analysis by an inviscid flow approach

The shock intensity could be represented in a more quantitative approach by computing the pressure ratio p_2/p_0 (state *0* for the upstream condition, state *2* for the condition downstream of the shock system; see sketch of the flow on Fig. 42), using the Rankine-Hugoniot equations for the oblique (incident and reflected) shocks.

Then, analysis of results concludes that the transition « point » is located in the interaction region (the transition abscissa X_T being nearly coincident with the shock impingement abscissa X_I) for moderate shock intensities obtained with: $\alpha \geq 3°$, which corresponds to pressure ratio values: $p_2/p_0 \geq 1.35$.

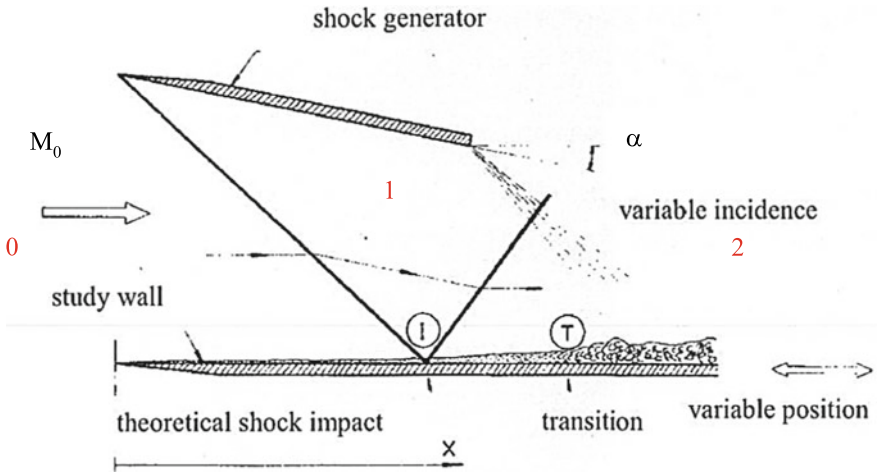

Fig. 42 Sketch of the investigated flow

Conclusions

An experimental study on a Mach 1.6 shock-wave/boundary layer interaction in a channel flow has been performed to analyze the transition process of the boundary layer growing on a flat plate. The detection of the boundary layer transition region is obtained by Schlieren visualizations, IR (Infra-red) thermography and TSP (Temperature Sensitive Paint) measurements, whose cross-checking of results allows to accurately determine the transition on the flat plate. Flow analysis shows that the transition process is not very sensitive to the flat plate boundary layer growth, but is strongly dependent to the oblique shock intensity. In fact, transition moves upstream and reaches the viscous interaction region for a moderate shock intensity given by the angle of attack of the shock generator wedge equal to 3°, which corresponds to a pressure ratio through the incident-reflected shock system of 1.35. Beyond this value, one concludes that the shock-wave triggers the transition.

2.2.3 TUD

Free stream turbulence level

Mass flux and velocity fluctuations in the free stream were measured by means of HWA and PIV, respectively. The perturbations in the freestream mass flux are mostly of an acoustic nature. The HWA measurements conducted at high overheat ratio (0.93) provide fluctuation levels of $(\rho u)' = 0.77\%$ of the freestream mass flux, yielding $p' = 1.9\%$ of the freestream pressure. Furthermore, from PIV measurements with a long pulse separation distance it was found that $u'/U_\infty = 0.57\%$ and $v'/U_\infty = 0.43\%$. For more information regarding the assessment of the free stream turbulence level the reader is referred to [27].

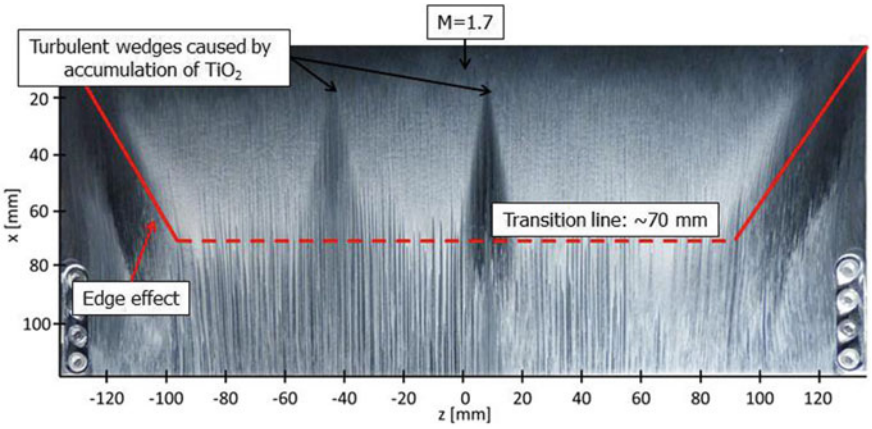

Fig. 43 Oil flow visualization for natural transition without shock interaction

Natural transition location

The transition location has been determined with four different methods: oil flow visualization, spark-light Schlieren visualization, infrared thermography, and particle image velocimetry. Results of the first two methods are given directly below; the infrared approach is not addressed here for brevity (but can be found in [28] while the PIV measurements will be described in the subsequent section in connection to the boundary layer characterization.

The oil flow visualization pattern in Fig. 43 indicates that boundary layer transition occurs at approximately 70 mm from the leading edge of the plate. A nominal 2D transition front is obtained over a spanwise length of ± 90 mm away from the centreline (~66% of the plate span). Clearly visible in the image are two turbulent wedges that originate close to the leading edge of the plate and which are triggered by small agglomerations of TiO_2 pigment particles in the oil film applied to the surface. These are not caused by plate imperfections, as they appear on different locations for different runs.

The spark-light Schlieren measurement visualizes instantaneous turbulent features in the flow and therefore allows to distinguish the laminar from the turbulent part of the boundary layer based on the granularity of the features detected therein. The transition location is found (see Fig. 44) to fluctuate between 55 and 65 mm during the course of a wind tunnel run. The Schlieren image presents a spanwise averaged image of the flow and any turbulent portion on the plate will overshadow the laminar portion of the plate. The Schlieren images therefore are indicative of the transition onset location x_T, rather than the average (50% intermittency) transition location $x_\gamma = 0.5$.

The results for the transition region characterization by the four different techniques are summarized in Table 8. The transition onset location x_T is found to be 55 mm ($Re_{x_T} = 1.9{\cdot}10^6$) from both the spark-light Schlieren visualizations and the PIV measurements. The average transition location $x_{\gamma=0.5}$ has been determined by

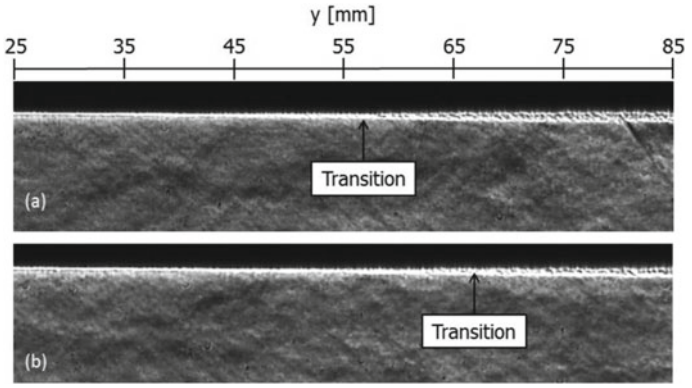

Fig. 44 Spark-light Schlieren visualization of boundary layer transition. Two snapshots are shown to illustrate the intermittent behaviour of the transition region

Table 8 Comparison of the transition locations found with the four different techniques

	x_T	$x_{\gamma=0.5}$	L	$dx_{\gamma=0.5}/dT_w$
Spark-light Schlieren	55 mm			
Oil-flow visualizations		70 mm		
Infrared thermography		68 mm		0.6 mm/°C
Particle image velocimetry	55 mm	71 mm	35 mm	

three techniques (oil-flow visualization, infrared thermography and PIV) and equals approximately 70 mm ($Re_{x_{\gamma=0.5}} = 2.5{\cdot}10^6$). From PIV also the transition length L has been obtained, which equals 35 mm. This implies that the process of transition approximately extends over the region of x = 55 to 90 mm on the flat plate, or in terms of Reynolds numbers from 1.9 to $3.2{\cdot}10^6$. Finally, infrared thermography also delivered the sensitivity of the average transition location to the average upstream wall temperature, as ~0.6 mm/°C.

Boundary layer characterization:
High-resolution PIV was applied to characterize the boundary layer. The measurements were performed with two Imperx Bobcat IGV-B1610 cameras. These cameras have a CCD chip of 1624 × 1236 pixels, which is cropped in the wall normal direction from 1236 to 651 pixels to speed up the data acquisition process (acquisition frequency of 10.2 Hz). The cameras are operated at a magnification of 0.57 and a spatial resolution of 130 pixels/mm. A major advantage of these cameras is the very short interframe time of 430 ns that can be achieved. At the given spatial resolution, this value results in a freestream particle displacement of ~24 pixels between frames. Illumination is provided by a double-pulse Nd:YAG Spectra Physics Quanta Ray PIV-400 laser, which is operated at a laser power of 140 mJ per pulse. The pulse duration is less than 7 ns, which translates into a particle displacement during illumination of less than 0.4 pixel and therefore incurs negligible particle blur. The

flow is seeded with TiO_2 particles (30 nm crystal size), which have a response time of 2.5 μs.

In view of the very small boundary layer thickness only a limited number of pixels is available that can be used to reconstruct the velocity profile. At 40 mm from the leading edge, the laminar boundary layer is ~0.2 mm thick, which at the given spatial resolution of 130 pixels/mm translates into just 26 pixels. So, for that reason elongated interrogation windows of 8 × 256 pixels were used, which size corresponds to 0.06 mm in the wall normal direction and 1.97 mm in the streamwise direction. A window overlap of 75% was used in the streamwise direction and an overlap of 87.5% was used in the wall normal direction, resulting in vector pitches of 7.7 μm and 0.49 mm, respectively. Before applying cross-correlation to obtain the velocity fields, several pre-processing steps were applied to correct the images for camera read-out noise, plate vibration and large differences in particle intensities [27]. Because of the thin interrogation windows and the relatively low seeding density close to the wall, it is not possible to determine the instantaneous velocity field from a single image pair. Instead an ensemble correlation approach is used, which cumulatively builds up the correlation plane by calculating and summing up the correlation results for all the image pairs. All of the processing is performed with an in-house iterative multi-grid window-deformation PIV code (Fluere).

To track the development of the complete boundary layer 12 field of views are combined. For every run, two cameras were operated simultaneously, one on each side of the tunnel, with a typical overlap of 4 mm between the cameras FOVs to allow stitching of the velocity fields. A total of 300 image pairs was obtained per location.

The major challenge of the PIV measurements proved to be the adequate seeding of the boundary layer. Using a TiO_2 seeder operated at an overpressure of 1 bar with respect to the pressure in the settling chamber, a satisfactory seeding density of 60–70 particles per mm^3 was obtained for the freestream. Figure 45 shows the seeding distribution over the flat plate and is obtained by calculating the maximum number of counts minus the minimum number of counts per pixel location for the entire dataset. This visualization shows that for the upstream laminar part boundary layer, no seeding is present in the near-wall region, while further downstream the seeding distribution is homogenized by the mixing that takes place in the turbulent boundary layer.

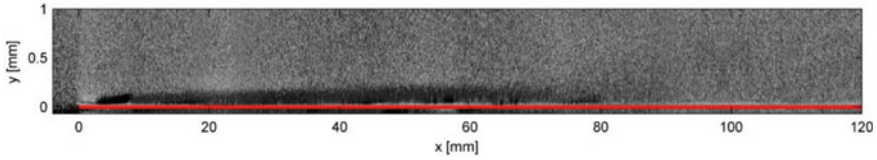

Fig. 45 Seeding distribution along the flat plate. The red line indicates the location of the wall

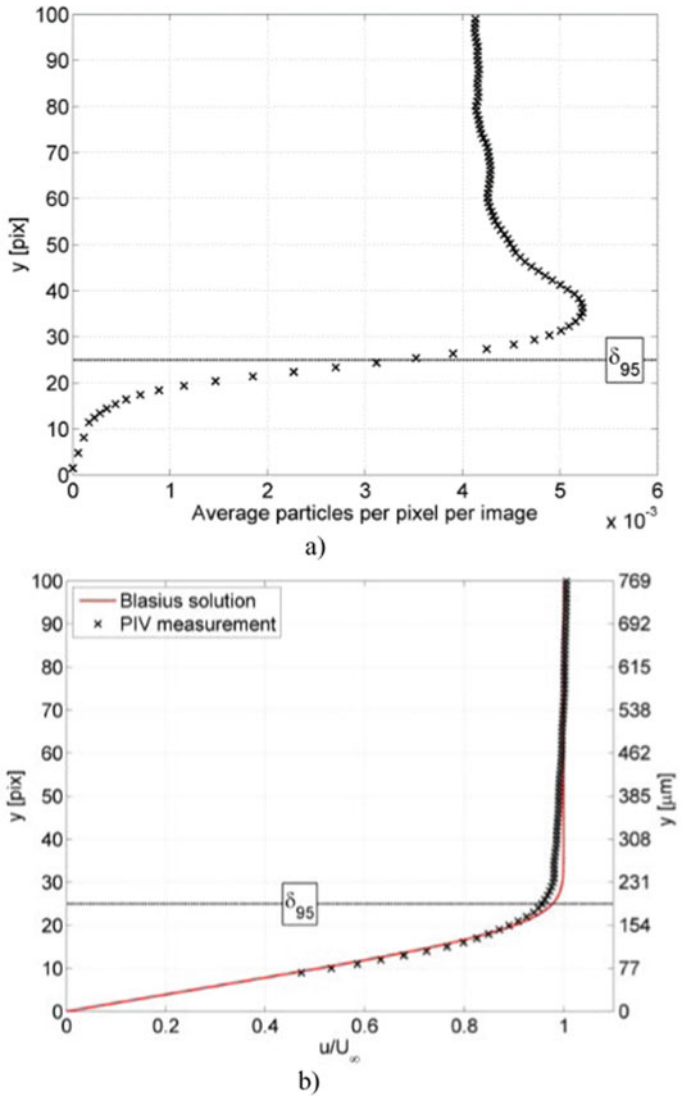

Fig. 46 Average particle distribution in the laminar boundary at x = 40 mm (**a**) and the corresponding velocity profile (**b**)

Figure 45 shows that the gap without seeding gradually disappears in the region of 60 to 80 mm from the leading edge, which agrees with the transition region determined by the other experimental techniques. This visualization provides an averaged view of the laminar-to-turbulent transition process. Inspection of the individual images reveals an intermittent behaviour, in that the gap is present in some images and absent in others. To quantify this intermittency, the ppp levels were calculated

in windows covering the region from 5 to 15 pixels away from the wall for every individual image. If the ppp level in the window has a value higher than 30% of the freestream ppp level for that particular image, the boundary layer state is qualified as turbulent and otherwise as laminar. Figure 47 shows the results of this analysis and indicates a smooth transition taking place over approximately 35 mm. The distribution exhibits an inflection point around x = 71 mm, at an intermittency level of 50%. The experimental data is compared to the semi-experimental/semi-theoretical intermittency distribution of Dhawan and Narasimha [29].

A further illustration of the seeding distribution is given in Fig. 46a, which shows the average pixel density at 40 mm from the leading edge. Virtually no seeding is detected in the first 10 pixels from the wall (~40% of δ_{95}), whereas just outside of the boundary layer an accumulation of migrated particles is found. Notwithstanding that the lower 10 pixels provide virtually no information, the remaining 15 pixels still allow to extract the upper 60% of the boundary layer profile. The resulting boundary layer profile is presented in Fig. 46b in comparison to the compressible Blasius solution, with properties documented in Table 9.

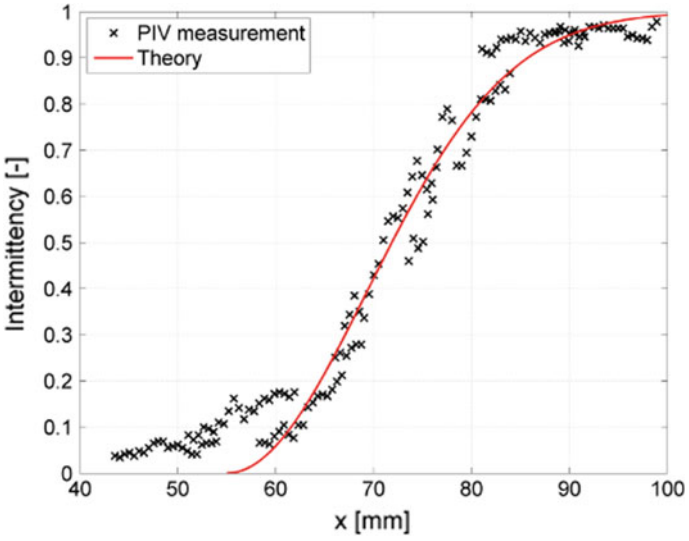

Fig. 47 Development of the intermittency throughout the transition region

Table 9 Boundary layer properties at $x = 40$ mm

	PIV	Blasius
δ_i^*	87 ± 5 μm	80 μm
θ_i^*	30 ± 2 μm	29 μm
H_i	2.9 ± 0.1	2.7
δ_{95}	200 ± 8 μm	170 μm

The development of the integral parameters of the undisturbed boundary layer, in terms of the incompressible displacement thickness δ_i^*, incompressible momentum thickness θ_i and the incompressible shape factor H_i, is displayed in Fig. 48. To obtain these parameters for the laminar part, the velocity profile close to the wall was extrapolated using the compressible Blasius solution. The shape factor has a value of approximately 2.9 at 40 mm from the leading edge and from 55–85 mm

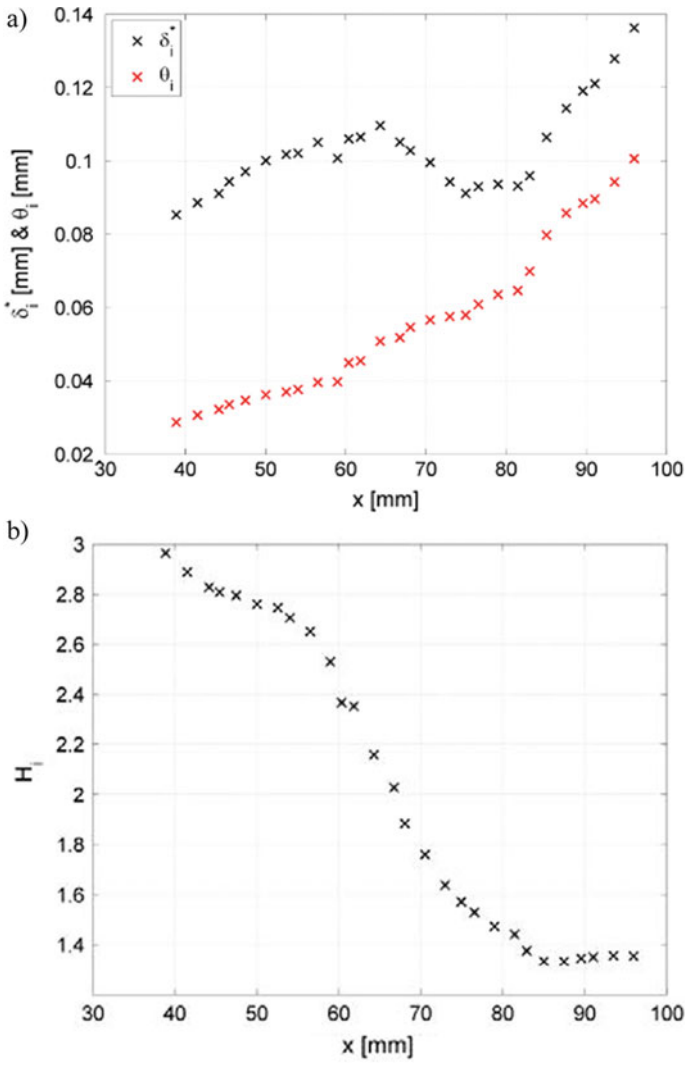

Fig. 48 Development of the integral parameters. Incompressible momentum ϑ_i and displacement thickness δ_i^* (**a**) and incompressible shape factor H_i (**b**)

displays a gradual decrease to a value of ~1.35, which are typical values for laminar and turbulent boundary layers, respectively.

Oblique shock wave reflection under natural transition conditions

To study the effects of boundary layer transition on an oblique shock wave reflection, three inflow conditions were considered: a laminar, transitional ($\gamma \sim 50\%$) and turbulent boundary layer, depending on the state of the undisturbed boundary layer at the shock impingement location.

For these cases, the incident shock wave (3° flow deflection angle) was positioned at, respectively, $x_{sh} = 51$, 71 and 101 mm from the leading edge. Schlieren visualizations of these cases are given in Fig. 49, while the mean velocity fields as measured with PIV are compared in Fig. 50.

For the **laminar case** (Fig. 51a) a large separation bubble is present which starts 8 mm upstream of the incident shock impingement location and ends 5 mm downstream. The total bubble length (10.5 mm) corresponds to approximately 110 times

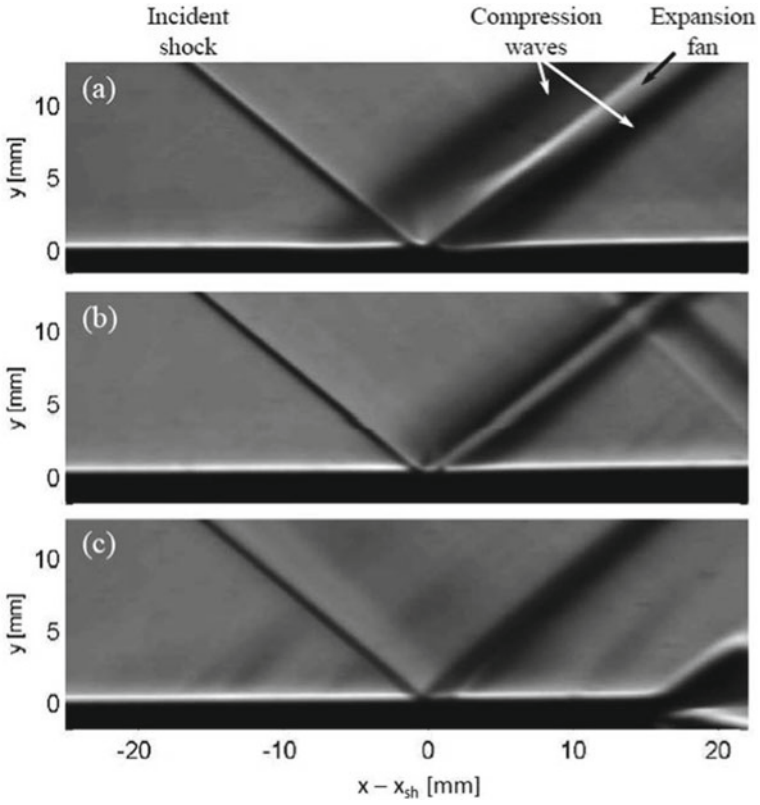

Fig. 49 Schlieren visualizations of an oblique shock wave reflection ($\theta = 3°$) with a laminar boundary layer, $x_{sh} = 51$ mm (**a**) a transitional boundary layer, $x_{sh} = 71$ mm (**b**) and a turbulent boundary layer, $x_{sh} = 101$ mm (**c**)

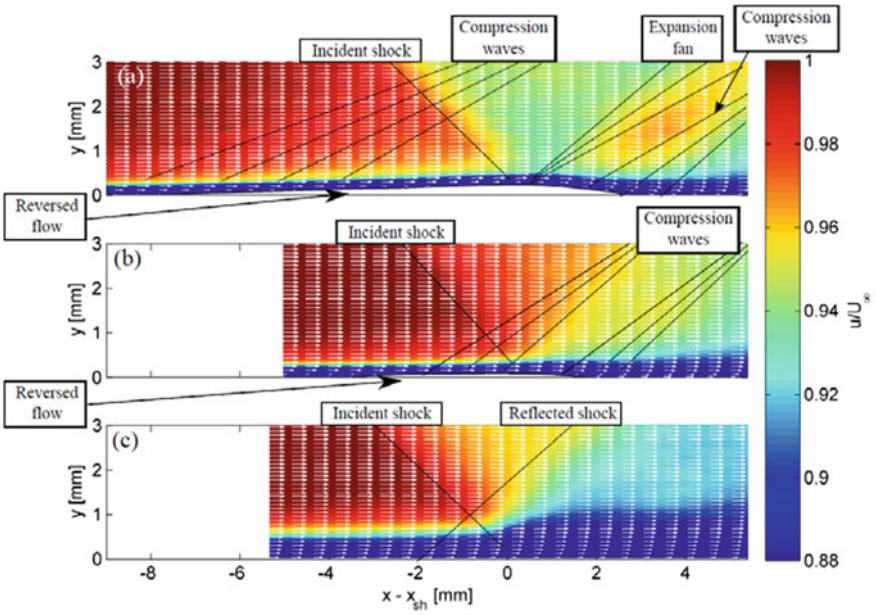

Fig. 50 Average velocity field of an oblique shock wave reflection with an incoming laminar (**a**), transitional (**b**) and turbulent (**c**) boundary layer. The corresponding shock locations are, respectively, $x_{sh} = 51$, 71 and 101 mm

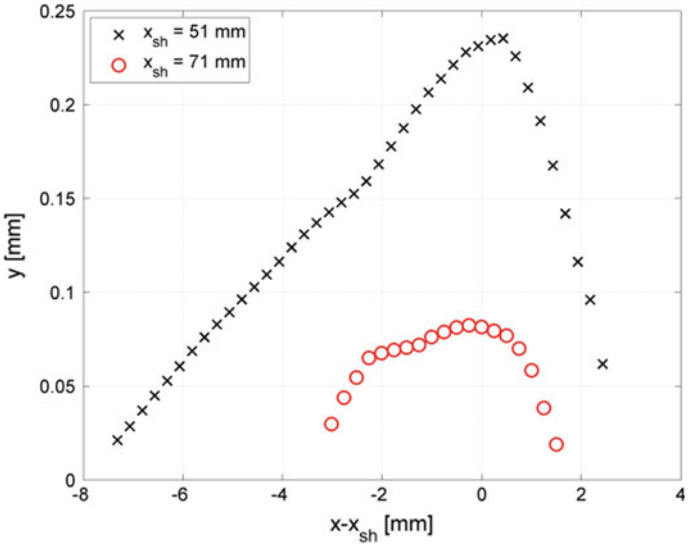

Fig. 51 Comparison between the size of the reversed flow region for an oblique shock wave reflection for a laminar and transitional incoming boundary layer

the displacement thickness δ^* recorded at $x = 40$ mm. The incoming laminar boundary layer is lifted over the separation bubble and remains in a laminar/transitional state up to the impingement location of the incident shock ($x \approx x_{sh}$), after which it undergoes transition and reattaches at the wall as a turbulent boundary layer. The displacement of the outer flow associated to the formation of the separation bubble results in the formation of subsequent series of compression and expansion waves. These features are typical for a separated laminar shock wave-boundary layer interaction and were also observed in the Schlieren visualizations.

The **transitional case** (Fig. 50b) also shows a region of reversed flow, though much smaller than for the laminar case. From the mean velocity field two regions of compression can be distinguished, one starting upstream of the incident shock wave and the other is formed around the reattachment location of the separation bubble. Similar observations were also made in the Schlieren and oil-flow visualizations for this configuration. Both techniques also indicate that the separation bubble is smaller for the transitional case than for the laminar case and that the compression waves are confined to a smaller region.

For the **fully turbulent interaction** (Fig. 50c) no separation is detected in the average velocity field, which is according to expectations based on theory. The inviscid pressure ratio that is imposed by the oblique shock wave reflection equals $p_3/p_\infty = 1.35$, whereas according to the free-interaction theory, a pressure ratio of at least $p_3/p_\infty = 1.77$ would be required to separate the turbulent boundary layer. Also the oil-flow visualizations (see section 4) that were performed for this configuration showed no indication of boundary layer separation.

The seeding difficulties that were encountered when investigating the undisturbed boundary layer were also present when investigating the laminar and transitional interactions. This factor, amongst others, prevents from obtaining an accurate estimate of the velocities inside the separation bubble under the present conditions. Therefore, a Falkner-Skan based extrapolation procedure was applied to the available velocity profile data to provide an estimate of the $u = 0$ isoline position. These results, indicative of the bubble shape are compared in Fig. 51 for the laminar and transitional case. The separation bubble for the laminar interaction is longer (10.5 vs. 5.3 mm) and higher (0.23 vs. 0.08 mm) than for the transitional case. For both cases there is a slow build-up in bubble height when approaching the incident shock wave. After passing the shock wave, the boundary layer undergoes transition and reattaches as a turbulent boundary layer. Notice also that the initial build-up in bubble height for the laminar case is observed to be nearly linear with streamwise distance.

Effect of shock strength

In addition to the nominal test condition case, a parametric investigation was conducted regarding the influence of shock strength, Mach number and Reynolds number. Here, the results on the shock strength are reported, obtained by varying the flow deflection angle between 1.0 and 5.0 degrees at Mach number of 1.7 (pressure ratio $p_3/p_1 = 1.11–1.64$). The corresponding reversed flow regions are presented in Fig. 52-left, where the length of the upstream portion, L_u, and the downstream portion, L_d, are defined by fitting straight lines to the experimental data points. For $\theta > 2°$

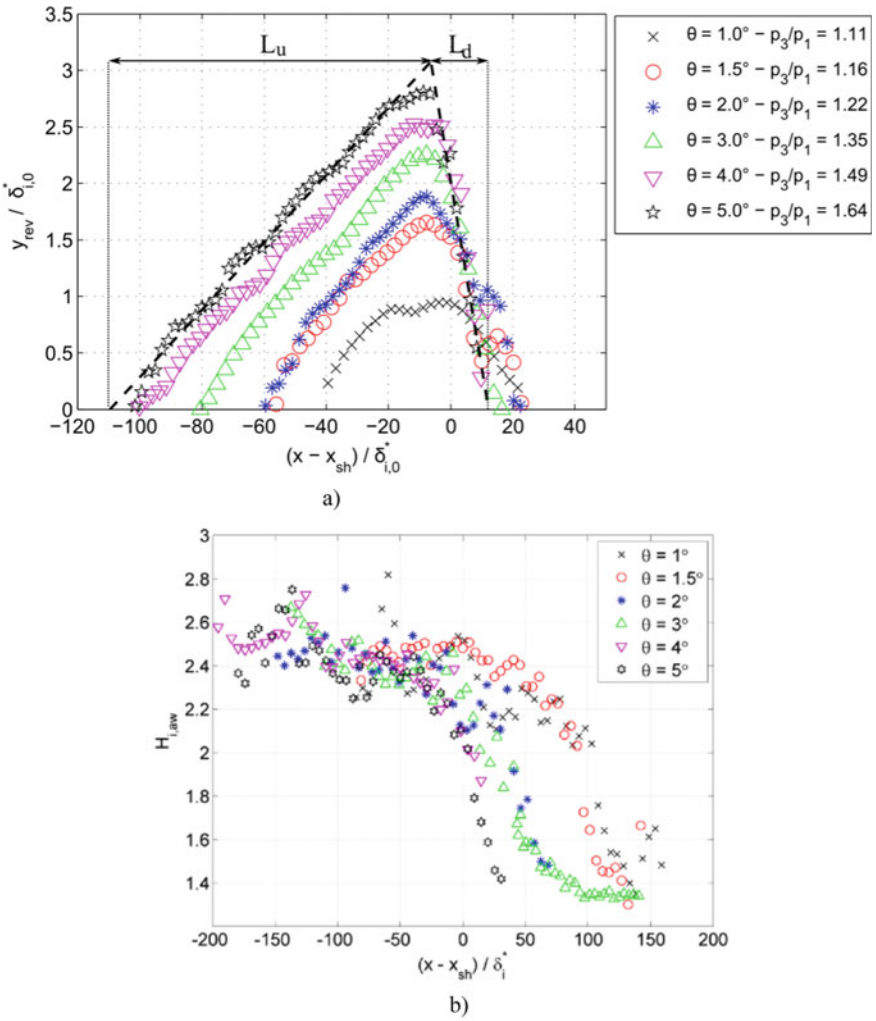

Fig. 52 The effect of shock generator angle on the reversed flow region size (left) and on the transition process (right); the latter is represented by the variation of the shape factor of the flow profile above the u = 0 isoline

($p_3/p_1 > 1.22$) the downstream portion of the separation bubble keeps a near-constant length of 20 $\delta^*_{i,0}$ (see also Fig. 53). The upstream portion of the separation bubble, L_u, on the other hand, shows a near-linear increases with the shock strength. For weak shock waves ($\theta < 2°$), however, these trends no longer apply and the upstream portion of the bubble is found to rapidly decrease in size with reducing shock strengths, while the downstream portion of the bubble increases in size. For shock strengths of $\theta = 1°$ – 1.3° ($p_3/p_1 = 1.11$–1.14) a near-symmetrical bubble is recorded, with comparable L_u and L_d.

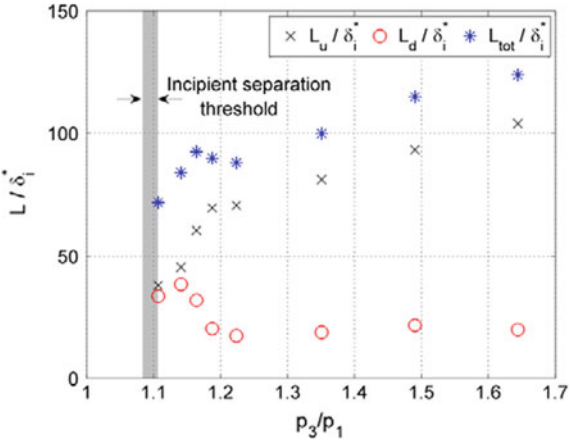

Fig. 53 The size of the reversed flow region as function of shock strength

The incipient separation threshold indicated in Fig. 53 is based on the free-interaction of Chapman [26].

The observed trends are strongly connected with the transition behaviour of the shear layer over the separated flow region, as supported by further investigation of the velocity profiles. This analysis (see Fig. 52-right) indicates that the transition location (where the incompressible shape factor decreases) is found to move upstream, yet even for the strongest shock wave ($\theta = 5°$) transition always occurs downstream of the shock impingement location. So, the boundary layer stays in a laminar state over the upstream part of the separation bubble. On the other hand, transition occurs significantly further downstream for weak shocks, corresponding to $\theta < 2°$. The data implies that for shock angles in the range of 1–1.5° the boundary layer remains in a close to laminar state throughout the entire interaction, which explains the longer downstream portion of the separation bubble.

Oblique shock wave reflection under turbulent conditions

Two approaches were followed to establish the presence of a fully turbulent boundary layer entering the interaction (referred to as case 1 and case 2, respectively):

- The boundary layer was tripped 5 mm from the leading edge with a 0.2 mm thick zig-zag strip. The incident shock wave is positioned 71 mm from the leading edge.
- The incident shock wave is positioned 30 mm downstream of the approximate natural transition location, so at x = 101 mm. At this location, the flow has left the intermittent transitional regime and a fully turbulent velocity profile is established.

As evidenced by the velocity profiles shown in Fig. 54, good agreement with the log law theory is found for both cases (with $H_i = 1.37$ and 1.32 for case 1 and 2, respectively).

In view of the similarity of the incoming boundary layer profiles for case 1 and 2, comparable flow fields are expected to occur throughout the interaction for both cases. This is confirmed by Fig. 55, from which it is clear that the impinging shock wave results in a thickening of the boundary layer.

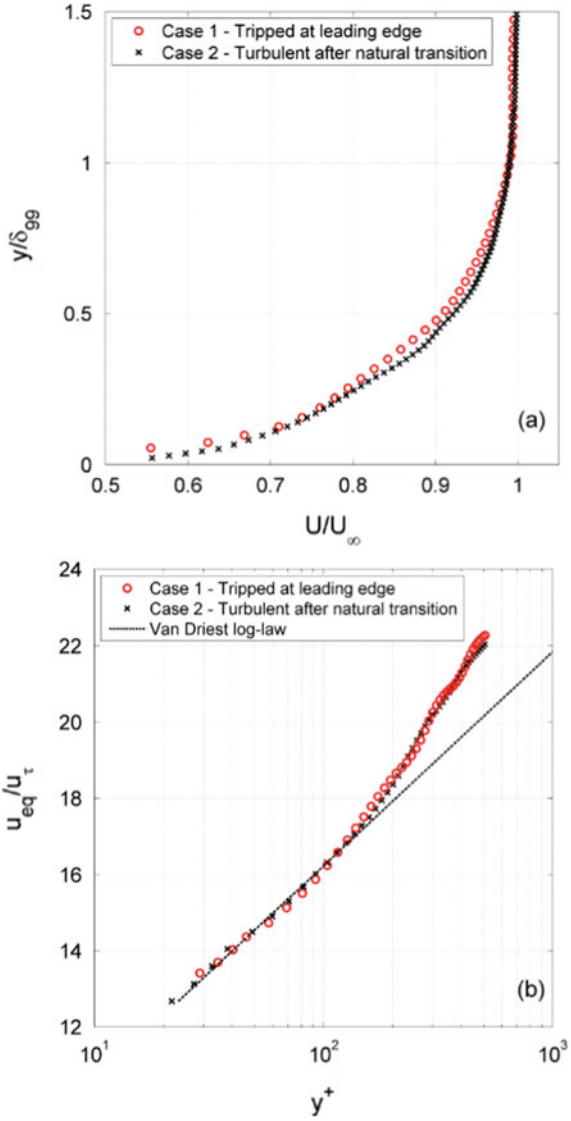

Fig. 54 Comparison between the velocity profiles measured 6 mm upstream of the interaction for case 1 and 2, in outer variables (**a**) inner variables (**b**)

This is even more evident when considering the development of the integral boundary layer parameters in Fig. 56. For case 2, the displacement thickness starts to increase approximately 2δ upstream of the incident shock and reaches its maximum value in close vicinity of the impingement point of the incident shock. Case 1 shows the same general trend, but the change occurs more gradual, with the displacement thickness already showing an increase 3δ upstream of the incident shock

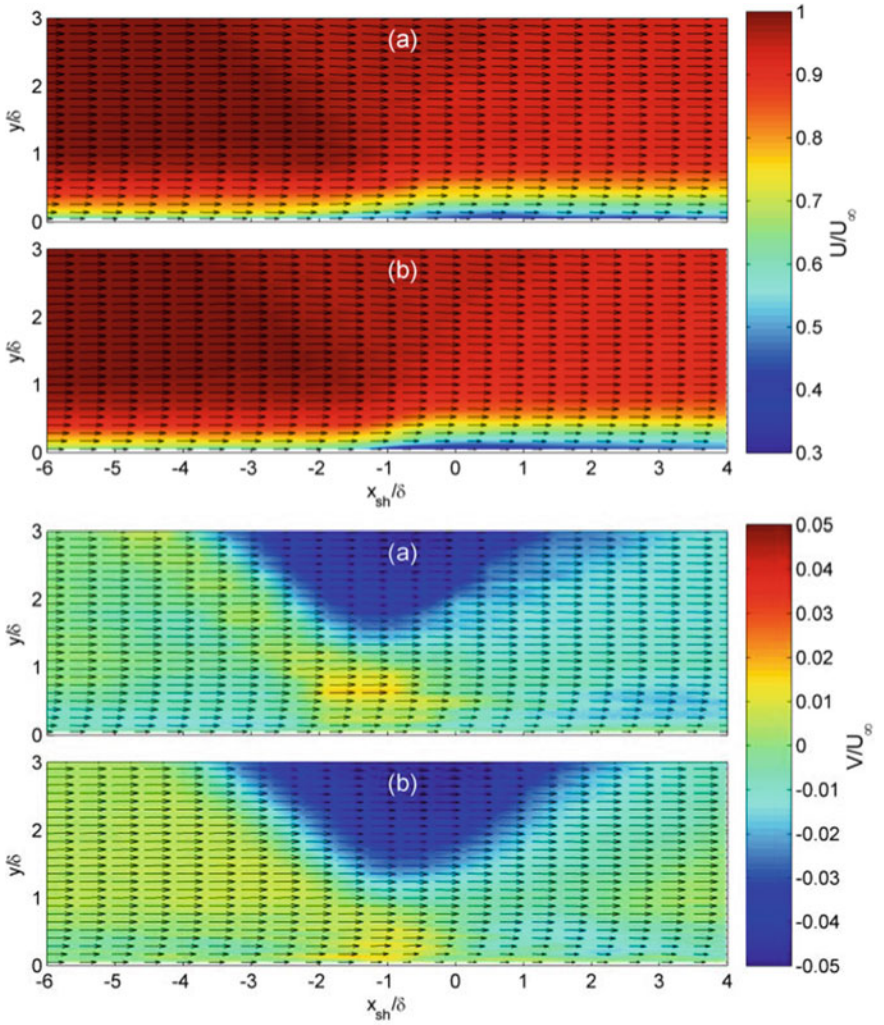

Fig. 55 The velocity components of the velocity field inside the interaction region. For case 1 (**a**) and case 2 (**b**)

wave. Downstream of the incident shock, the boundary layer recovers and the displacement thickness is again reduced, this in contrast to the momentum thickness, which remains relatively constant downstream of the incident shock.

The development of the shape factor shows a trend very similar to the one described for the displacement thickness, with the highest shape factors (1.6–1.65) being reached around the impingement point of the incident shock.

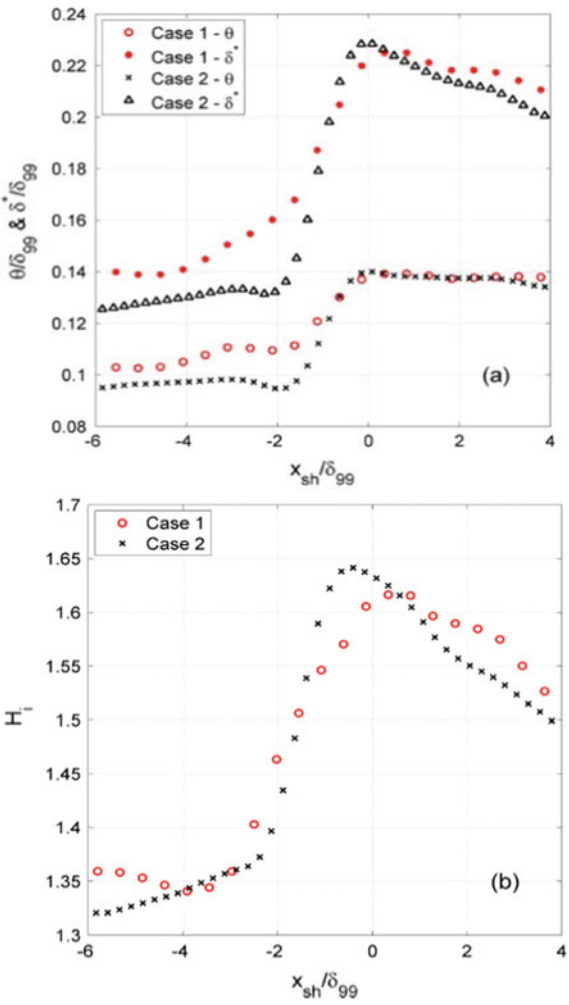

Fig. 56 Variation of the integral boundary layer properties through the interaction region: (**a**) incompressible momentum thickness θ_i and displacement thickness δ_i^* and (**b**) the incompressible shape factor $H_{i\neg}$ (**b**)

2.2.4 ITAM

Laminar test case

Parameters of experiments carried out at natural laminar-turbulent transition are shown in Table 10. From the table it can be seen that the Mach number upstream of SWBLI (calculated on the basis of PIV data) is less than one measured upstream of the model (M = 1.47). This can be explained by a decrease of Mach number in a weak compression wave generated by the leading edge of the plate, which crosses the flow several times due to its reflections from the walls. The value of X_{imp} corresponds to the point of intersection of the incident shock wave with plate for inviscid flow, measured from the leading edge of the plate.

Table 10 Parameters of experiments

M	P_0, bar	T_0, K	Re_1, 10^6 1/m	X_{imp}, mm	β,°	Re_{Ximp}, 10^3	δ*, mm	State of BL
1.42	0.694	286.4	10.9	288	3,4	3145	0.53	Turb.
1.42	0.847	280.8	13.7	290	3,4	3975	0.43	Turb.
1.42	0.984	284.2	15.6	290	3,4	4540	0.46	Turb.
1.43	0.551	291	8.5	132	3,4	1120	0.30	Lam.
1.43	0.694	290.4	10.7	133	1,2, 3,4	1425	0.27	Lam.
1.43	0.834	286.3	13.2	134	3,4	1755	0.25	Lam.
1.43	0.978	285.1	15.5	134	1,2, 3,4°	2070	0.22	Lam.

Fig. 57 Schlieren visualization

Example of the results illustrating the wedge angle effect on the interaction study are shown in Fig. 57 as instantaneous (exposure 1.5 μs) and the averaged schlieren images obtained for the laminar case. Origination of vortices in the zone of SWBLI can be clearly seen and indicates the laminar-turbulent transition. The adverse pressure gradient caused earlier turbulization of boundary layer. For a horizontal orientation of the knife in the averaged images the laminar boundary layer is observed as narrow bright line. Therefore we can qualitatively assume that the end of the bright line corresponds to the point of the boundary layer turbulization.

With the reduction of the wedge angle the size of the separation zone is reduced and the location of the laminar-turbulent transition is shifted downstream (Fig. 58). Apparently decrease of the pressure gradient in the shock wave results in weakening of disturbance growth in the interaction zone. Increasing of the Reynolds number from 10.7 up to $15.5 \cdot 10^6$ m^{-1} significantly reduces the size of the separation region, but has little effect on the position of the laminar-turbulence transition.

Figure 59 shows PIV velocity fields obtained for the same flow parameters. PIV measurements were performed in the region of the interaction at the centreline of the model. All the figures clearly show the formation of a weak shock wave arising at the beginning of the separation zone. The intensity of the separation shock is small

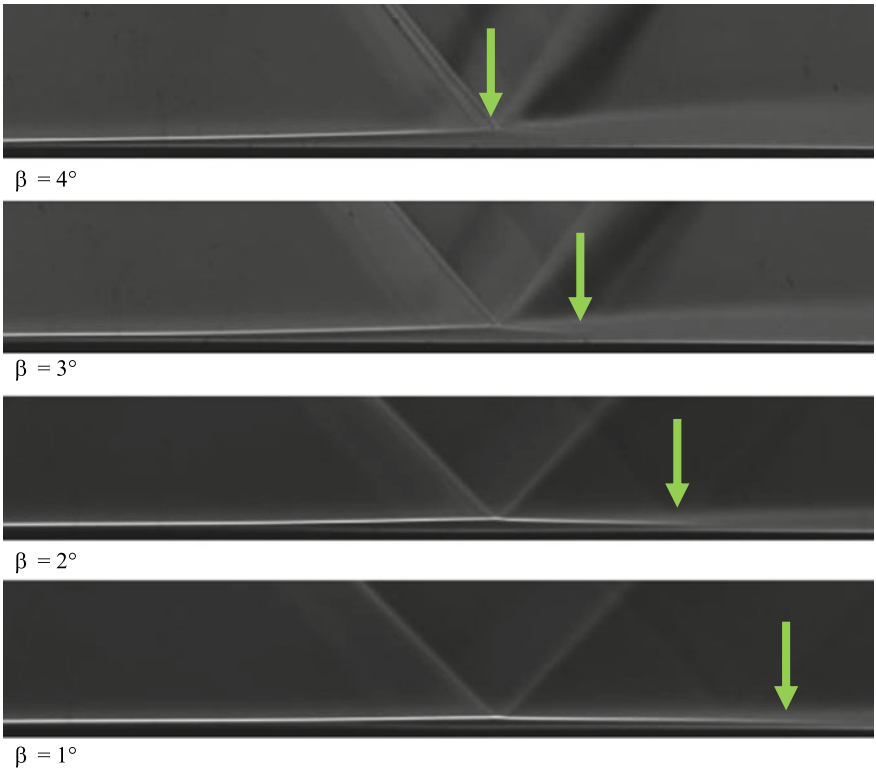

Fig. 58 Laminar case (L = 250 mm, Re_1 = 10.7e6 1/m)

due to a slight growth in the displacement thickness in the separation zone. There is only one separation shock wave on the velocity distribution, since the displacement thickness in the laminar separation increases approximately linearly. It can be seen that reduction of the incident shock wave angle just slightly changes the intensity (angle) of the separation shock. It means that the angle of the flow displacement by the separation weakly depends on the strength of the shock wave.

Let's consider a change of the separation zone length (length of interaction zone). If the wedge angle decreases from 4 to 3° the length of the separation zone remains almost constant. The figure clearly shows that decrease of the wedge angle is accompanied by a downstream shift of the separation beginning for about 10 mm, but the end of the separation is also shifted by the same distance. This is the result of the displacement of X_{imp} downstream due to changing of wedge angle β.

With further decrease of the incident shock wave strength, the length of the separation zone begins to decrease more significantly. This behavior is well explained by the turbulization of the boundary layer in the SWBLI zone. Laminar-turbulent transition in the interaction region leads to significant reduction of its length compared to the classical laminar case. Thus for the case of 4° the RMS velocity distribution

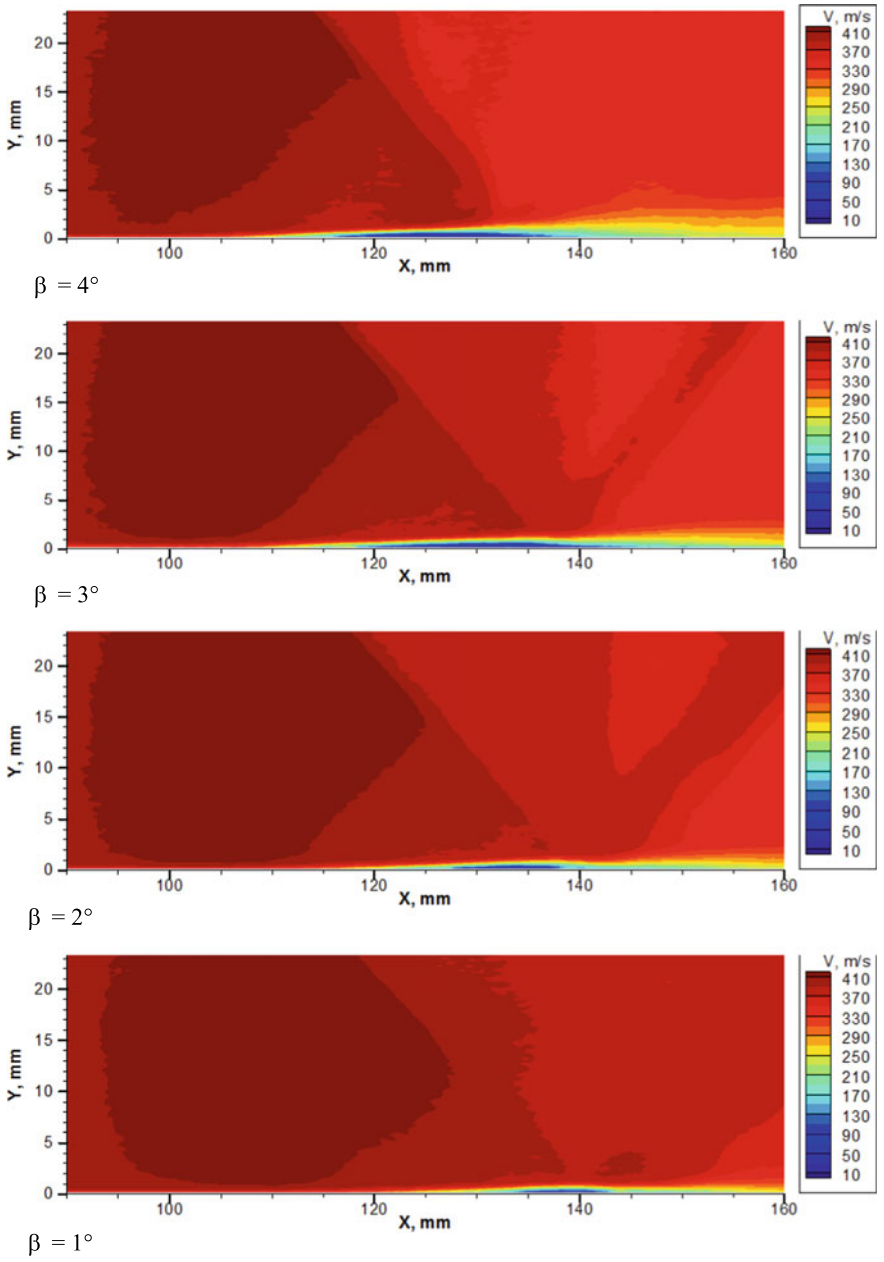

Fig. 59 Velocity field (Laminar case, L = 250 mm, Re_1 = 10.7e6 1/m)

shows that the transition occurs near the point of intersection of the incident shock wave with the model. The decrease in the strength of the incident shock wave is accompanied by a shift of the transition point downstream, which is clearly seen from the substantial decrease in the thickness of the wake boundary layer for $\beta = 1{,}2°$. As a result the laminar-turbulent transition process gradually diminishes its effect on the length of the SWBLI. Therefore the significant decrease of the wedge angle from 4 to 1° changes the size of the interaction zone only by a factor of ≈2. Figure 60 shows the distribution of the displacement thickness and the shape factor in the zone of SWBLI at $\beta = 4°$. The solid lines correspond to the data obtained in the zone of interaction, the dotted lines correspond to another experiment where the measurements in the wake were performed. It is clearly seen that the data obtained for the same flow conditions are perfectly matched. Integral parameters (momentum thickness, shape factor) vary only slightly. The sharp decrease of the shape factor at X_{imp} indicates the turbulization of the boundary layer, but its value indicates that the equilibrium state is not reached.

The spectra of wall pressure pulsations confirm this assumption. For laminar case at $\beta = 3, 4°$ peak of wall pressure pulsation was found near X_{imp} and it is most likely associated with the beginning of the turbulization of BL (see Fig. 61). The growth of pulsations in the wake mainly takes place only in some frequency band. This means that the turbulent boundary layer is not equilibrium. The characteristic peak of pulsations in the high-frequency range for the laminar case has a frequency 20–30 kHz which is substantially smaller than the characteristic frequency of the turbulent boundary layer. It can be attributed by the generation of a large-scale structures for the laminar case.

In the low-frequency region two peaks at 2 and 0.2 kHz were found. These pulsations are most probably the characteristic ones of the separation zone and the zone of interaction. From the correlation analysis it was discovered that these disturbances (up to 2 kHz) propagate upstream and originate near the point of the shock wave interaction with the boundary layer.

Figure 61b shows that the decrease of the total pressure was accompanied by a drop of the pulsations in the low-frequency region < 10 kHz. It van be concluded that there is an influence of the Reynolds number on the development of perturbations in the separation zone.

Turbulent Test Case

For Mach number M = 1.43 – 1.47 and turbulent state of the incoming boundary layer the adverse pressure gradient in the shock is insufficient for the flow separation. For the case of strong incident shock wave ($\beta = 4°$) and fully turbulent interaction it is possible to see the formation of small Mach stem (Fig. 62). Mach stem is generated here due to presence of strong reflected shock wave and leads to considerable increase of the local adverse pressure gradient. It is interesting to note that the cause of the formation of the strong reflected shock is higher resistance of the turbulent boundary layer to the separation. As a result the length of separation bubble is relatively small

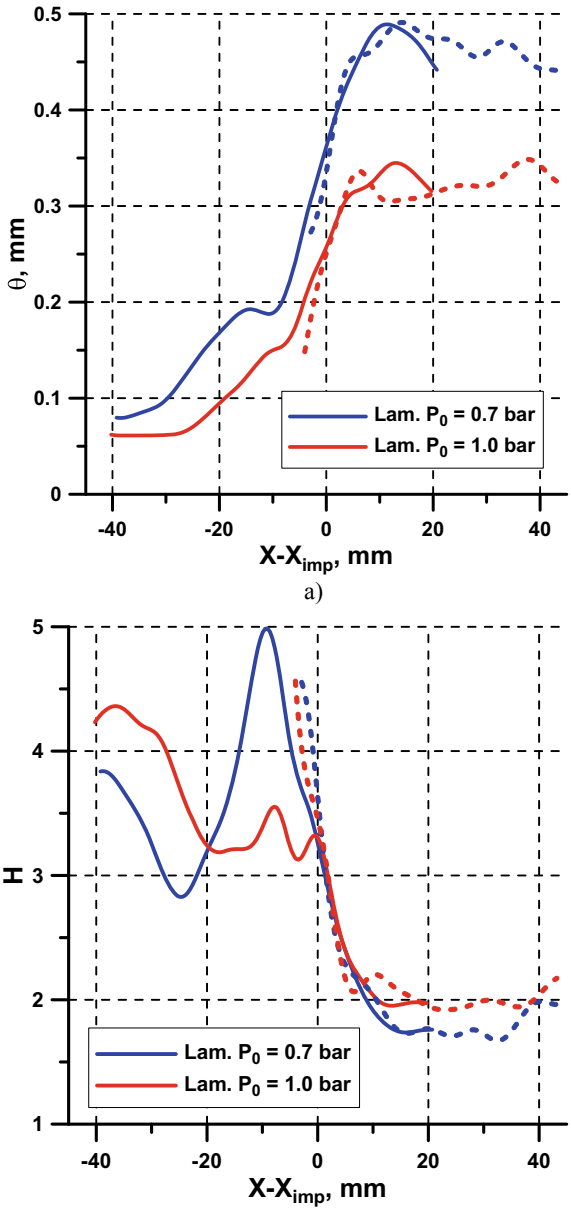

Fig. 60 **a** The momentum thickness and **b** shape factor distribution along the SWBLI

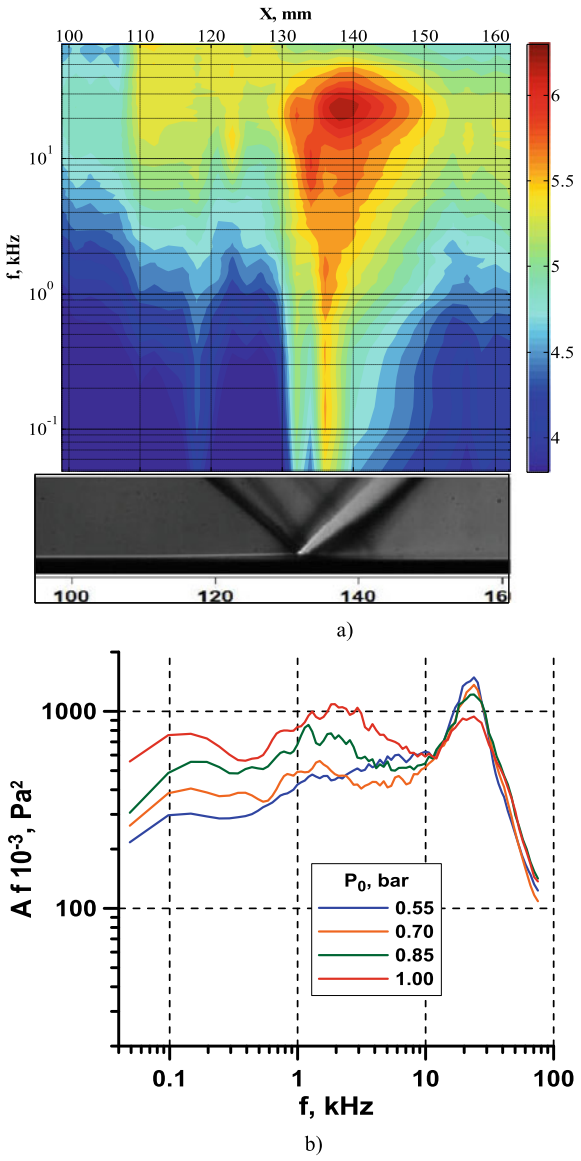

Fig. 61 *PSD·f* of wall pressure pulsations for laminar test case **a** along zone of SWBLI for $P_0 =$ 0.7 bar and **b** at the point of maximum pulsation for various P_0

comparing to the laminar case and therefore there is very rapid growth of the boundary layer displacement thickness in the zone of SWBLI. This leads to the formation of a strong reflected shock wave. But if the wedge angle changes from 4 to 3° the Mach stem almost disappears. Note that the thickness of the boundary layer in the wake obtained for the turbulent case is close to the laminar one founded at $\beta = 4°$.

Example of RMS value of streamwise velocity pulsations is presented in Fig. 63. The level of pulsations upstream of the incident shock corresponds to a turbulent flow.

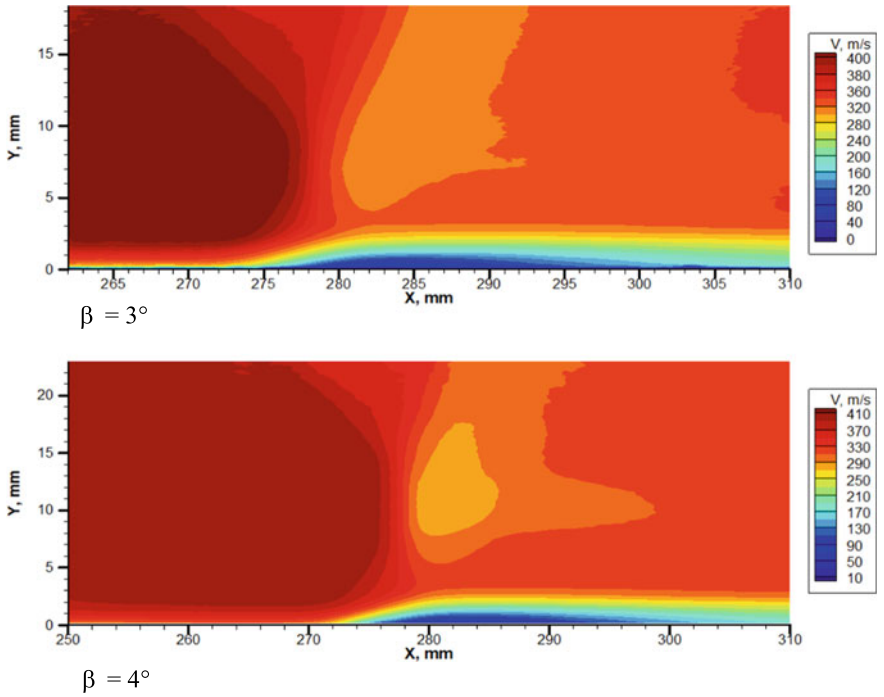

Fig. 62 Velocity magnitude at the centerline, L = 100 mm, natural turbulization $P_0 = 0.7$ bar

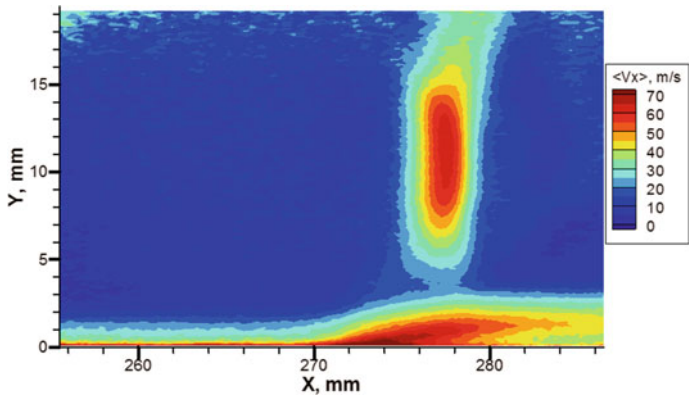

Fig. 63 RMS of streamwise velocity pulsations, L = 100 mm, natural turbulization

The streamwise distribution of pulsations in the zone of interaction corresponds to the published data. Pulsations in the zone of the Mach stem are result of low-frequency oscillations of the interaction zone.

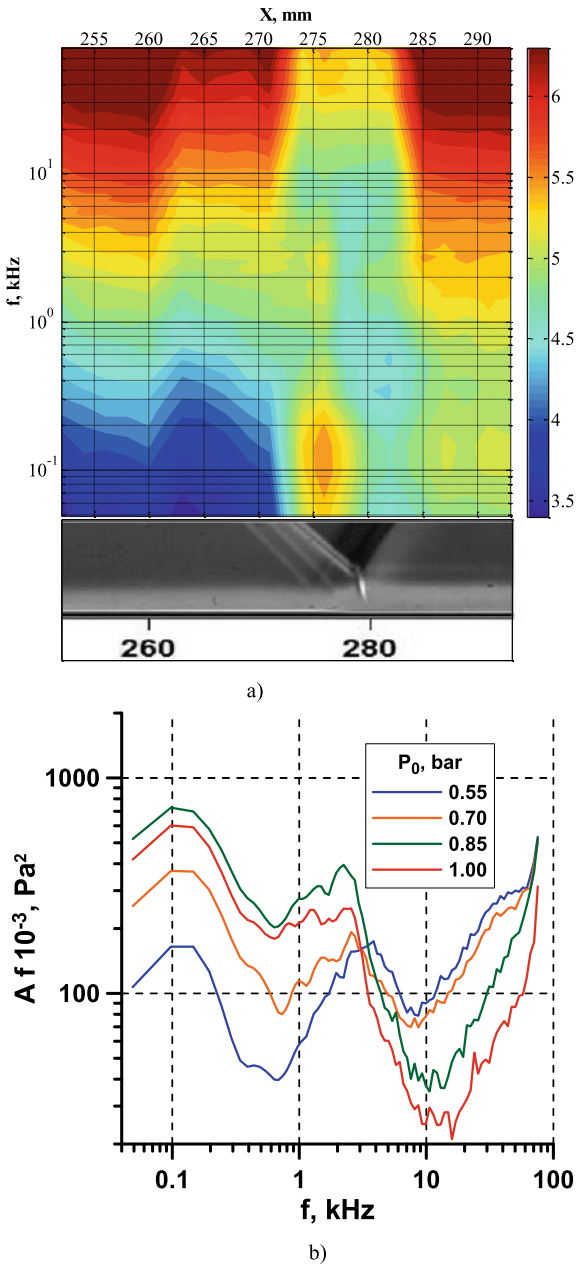

Fig. 64 *PSD·f* of wall pressure pulsations for turbulent test case **a** along zone of SWBLI (L = 100 mm, β = 4°, P_0 = 0.7 bar) and **b** at point of maximum pulsation for various P_0

An example of the wall pressure pulsations spectra distribution along SWBLI zone for the turbulent case is shown in Fig. 64. The data show that the level of pulsations upstream of the incident shock corresponds to a turbulent flow. The spectra in the

wake are also turbulent. Near the reflected shock wave the low-frequency pulsations are generated which have been well studied in UFAST.

In view of data obtained for the laminar case it is possible to assume that the incoming pulsations significantly influence on the process of perturbations development in the zone of adverse pressure and their evolution in the wake.

Using the RMS values of U pulsations the following value can be calculated:

$$\int \rho u^2 \, dy \tag{14}$$

Figure 65b. The integral is calculated along the vertical coordinate up to the undisturbed inviscid flow. This value will be analyzed coupled with momentum thickness distribution along the zone of interaction (Fig. 65a).

For the turbulent inflow boundary layer the peak of pulsations was found at the beginning of the SWBLI zone near the reflected shock wave. Near this location there is the rapid increase of momentum thickness and corresponding loss of total pressure. It is obvious that the growth of pulsations is a result of convective processes and energy transfer in the shear layer which leads to increase of drag.

Growth of the pulsations for the transitional case is more gradual and accompanied by weaker growth of momentum thickness. For the laminar case the most dramatic growth of pulsations (more than in turbulent case) was obtained. It was accompanied by an increase of momentum thickness approximately up to the level of turbulent case. But for the laminar case the turbulent boundary layer in the wake is substantially more nonequilibrium as follows from the POD analysis and the spectra of pressure pulsations (Fig. 61).

It should be noted that due to low spatial resolution of the PIV method (for the selected scale), the momentum thickness for the laminar and transitional inflow boundary layer is overestimated. It can be concluded that for small supersonic Mach numbers and strong incident shock waves, the process of the laminar-turbulent transition has a very large effect on the mean and nonstationary parameters of the zone of SWBLI.

2.3 CFD of the Laminar and Turbulent Interaction

(IUSTI, ONERA, SOTON, IMFT)

2.3.1 IMFT

Introduction

The SWBLI of oblique shock is studied in comparison with the TUD experiments and in respect of the effect of fully turbulent boundary layer upstream and on the

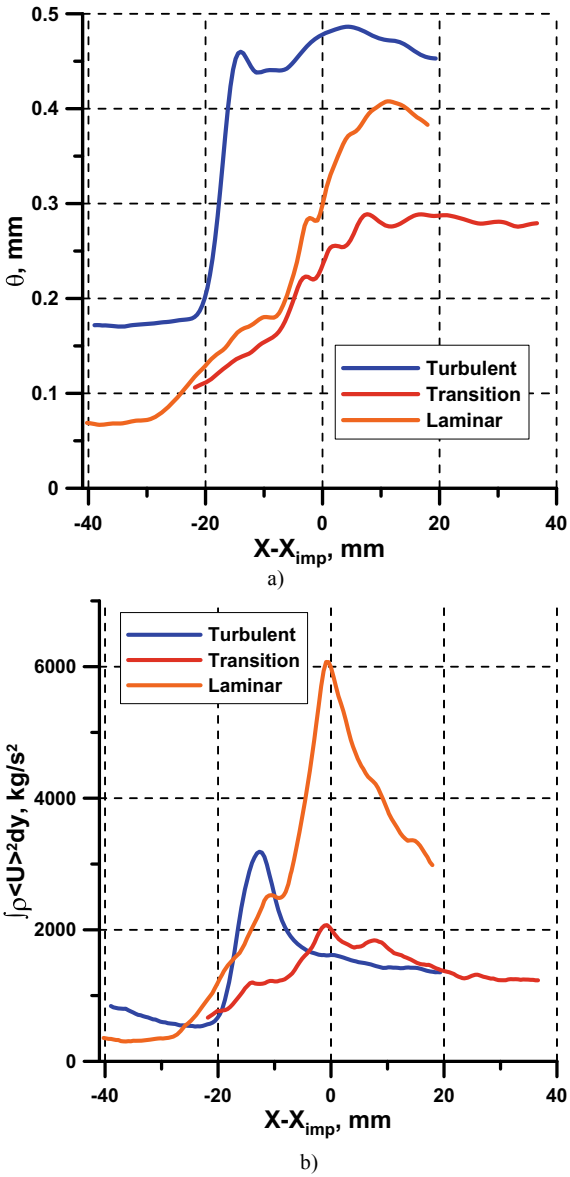

Fig. 65 **a** The momentum thickness distribution and **b** The integrated RMS of velocity pulsations along the SWBLI ($Re_1 = 13.2 \cdot 10^6$ m^{-1})

transition location by numerical tripping (turbulent viscosity value), by using the hybrid DDES—Delayed Detached Eddy simulation as well as the Organised Eddy Simulation approaches. These methods are also compared with the WM-LES (Wall-Model LES approach of Stanford, thanks to collaboration of IMFT with the group of Prof. P. Moin and our involvement in the CTR—Center of Turbulence Research programme of July-August 2014).

This study accounts on the efficiency of the DDES-OES in respect of other URANS approaches in capturing the SWBLI physics in comparison with the experimental data. To this end,

- integral quantities along the boundary layer and in the SWBLI are presented and compared with the TUD experiments
- grid sensitivity and influence of the upstream turbulence intensity
- skin-friction coefficient
- influence of fixed transition position at x/C = 33%.

The analysis of the shock wave-boundary layer interaction (SWBLI) is carried out in supersonic speeds regarding laminar wing technology of future aircraft design, in the context of the TFAST European project. Vision of H2020, whose objectives include the reduction of emissions and more effective transport systems, puts severe demands on aircraft velocity and weight. These facts require an increased load on wings and aero-engine components. The greening of air transport systems means a reduction of drag and losses, which can be obtained by keeping laminar boundary layers on external and internal airplane parts. Increased loads make supersonic flow velocities more prevalent and are inherently connected to the appearance of shock waves, which in turn may interact with a laminar boundary layer. Such an interaction can quickly cause flow separation, which is highly detrimental to aircraft performance and poses a threat to safety. In order to diminish the shock induced separation, the boundary layer transition upstream of the interaction should be optimized in respect of minimizing the skin-friction coefficient upstream and within the interaction.

Based on the natural flow developed, the laminar/turbulence transition can be imposed anywhere upstream of the SWBLI and the effects of various locations can be studied. In specific supersonic Mach number ranges, the boundary-layer structure within SWBLI can insipient separation accompanied by predominant unsteadiness and the influence of the transition location plays an important role for the design, concerning oblique shock interactions.

Simulations

Numerical method

The simulations have been performed with the Navier-Stokes Multi-Block (NSMB) solver. The NSMB solver is the fruit of a European consortium that included Airbus from the beginning of'90's, as well as main European aeronautics research Institutes, as KTH, EPFL, IMFT, ICUBE, CERFACS, Univ. of Karlsruhe, ETH- Zürich, among other. This consortium is coordinated by CFS Engineering in Lausanne, Switzerland. NSMB is a structured code including a variety of efficient high-order numerical schemes and turbulence modelling closures in the context of LES, URANS and RANS-LES hybrid turbulence modelling, especially DDES (Delayed Detached Eddy Simulation). NSMB highly evolved up to now and includes an ensemble of the most efficient CFD methods like URANS modelling for strongly detached flows, allowing for Detached Eddy Simulation for e.g. and the Delayed Detached Eddy Simulation

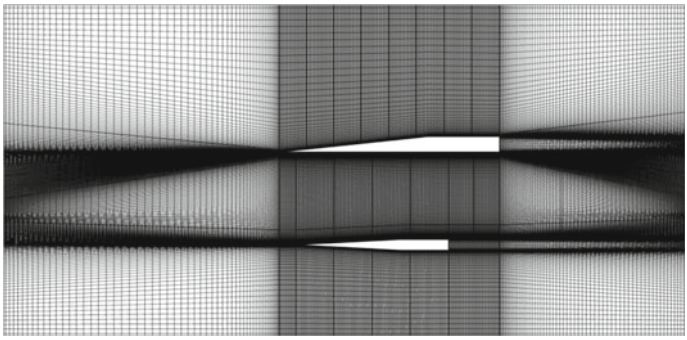

Fig. 66 Computational domain

(DDES), [30] as a hybrid method. NSMB solves the compressible Navier-Stokes equations using a finite volume formulation on Multi-Block structured grids.

In the two studies presented here, the time integration relies on a second-order backward Euler scheme based on the full matrix implicit LU-SGS (Lower-Upper Symmetric Gauss-Seidel) method and on the dual-time stepping, performing internal iterations, to reach convergence in each time step, which is 10^{-7} s.

Oblique Shock-Wave—Simulations Based on the TUD Configuration

The oblique shock wave test case has been studied in the conditions of the Delft experiment concerning the fully turbulent experimental case. The Reynolds number based on the flat plate length is ~4.08 million. The upstream isotropic turbulence intensity level is 0.56%.

For the 2D simulations, the structured mesh used has ~319000 cells. Due to convergence issues with two-equation models, this mesh has been refined around the trailing edge of the flat plate, giving a grid of ~25 M cells in 3D. The first grid has been extruded to a span length of 272 ~ mm, the span of the flat plate, giving a 3D mesh of ~31 million cells. The domain used for the computations is 1.5 height, 3.125 length (and 2.27 width in 3D) non-dimensioned by the length of the flat-plate (120 mm), and is also represented in Fig. 66.

The experimental conditions have been set up such that the effects of the upper and lower walls on the interaction region are limited. This helped the CFD calculations by placing the flat plate and the shock generator in free stream conditions, which define the external boundary conditions of domain. The geometrical elements are defined by adiabatic solid wall boundary conditions. Therefore, the inlet conditions are free-stream Dirichlet, where at the outlet boundary, characteristic velocity boundary conditions are considered. On the upper and lower boundaries, free-stream conditions are specified. In the spanwise direction, symmetry conditions have been used.

The AUSM spatial scheme has been first used but it displayed convergence insufficiencies. The Roe (1981) 3rd order scheme with van Leer (1978) MUSCL limiter has been used afterwards for all the computations. The diffusion terms have been discretized by means of central differencing. The time-step value was set after detailed tests to 0.5×10^{-7}.

Four turbulence models have been used for the 2D URANS computations: the one-equation Spalart-Allmaras [31], the k-ω—SST, Menter (1994) [32], the k-ε with Chien [33] low Reynolds number damping near the wall, as well as the k-ε-OES (Organised Eddy Simulation) model [34]. The use of the k-ω SST model displayed convergence issues on the coarse and finer grids. Therefore, the Spalart-Allmaras, the k-ε Chien and the k-ε-OES models have been finally used. The Spalart-Allmaras (SA) model has been used on the coarse grid. The k-ε-Chien (denoted hereafter as k- ε), as well as the k-ε-OES have been used on the finer grid. The results presented in this part will focus on these three models, by comparing the boundary-layer properties as well as the caption of the unsteadiness in the SWBLI.

Boundary-Layer Analysis

Figure 67 shows the integral parameters versus x in the boundary layer for the different turbulence models. The momentum thickness is over-predicted by the SA and k-ε models and underpredicted by the k-ε-OES, for which the displacement and momentum thicknesses are found closer to the experiments. The shape factor though is found in better agreement according to the two first models. The skin-friction coefficient displayed a decrease across the SWBLI region. Figure 68 shows the iso-pressure contours and probe—points for the spectral analysis.

Figure 69 shows the Power Spectral Density (PSD) at several selected positions. Point 1 is located in the beginning of the interaction. The models indicate formation of predominant frequency peaks around the frequency of order 5×10^4 Hz, being of the same order of magnitude as in experimental studies by Dupont, by means of TRPIV. In the following, the influence of a fixed transition position at 33 and 66% from the leading edge is studied by using the SA model (Fig. 70).

DDES and IDDES Simulations and Comparison with WM-LES

For a detailed view of this study, the reader can also refer to the edition of the Center for Turbulence Research—CTR, http://ctr.stanford.edu/publications.html.

WM-LES stands for Wall-Model-LES method of the group of Prof. Moin.

In Fig. 71, the mean stream-wise velocity profiles of the boundary-layer, around x_{sh}, are provided at eight different stream-wise locations and allow a more detailed comparison. The velocity profiles are normalized by the corresponding local free-stream velocities in the experiment at each location. In the DDES case, the mean stream-wise velocity is underestimated compared to the experiment, which can be understood as an overestimation of the development of the turbulence in the boundary

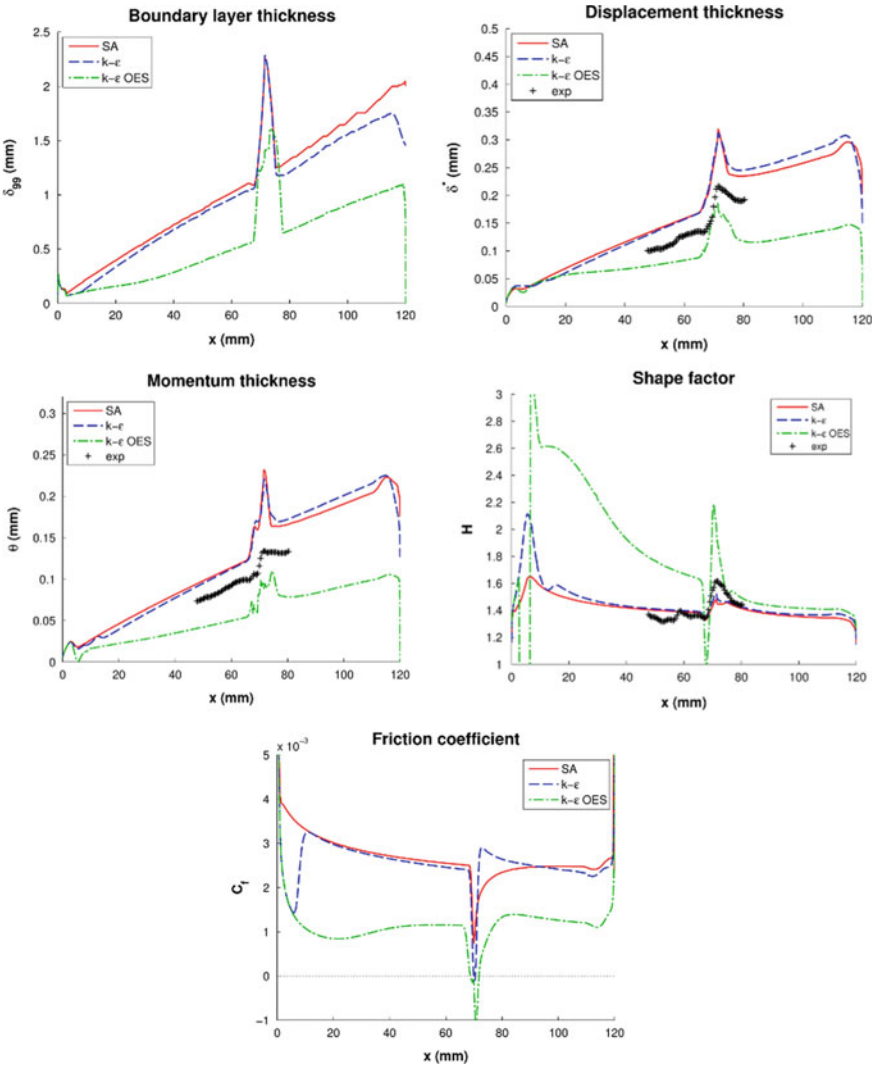

Fig. 67 Integral parameters in the boundary layer versus x in comparison with the TUD experiments

layer. The Spalart-Allmaras model induces a quasi-instantaneous laminar-turbulent transition from the leading edge in the RANS layer, while in the experiment, the transition is triggered in the zone of $x_{LE} = 5$—16 mm by the zig-zag tripping. The result of the transitional DDES matches better with the experiment by using the conditioning of the boundary layer, which delays its development to the turbulent state, until the flow approaches the interaction zone where the decrease in velocity observed in the experiment is underpredicted. WM-LES profiles matches well with the experiment, especially in the upstream and downstream directions of the SWBLI

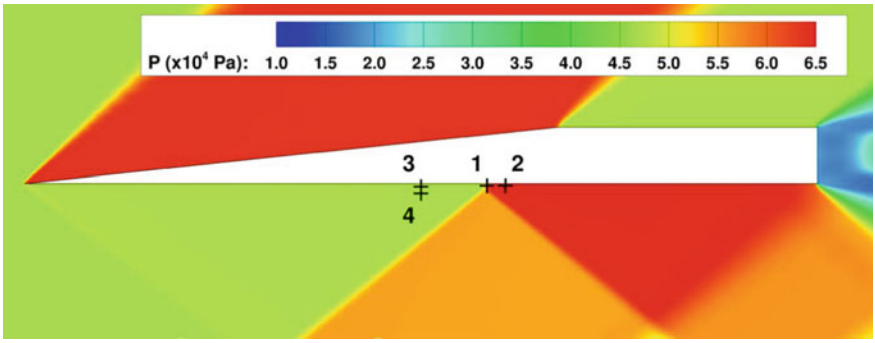

Fig. 68 Iso-pressure coefficients and probe (monitor) points locations

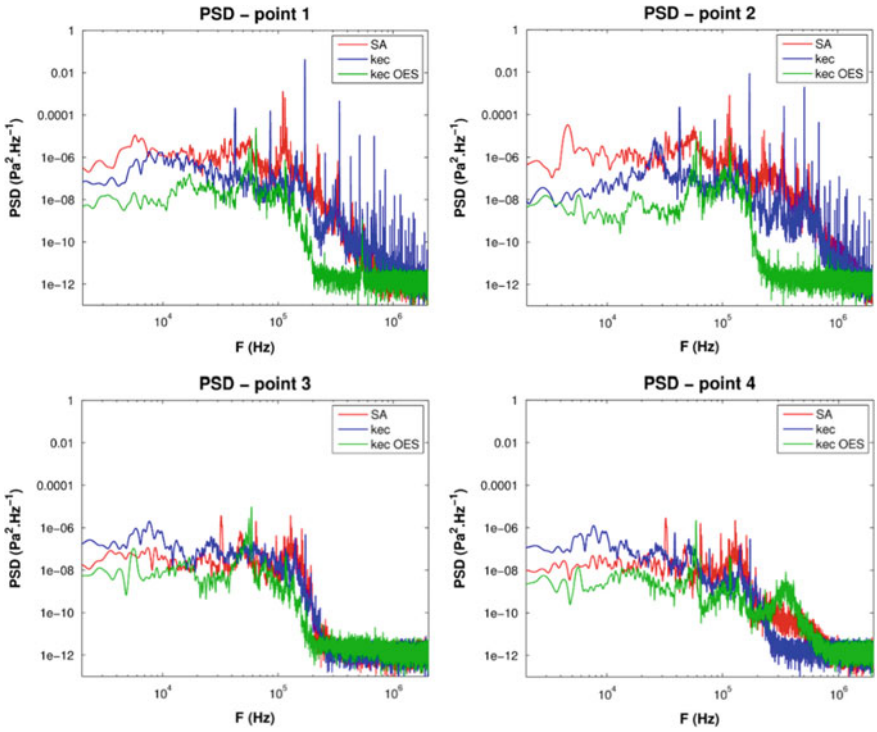

Fig. 69 Power Spectral Density PSD at selected monitor points as I, Fig. 68

zone. In the interaction zone ($x\text{-}x_{sh}$) = 0.1 and 4.8 mm), however, there are noticeable discrepancies from the experiment, similar to the transitional DDES. Since an equilibrium WM-LES formulation is used in this study, non-equilibrium effects such as strong pressure gradient and flow recirculation cannot be achieved in the wall model. Dawson [35] also observed poor predictions through interaction in their study of a

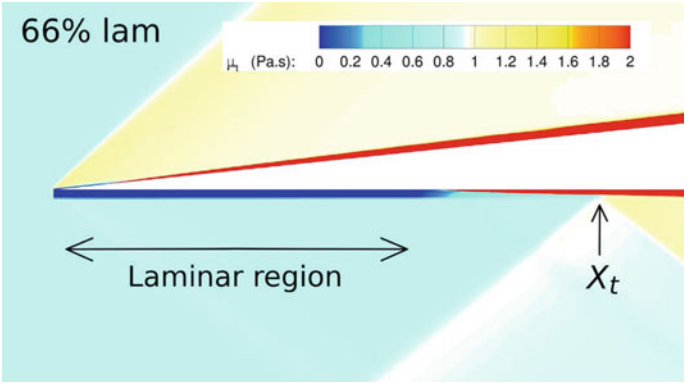

Fig. 70 Eddy-viscosity iso-contours illustrating the laminar-to-turbulent transition regions for a fixed transition position at 66%

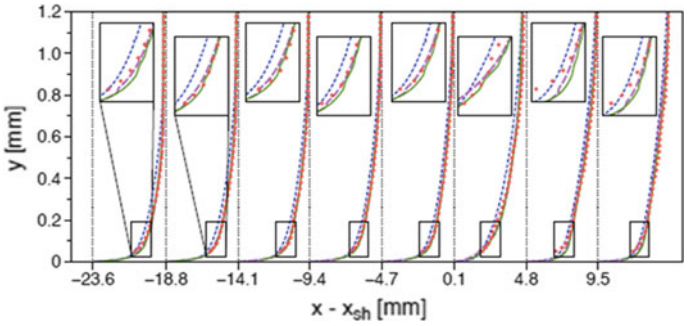

Fig. 71 Velocity profiles at 8 streamwise locations: normalized bu the experimental U∞ at each location. Blue line; DDES, violet line DDES with fixed transition at 33%. Green line: comparison with WM-LES commputations by the group of Prof. Moin, CTR 2014, Stanford. Dots: TUD experiment

supersonic compression ramp using a WM-LES. By investigating the magnitude of each term in a wall-resolved LES in the same configurations, they concluded that the convective and pressure gradient terms are dominant in near interaction zone. However, previous attempts to include dominant terms measured at the matching location (h_{wm}) in the equilibirum formulation such as that by Hickel [36] not only had difficulties in showing a satisfactory result but also suffered from numerical stability problems. As the flow goes downstream of the interaction and recovers equilibrium behavior, the WM-LES profiles is getting close to the experiment. Therefore, it may be necessary to solve the full non-equilibrium equations in the wall model. However, the accuracy of the PIV measurements in the SBLI region is reduced compared to that of the other regions of the boundary layer.

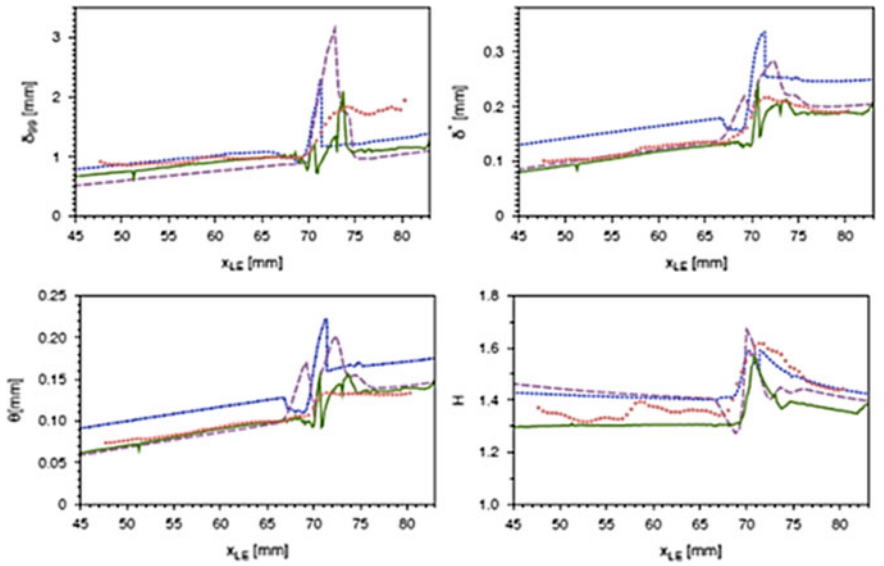

Fig. 72 Boundary layer thickness δ_{99} and displacement thickness δ^* (top). Momentum thickness, bottom. Line symbols as in previous figure

Figure 72 shows the distributions of boundary-layer thickness (δ_{99}), displacement thickness, momentum thickness and shape factor H, as a function of x_{LE}.

For δ_{99}, DDES and WM-LES match relatively well with the upstream of the SBLI, given the fact that in general 99 cannot be accurately defined for such complex flows. For and, however, the DDES slightly overestimates the integral values, which confirms the remarks of the previous paragraph: without any conditioning, the DDES generates an early development of the turbulent boundary layer compared to the experiment. This can be corrected by imposing the transition at $x_{LE} = 23$ mm, as explained above. In this case, the development of the boundary layer is delayed, as shown in all the graphs and the integral values downstream of the transition location get closer to the WM-LES and the experiment. In the interaction zone, none of the numerical methods can predict accurately the quantities.

In the downstream of the interaction, the WM-LES approaches the experimental values as well as the transitional DDES, as observed in Fig. 71. For the shape factor (H), both the transitional DDES and the WM-LES are reasonably close to the experimental value in $x_{LE} < xsh$. In the interaction zone, the transitional DDES and the WM-LES follows the general trend of the experiment but shows noticeable discrepancies from the experiment. In the downstream of the interaction zone, the transitional DDES shows a better agreement with the experiment. Interestingly, the DDES results are closer to the experiment for $x_{LE} \geq x_{sh}$ than for the other two calculations despite its poor predictions of the upstream flow for the other quantities

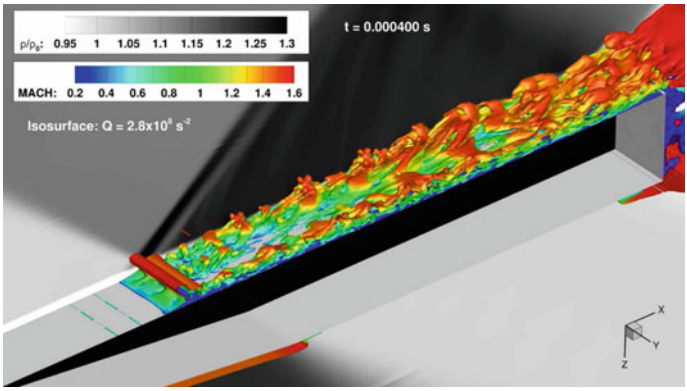

Fig. 73 Iso-Q criterion surfaces coloured by the Mach number showing the dynamics of the 3D vortex structures in the SWBLI and downstream, showing formation of 'hair-pin'vortices (grid of 13,5 M cells)

without conditioning. We briefly recall that the PIV measurements are less accurate in the SBLI region thanin the other regions of the boundary layer.

Figure 73 shows view of the 3D vortex structure dynamics in the SWBLI region and downstream of it, by illustrating formation of 'hair-pin' vortices, by means of Improved DDES (IDDES), Spalart [37] computations involving a specific wall model embedded LES in the near region. This model enhanced the turbulence intensity in all the flow field and produced higher amplitudes of *rms* than the experiments and the DDES results. These simulations allowed showing the 3D vortex structure within the interaction and past of it.

Conclusions

The present study analysed the SWBLI effect on the boundary layer subjected to supersonic (oblique shock) inlet Mach number conditions. A comparison of DDES and OES methods has been presented as well as in respect to experimental results is carried out concerning the supersonic interaction. A fair comparison with the TUD results is obtained. Comparison of DDES and of the WM-LES (Park, Moin, 2014), are used to predict the SWBLI in a Mach 1.7 flow. The flow is tripped very close to the leading edge in the experiment to insure a turbulent interaction, and both numerical approaches use different techniques to simulate the tripped fully turbulent boundary layer. While the results of the DDES modeling show an overestimation of the integral values of the boundary layer, the DDES with fixed transition at 33% and the WM-LES match well with the boundary-layer characteristics found in the experiment for the supersonic equilibrium flows. The results of standard DDES show an overestimation of the development of the boundary layer compared to the reference results. By using a preconditioning of the upstream boundary layer in an analogy with the WM-LES that used blowing and suction for the tripping in the experiment, a quite good behaviour is achieved.

Within the SWBLI region, strong pressure gradient and complex flow features near the wall at the interaction cannot be represented in the numerical methods. The

WM-LES needs to incorporate non-equilibirum dynamics for strong non-equilibrium regions. A possible future approach is the non-equilibirum WM-LES formulation suggestedby Park & Moin (2014), which uses a full non-equilibrium formulation to calculate the transient wall shear stress and heat flux q_w. However, even the full non-equilibrium WM-LES formulation cannot guarantees a more exact prediction in some strongly separated flows. The DDES approach is quite promising to provide the most close results within the region of SWBLI by using more economic grids, a crucial issue for the industrial involvement in the TFAST project. The tripping at transition location of 33% of (x-xsl) provides also quite close results in the region upstream of the SWBLI. The blending of OES in the RANS part of the DDES approaches is recommendable also to capture the unsteadiness in the SWBLI.

Acknowledgements
The investigations presented in this section have been obtained within the European research project TFAST (Transition location effect on shock wave induced separation), coordinated by P. Doerffer, IMP-PAN, Gdansk Academy of Science, Poland. The computing CPU allocation of IMFT has been attributed by the French supercomputing Centres CINES in Montpellier), IDRIS (Paris) and CALMIP (Toulouse). The authors are grateful to Professor Moin for the invitation in the CTR—2014 of D. Szubert and M. Braza.

2.3.2 IUSTI

Numerical method

The shock-wave boundary layer interactions into consideration are both transitional and possibly prone to low-frequency unsteadiness. Direct Numerical Simulation is the modeling of choice when dealing with transitional flow. However the occurrence of low– to medium–frequency unsteadiness makes the computation of several dozen of periods of the lowest-frequency phenomenon mandatory in order to achieve statistical convergence. The computation cost of DNS appears consequently to be very high, preventing parametric study involving several computations to be carried out.

In that context, Large–Eddy Simulation was demonstrated to be an interesting modeling compromise between computation accuracy and statistical convergence when dealing with turbulent interactions (see [38, 39], among others). It is however well known that Large–Eddy Simulations are rather ill–suited to describe transition to turbulence in wall–bounded flow [40], with significant modification of the transition location when the grid is refined, unless to go up to quasi-DNS resolution. However it may be noted that mixing layer instabilities are less prone to such mispredictions than boundary layers instabilities because of their far higher amplification rates.

The strategy developed is to perform computations for various grid resolutions while adjusting the amplitude of some inflow perturbations in such a way that a similar separation length is achieved from one computation to another. The rationale behind this is that, for a given Reynolds number of the incoming boundary layer, the length of separation is mostly imposed by the location of the transition within

the mixing layer developing over the bubble. The location of the transition is in turn governed by the non-linear saturation of the instable modes. Consequently, keeping constant the separation length should help ensuring that the transition process is not significantly altered when changing the grid resolution.

The various computations described hereafter are performed using ONERA's FLU3M solver that has been extensively used in the recent years to analyze successfully compressible flows either by LES and DNS [41, 42]. The numerical scheme is designed to be able to capture the shock while meeting the LES requirement of very low dissipation in the turbulent regions [43]. This is achieved by adding the dissipative part of the Roe scheme [44], modulated by Ducros' sensor [45], to a second order centered scheme. The subgrid filtering is implicitly provided by the mesh and the subgrid modeling relies on the selective mixed-scale subgrid model, well suited for compressible wall bounded flows [46].

Time integration is achieved by means of a second-order accurate implicit Gear scheme [47]. The timesteps of the various simulations have been selected in order to achieve maximum CFL numbers lower that 11, making the implicit time filtering negligible with respect to the implicit grid filtering. The resulting non-linear system is solved iteratively at every timestep with 7 sub-iterations.

Flow parameters selection and mesh design

Because of the difficulties encountered initially for the experiments, computations have been performed without knowledge of the definitive experimental setup. No measurements of the incoming boundary layer were therefore available to help setting the various parameters of the LES when the present numerical study has started. Consequently the incoming boundary layer has been assumed to match a Blasius profile for a Mach number equal to 1.63 and a stagnation temperature and a stagnation pressure equal respectively equal to $T_0 = 293.15\ K$ and $P_0 = 0.4\ atm = 50650\ Pa$. The boundary layer thickness at the inflow of the computational domain has then been evaluated by considering both the developing length and the location of the incident shock deriving from the initial experimental setup, resulting in Reynolds number equal to 1,400,000. A reference mesh with 26 M cells has been designed based on these information.

It has been used to perform parametric studies of the influence on the interaction region of either the shock angle or the inflow perturbation level. Inflow fluctuations are generated using a Synthetic Eddy Method with amplitudes one to two orders of magnitude lower than the ones retained for fully turbulent flows. Values of U_{rms} respectively equal to 0.125, 0.25, 0.5 and 1.0% of U_∞ have been tested for a shock generated by a 4.5° deviation of the flow, yielding interaction ranging from transitional separation bubbles to fully turbulent, attached interactions. Intermediate values of 0.25 and 0.5%, corresponding respectively to locations of the transition in the first half of the separation bubble and slightly upstream of attached interaction region, have been retained for the analysis of the influence of the shock strength. Three deviation angles ranging from 3.5° to 4.5° have been tested. Similar trends have been found for each angle, as seen in Fig. 74. Eventually, the 4.5° deviation angle has been

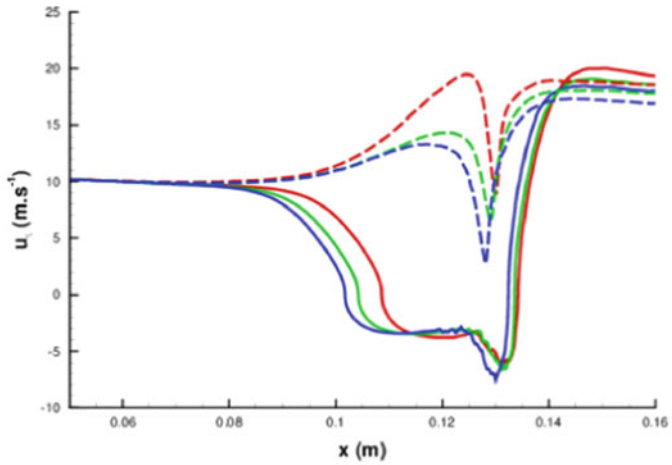

a) Friction velocity

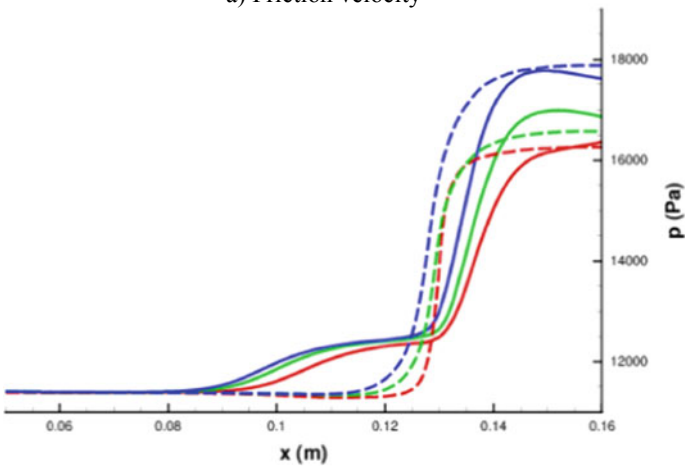

b) Wall pressure

Fig. 74 Influence of the shock deviation angle on the interaction region: 3.5° (red), 4.0° (green), 4.5° (blue). Solid and dashed lines correspond to inflow fluctuation levels of 0.25% and 0.5%, respectively

retained since it results in a separation length of about 30 mm, a dimension that was compatible with was could be inferred from the preliminary experimental set-up.

A refined mesh has then been designed in order to quantify the dependence of the results upon the grid. Cell counts were increased by 40% in the streamwise and spanwise direction and by 20% in the wall-normal direction. Because of the high sensitivity of the transition process to the grid resolution in LES, the inflow perturbation level has been adjusted in order to obtain the same separation length as for the computation from the reference mesh. It allows for comparisons between computations free from transition modelling considerations. However the fluctuation

level had to be dropped by a factor of five to achieve a similar separation length when moving from the reference mesh to the refined one, possibly denoting a change in the numerically-driven physics of the transition process. This point has been addressed by locally increasing the streamwise resolution in the interaction region similarly for the reference and the refined case. It results in an increase of the cell count by about 10% whereas the inflow fluctuation level required for these new meshes to obtain the desired separation length differ by less than 35%, (0.082% of the external velocity for the reference mesh versus 0.061% for the refined mesh). The shape of the separation bubble and the resulting pressure rise obtained from the two meshes are in good concordance, as seen in Fig. 75.

An additional, third mesh has also been derived from the locally-refined reference one by doubling the span of the domain. These three meshes will be hereafter referred to as *reference*, *extended* and *refined* and includes 28 M, 56 M and 67 M cells, respectively.

CFD results

These experimental results are complemented by data coming from the LES performed using the flow parameters and mesh described in previous sectio for a simulated time of 20 *ms*. Such a duration makes it possible to encompass at least 10 periods of the low frequency oscillations, thus allowing spectral analyses of the low-frequency dynamics of the flow with acceptable statistical uncertainties

The streamwise evolution of the premultiplied wall pressure power spectra obtained from the three meshes is plotted in Fig. 76. Note that for each streamwise location the power spectra is normalized by the local value of the pressure variance in order to highlight the *relative* energy contribution of a given frequency range. The three computations results in a similar space–frequency distribution which bears similarities with the experimental power spectra plotted in Fig. 34. The region in the vicinity of the separation point is energetically dominated by the low-frequency content while the energy contained in higher frequency band close to 10 kHz prevails when moving up to the shock impingement location. One can nonetheless note that the typical low frequencies, when normalized using the interaction length and the external velocity, have two– to three–time lower values in the LES than in the experiments.

Influence of the inflow perturbations on the interaction region

Three additional computations have been carried out for each of the three meshes defined in previous section. They correspond to inflow fluctuation levels respectively multiplied by $\alpha_{u'}$ *inflow* $= 3, 5$ *and* 7 with respect to the LES previously described. The statistics have been gathered over 6.25 *ms*, a value large enough for convergence since all these cases yield attached interactions and do not exhibit low-frequency unsteadiness. For all computations the largest cell dimensions in wall unit are encountered in the fully turbulent region downstream of the interaction. Computations based the fine mesh fully fulfill the recommended criteria for LES of turbulent wall bounded flow while for the standard and enlarged meshes values in the wall–normal and streamwise direction are slightly above recommendations in that region ($\Delta y^+_{wall} \simeq 1.6$, $\Delta Z^+ \simeq 22$).

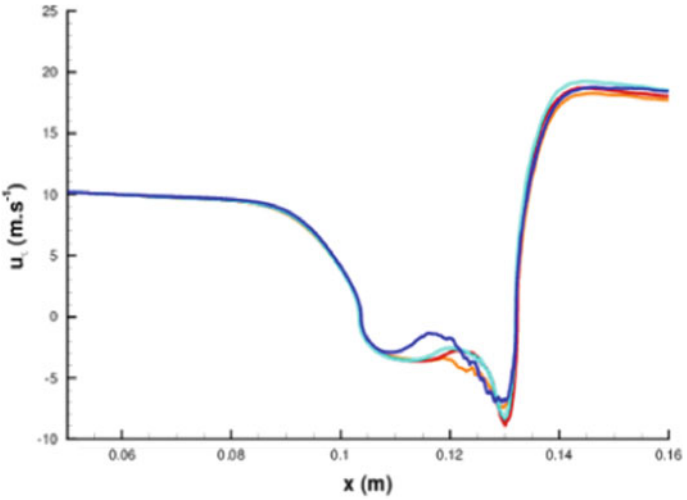

a) Friction

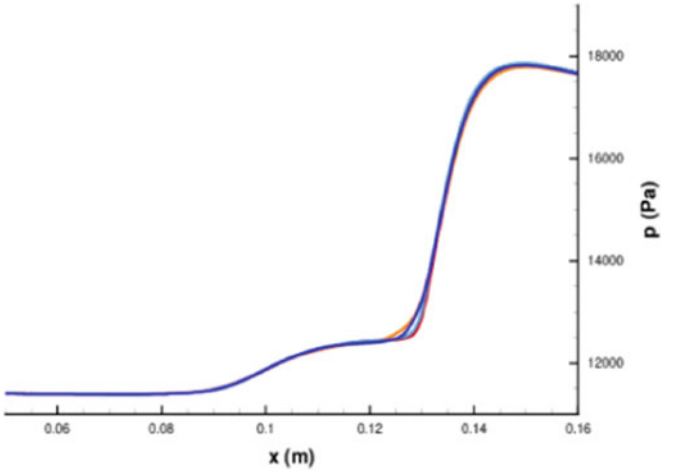

b) Wall pressure

Fig. 75 Influence of the computational grid on the interaction region: initial reference mesh (orange), reference mesh with local streamwise refinement (red), initial refined mesh (cyan) and refined mesh with local streamwise refinement (blue)

Since the scaling on the inflow velocity fluctuation was performed in order to achieve the same separation length for the three meshes, it does not necessarily result in similar locations of the transition for all the meshes when increasing the inflow perturbation level to trigger more upstream transitions. It can however be verified from the streamwise evolution of the compressible shape factor plotted in Fig. 77 that multiplying the reference perturbation level by a value $\alpha_{u'}$ *inflow* common to all three meshes indeed results in very similar transition locations. Moreover, the

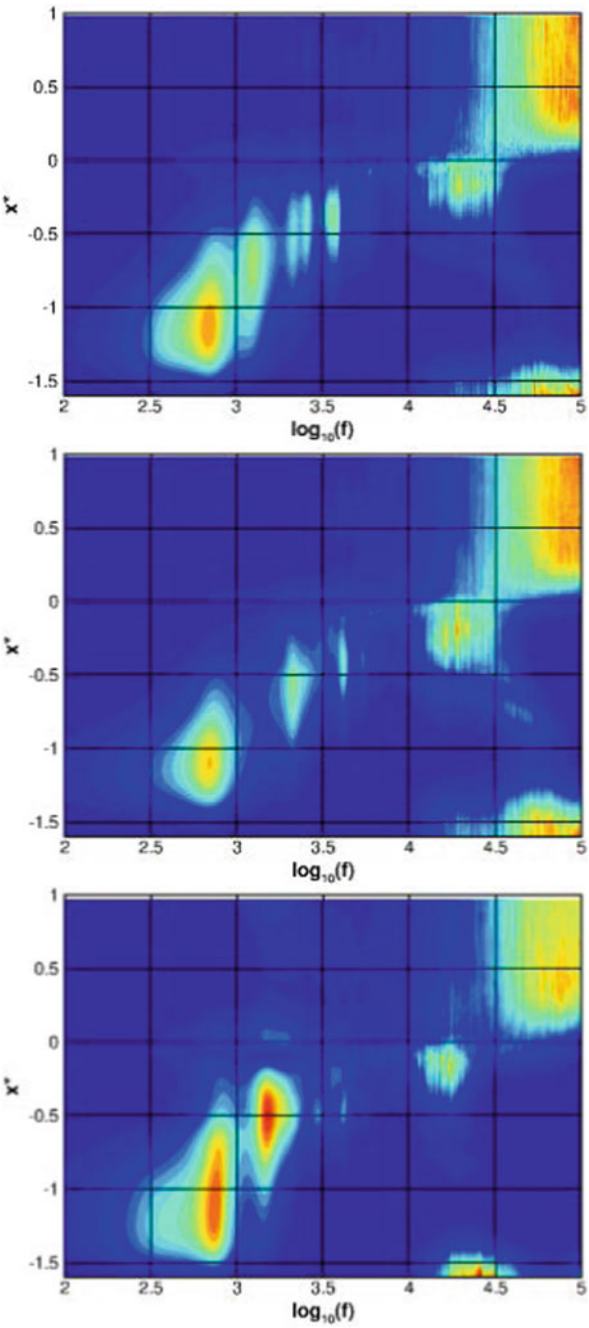

Fig. 76 Streamwise evolution of the pre-multiplied power spectrum of the wall pressure, normalized by the local variance for the reference mesh (left), the extended mesh (middle) and the refined mesh (right)

velocity profiles in wall unit sampled 1 *cm* upstream of the shock impingement, found in the remaining parts of Fig. 77, are in good concordance from one mesh to the other for the three values of $\alpha_{u'inflow}$ that have been tested. The most noticeable differences occur for the two fully turbulent cases above the buffer layer and are due to an underestimation by about 5% of the skin friction coefficient with respect to the fine mesh computations.

The nature of the incoming boundary layer can also be ensured by looking at the streamwise evolution of the skin friction velocity plotted in Fig. 78. These plots

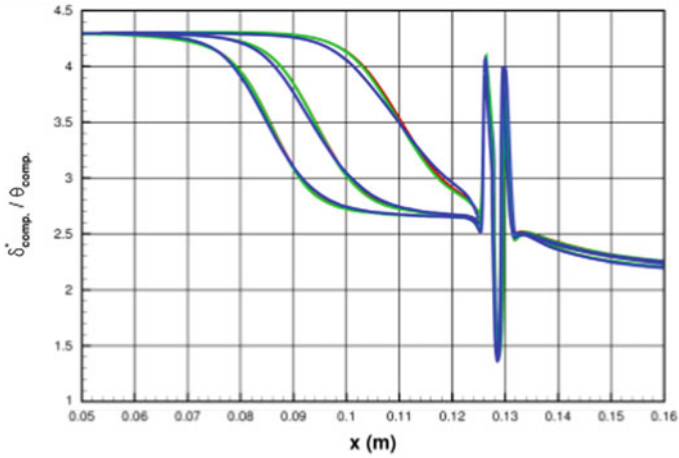

a) Compressible shape factor

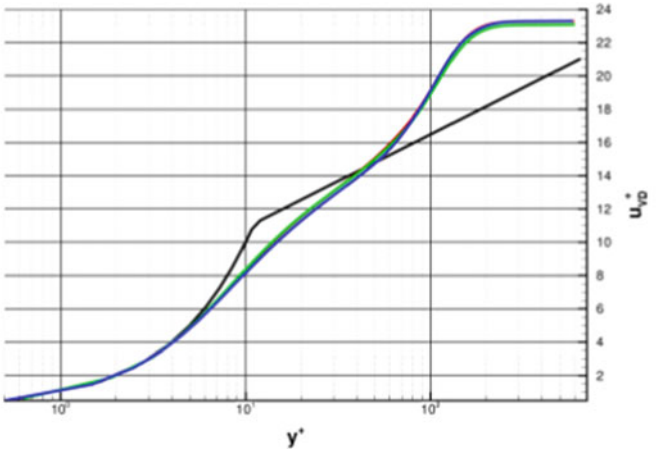

b) Profile for x=0.12 *m*.,

Fig. 77 Assessment of the numerical transition process: reference mesh (red), extended mesh (green) and refined mesh (blue). Results for $\alpha_{u'inflow} = 3$, 5 and 7 have been superimposed

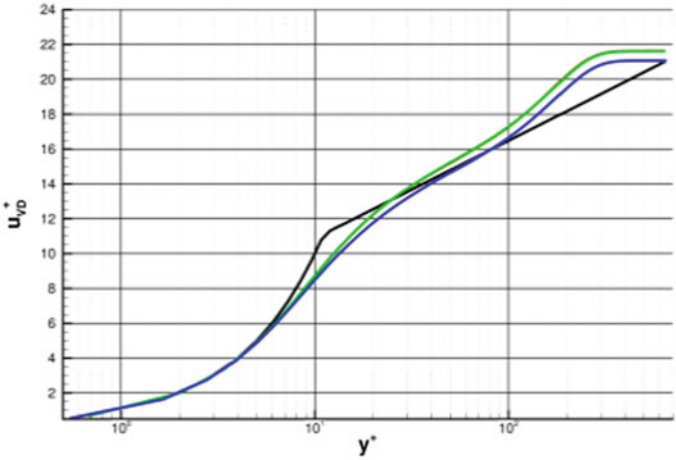

c) Profile for x=0.12

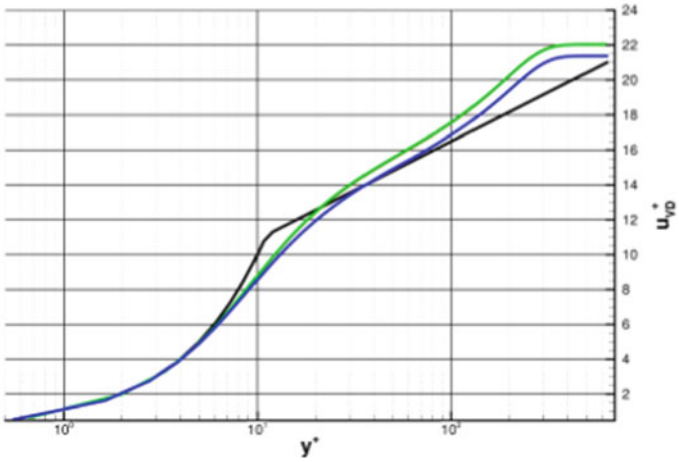

d) Profile for x=0.12 *m.*,

Fig. 77 (continued)

demonstrate that the transitional incoming boundary layer is as capable as the turbulent ones of inducing a reattachment of the flow in the interaction region. This point is confirmed by an additional computation performed using the reference mesh with $\alpha_{u'}$ *inflow* $= 2$, not shown here, which results in an early transitional stage for the incoming boundary layer (the skin friction is increased by 10% with respect to a laminar BL) preventing the flow separation.

It is however interesting to note that in the relaxation region downstream of the interaction, transitional cases result in value of the friction velocity higher by 5 to 10% to the ones obtained for the turbulent cases.

2.3.3 SOTON

Transition Location Effect on SWBLI

The effect of the transition location on the structure of interaction between an oblique shock wave and a boundary-layer at M = 1.5 is investigated. Three different types of interaction, denoted as laminar, transitional and turbulent based on the state of the boundary-layer just upstream of the interaction, have been considered. A naturally

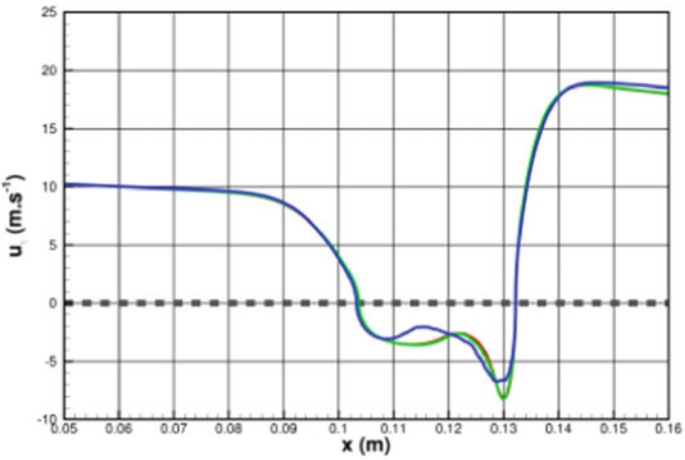

a) $\alpha_{u'inflow} = 1$

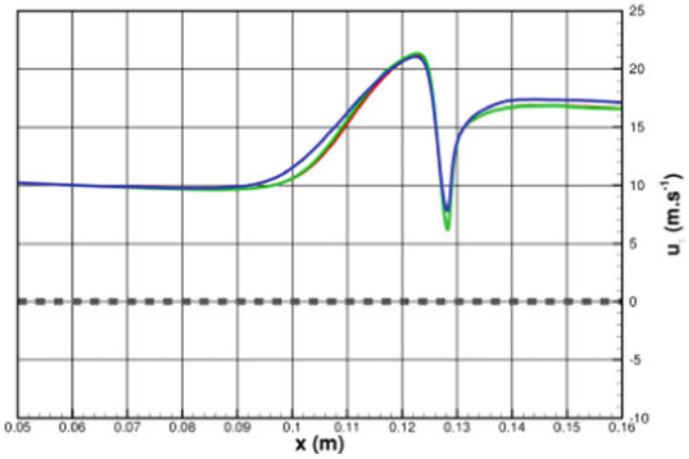

b) $\alpha_{u'inflow} = 3$

Fig. 78 Streamwise evolution of the friction velocity for various perturbation levels at the inflow: reference mesh (red), extended mesh (green) and refined mesh (blue)

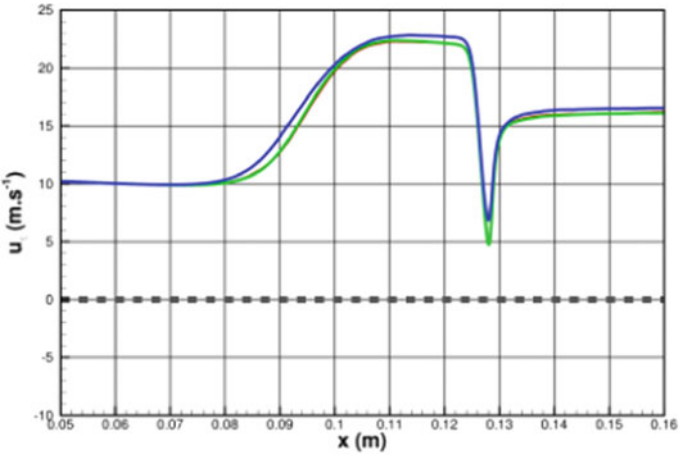

c) $\alpha_{u'inflow} = 5$

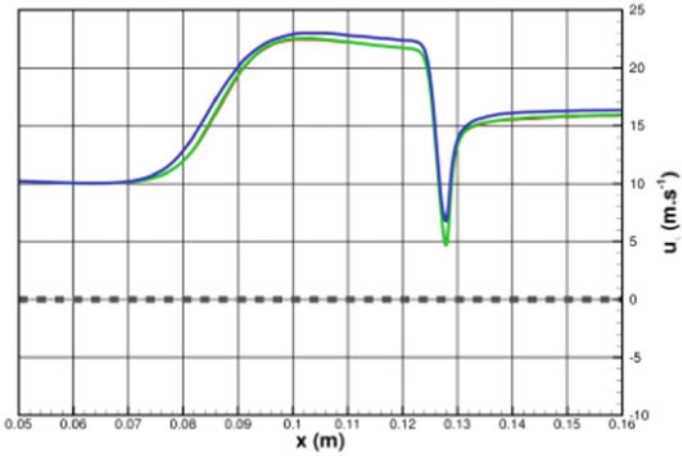

d) $\alpha_{u'inflow} = 7$

Fig. 78 (continued)

transitional boundary-layer can usefully be divided in three main regions (laminar, transitional and turbulent) and in this context a classification of the interaction can be made based on the state of the boundary-layer at the impingement location of the oblique shock wave. The selected laminar, transitional and turbulent interaction cases are based on the set of experiments run at the French aerospace laboratory (Office National d' Etudes et de Recherches A´erospatiales, ONERA), as part of the TFAST project, and modelled numerically by means of DNS. A modal forcing

Table 11 ONERA experimental setup

Exp. Facility	M	T_0 (K)	x_imp (mm)	Reximp $\times 10^6$	P_0 (bar)	θ (deg)
ONERA	1.6	290–310	40–80	0.6–1.1	0.95–1.01	1.5–4

technique is used to promote transition in the boundary-layer and the effects of shock impingement location, shock strength and Reynolds number are investigated.

Experimental Setup

The flow conditions set by the TFAST project in the context of oblique shock reflection on a flat plate consider Mach number between $1.4 - 1.7$, shock impingement Reynolds number Reximp $= (0.4 - 3) \times 10\hat{}6$ and shock generator plate angles of $1 - 4$ deg. The inflow conditions can slightly vary depending on the experimental facility considered. Attention is focused here only on the experiments of ONERA, whose Mach number M, stagnation temperature T_0, stagnation pressure P_0, impingement location x_imp, Reynolds number based on the impingement location Re_ximp and shock generator plate angle θ are reported in Table 11. The intention is to carry out stand-alone DNS calculations in a computationally affordable Reynolds number range, based on the ONERA experiments.

Numerical Setup

The most relevant aspects of the numerical setup are described here. Details on the nature of the forcing, domain size and grid resolution are presented in the following sections.

Inflow Conditions

The inflow conditions are set on the experiments conducted by ONERA. Although the measured Mach number in the experiments is either $M = 1.6$, for consistency with the previous set of simulations the Mach number is $M = 1.5$. For the considered shock strengths, the difference between the numerical and experimental Mach numbers in terms of pressure ratio p3/p1 (downstream of the reflected shock to upstream of the incident shock) is about 1%, therefore no significant effects on the interaction region are expected. The numerical inflow is placed at x_0 = 0.0518 m downstream of the flat plate leading edge where the displacement thickness is $\delta 1{,}0 = 1.84 \times 10\hat{}(-4)$ m. The unit Reynolds number is fixed to Re_1 $= 10.7 \times 10\hat{}6$ m$\hat{} - 1$ and the corresponding Reynolds number based on the displacement thickness at the inlet is Re_δ1,0 = 1971.07. Inflow profiles are given by a similarity solution using the Illingworth transformation. The angle of the shock generator is $\theta = 4$ deg and the oblique shock is introduced by the Rankine-Hugoniot jump relations at the top boundary. For all the selected cases, the free-stream temperature is $T\infty = 197.93$ K and a Sutherland's law is used to describe the variation of viscosity μ with temperature (Sutherland's constant temperature TS = 110.4 K). The integration time step is $\Delta t = 0.015$. All the simulations are run until statistical convergence.

Domain Size, Grid Resolution and Boundary Conditions
While the domain size is kept fixed in the wall-normal (high enough to avoid the reflection of the wave system from the top boundary to impinge onto the boundary-layer) and spanwise (equal to one spanwise wavelength of the most unstable mode and is $Lz = 2\pi/\beta$) directions, the streamwise extent varies depending on the interaction type. The numerical inflow is kept fixed for all the cases studied, whereas the outflow is moved further downstream in order to let the boundary-layer become either transitional or turbulent. When no shock is introduced (ZPG case at $\theta = 0$), the numerical domain corresponds to the one for the turbulent interaction. For each case, the grid distribution in the wall-normal direction is stretched and clusters about 30% of the grid points within the boundary-layer at the inlet. The grid is stretched in the streamwise direction following a 10th-order polynomial distribution whose derivatives are continuous up to the 4th-order. The spatial step size Δx continuously decreases from the inflow up to either the shock impingement or the transition location (whichever comes first), after which uniform grids are used. The grid resolution in the streamwise direction changes depending on the interaction type. While for all the DNS cases, the gridresolution in the transitional/turbulent region is $\Delta x + = 4.8$, $\Delta z + = 4.8$ and $\Delta y +$ wall $= 0.96$. The boundary conditions applied to the computational domain are no-slip and fixed temperature conditions (with temperature equal to the laminar adiabatic wall temperature) at the wall and time-dependent fixed inlet (where the modal forcing is applied). To minimise the reflection of waves into the domain, an integral characteristic method is applied to the top boundary and a standard characteristic boundary condition at the outflow.

Broadband Modal Forcing Technique
The modal forcing represents a very effective way to excite the unstable modes of the boundary-layer and eventually trigger transition. In order to mimic the broadband disturbances in the wind tunnel, the modal forcing is used by selecting a large number of stable and unstable modes. The transition location influences the size of the separation, character of the interaction and, consequently, the boundary-layer instabilities. Since the transition point is not known a priori, it is more convenient to select the boundary-layer unstable modes at the inlet of the numerical domain for the generation of the broadband modal disturbances. For all simulations, 42 eigenmodes are calculated for every combinations of $\omega = 0.02: 0.02: 0.12$ and $\beta = -0.6: 0.2: 0.6$. Since pairs of oblique modes are selected to construct the broadband modal disturbances, random phases are added to each mode in order to avoid any symmetry of the breakdown.

ZPG Boundary-Layer
The classification adopted for the definition of the type of interaction (laminar, transitional and turbulent) assumes a priori knowledge of the transition location. A ZPG boundary-layer is therefore forced with the previously described broadband modal forcing at an amplitude $Ao = 0.05$ (corresponding to a turbulence intensity at the inflow $\rho rms = 0.25\%$), for which transition is obtained approximately halfway down of the numerical domain. The time- and span-averaged skin friction distribution (a), contours of the time-averaged skin friction (b) and instantaneous streamwise velocity at the centreplane (c) reported in Fig. 79 show that transition starts at $Rex = 7 \times 10^5$

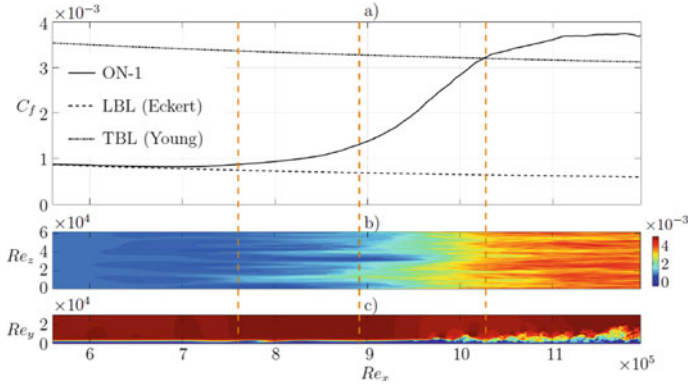

Fig. 79 **a** Time- and span-averaged skin friction distribution for the ZPG boundary-layer (black solid line) along with laminar (dashed-dotted black) and turbulent (dashed black) boundary-layer distributions by Eckert (1955) and Young (1989), respectively; contours of time-averaged skin friction (**b**) and instantaneous streamwise velocity (**c**). The vertical orange dashed lines indicate the shock impingement locations

and the turbulent state is reached at Rex $= 11 \times 10^5$. As seen for bypass transition in incompressible applications (Coupland, 1990, Bhushan and Walters, 2014), an overshoot of the skin friction with respect to theoretical distribution by Young (1989) can be seen at Rex $= 1.02 \times 10^6$ due to the high intensity structures formed during the breakdown to turbulence. The vertical orange dashed lines indicate the shock impingement locations for laminar, transitional and turbulent interactions, respectively. The laminar and turbulent interactions are, in a mean sense, at the boundaries of the transitional region. However, the main transition scenario is a bypass breakdown where intermittent turbulent spots are generated and move the transition point in the streamwise direction. Figure 80 shows the contours of wall-normal vorticity in the vicinity of the wall for three different time levels: t = 7,450 (a), t = 7,900 (b) and

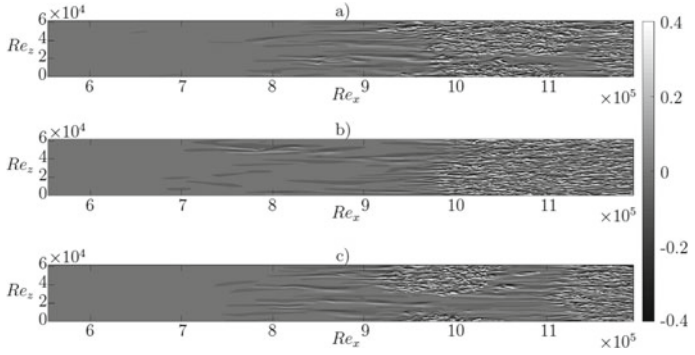

Fig. 80 Contours of wall-normal vorticity for the ZPG boundary-layer at time levels t = 7; 450 (**a**), t = 7; 900 (**b**) and t = 8; 350 (**c**)

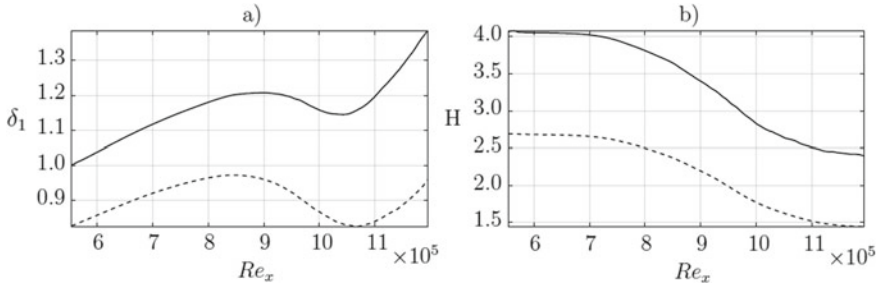

Fig. 81 Time- and span-averaged displacement thickness (**a**) and shape factor (**b**) distributions calculated with the incompressible (dashed lines) and compressible (solid lines) formulations

t = 8,350 (c). The formation of a turbulent spot is visible in Fig. 80c between Rex $= 9 \times 10^5$ and Rex $= 10.5 \times 10^5$. The appearance of the turbulent spots is periodic and localised at around Rez $= 0.1 \times 10^5$ and Rez $= 0.5 \times 10^5$. These preferred locations are due to the choice of the random phases applied to the forcing to avoid a symmetric breakdown. Although random, these phases are fixed throughout the simulation.

Displacement Thickness and Shape Factor Calculations

The state of the boundary-layer can also be examined by calculating the time- and span-averaged displacement thickness and shape factor H (displacement thickness over momentum thickness ratio), as reported in Figs. 81a, b respectively. The kinematic formulation to calculate the displacement thickness and shape factor (dashed lines) is compared with the compressible one (solid lines). When the variable density is not taken into account the shape factor follows the theoretical distributions for incompressible boundary-layers and is about 2.7 near the inlet and 1.5 towards the outlet, in accordance with the laminar and turbulent state. The contribution of compressibility is to shift δ1 and H distributions towards higher values. With reference to the summary of Gatski and Bonnet (2013) on the effects of compressibility on TBLs H-factors, the value obtained in the turbulent region is reasonable for M = 1.5.

Intermittency Calculation

For this bypass-like transition scenario, it can be interesting to measure the intermittency, Γ, to define the state of the boundary-layer. The intermittency is defined as the fraction of time during which the boundary-layer is locally turbulent and typically involves setting arbitrary thresholds on particular measured data. An alternative measure of the intermittency is proposed to avoid problems related to the mean skin friction distribution. Based on the criteria proposed by Volino [48], first time derivatives of the skin friction time series are selected to define the state of the boundary-layer. Low and high fluctuation levels of the time derivatives are related to laminar and turbulent states, respectively. False laminar states, when the first time derivatives of the skin friction cross zero, can be avoided by calculating the second time derivatives of the skin friction. The intermittency is then calculated as the fraction of time during which the first or second time derivatives of the skin friction are

higher than specified thresholds for both ∂Cf/∂t and ∂2Cf/∂t2, respectively. To avoid the need to fix two thresholds, one can iteratively adjust on threshold in order to have the same time average for Γ f and Γ s [48]. The obtained intermittency could then be low-pass filtered in order to smooth the distribution and to prevent false turbulent points in laminar regions or false laminar points in turbulent regions to be captured. However, in the present study no significant differences were found and the filtering is not performed. By visual inspection of the data, the threshold on the first time derivatives is set to be $\Gamma = 6 \times 10^{-5}$. The sensitivity to the selected threshold is studied for $5 \times 10^{-5} < \Gamma < 7 \times 10^{-5}$ and the resulting span averaged intermittency distribution is reported in Fig. 82. The intermittency distribution resulting from the more commonly used criterion proposed by Schneider [49], for which a p.d.f. of the skin friction distribution needs to be calculated (definition A, black solid line with error bars) is compared to the one calculated with the current method (definition B, red solid line with error bars), providing a good agreement and confirming definition B as suitable for both ZPG and SWBLI cases.

SWBLI: Laminar, Transitional and Turbulent Interactions

Laminar, transitional and turbulent interactions are here examined. Time- and span-averaged skin friction distributions are reported in Fig. 83 for the laminar (red solid line), transitional (blue solid line) and turbulent (green solid line) cases. The ZPG boundary-layer solution is also plotted (black solid line) along with the shock impingement locations (vertical orange dashed lines). A first main observation is that when a laminar interaction occurs the boundary-layer separates, whileit remains attached for the turbulent interaction. For the transition case, a marginal separation occurs. As part of the TFAST project, Giepman et al. (2015) report a similar situation for laminar, transitional and turbulent SWBLIs at M = 1.7. While theseparated region is large for the laminar interaction, for the transitional case the zone of reversed flow is strongly reduced and no mean-flow separation is present for the turbulent interaction. The size of the interaction, for example starting where the skin friction deviates from the ZPG boundary-layer distribution and ending with the steep increase downstream

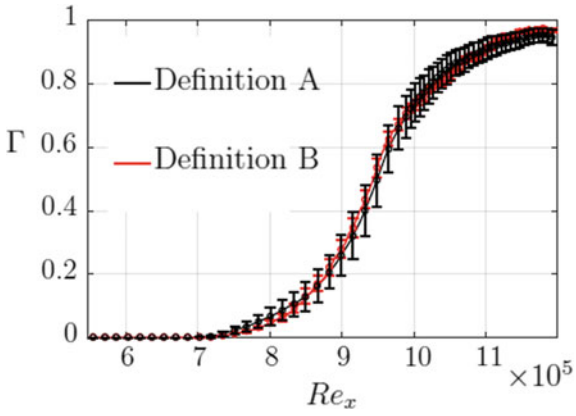

Fig. 82 Sensitivity to the denition for the intermittency calculation (denition A—black solid line, denition B—red solid line)

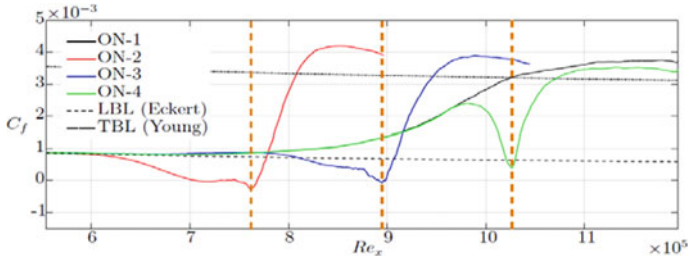

Fig. 83 Time- and span-averaged skin friction distributions for the laminar (red solid line—case ON-2), transitional (blue solid line—case ON-3) and turbulent (green solid line—case ON-4) interactions. The ZPG boundary-layer (black solid line—case ON-1) is also plotted along with laminar (dashed-dotted black) and turbulent (dashed black) boundary-layer distributions by Eckert (1955) and Young (1989), respectively. The vertical orange dashed lines indicate the shock impingement locations

of the impingement, decreases significantly with increasing Reximp. Although only marginally separated, the transitional interaction still presents a relatively large interaction size, which is very narrow in the turbulent case. Another important point, in qualitative agreement with the experiments of Giepman et al. (2015), is that a TBL is detected downstream of the impingement location for the laminar interaction and that transition is accelerated for the transitional and turbulent ones. The shock considered ($\theta = 4°$) is very strong and the boundary-layer becomes turbulent at the shock impingement location. Similarly to what happens to pressure and peak heat transfer distributions in hypersonic applications [50], the skin friction downstream of the impingement location overshoots the fully turbulent skin friction levels of the ZPG case. This is due to the enhanced energy transfer mechanism that precedes the turbulent state downstream of the impingement location. It is also interesting to notice that this overshoot decreases for increasing impingement location Reynolds number.

Displacement Thickness and Shape Factor Calculations

Compressible formulations of the displacement thickness (a) and shape factor (b) are reported in Fig. 84 for the laminar (red solid line), transitional (blue solid line) and turbulent (green solid line) interactions, along with the ZPG boundary-layer solution (black solid line). The APG introduced by the shock causes the appearance of a peak in the boundary-layer displacement thickness and shape factor at the impingement location. Similarly to the interaction size, the peaks get narrower for increasing impingement Reynolds number, allowing these quantities to be used to quantify the interaction size. Differently from the width, the peak value is very sensitive to the way the edge of the boundary-layer is chosen for the calculations of both displacement and momentum thickness. Here, the edge of the boundary-layer is identified by specifying a vorticity threshold, which represents a consistent choice everywhere but at the apex of the separation bubble. The shape factor confirms that the boundary-layer becomes turbulent downstream of the impingement but at a lower level with respect to the ZPG

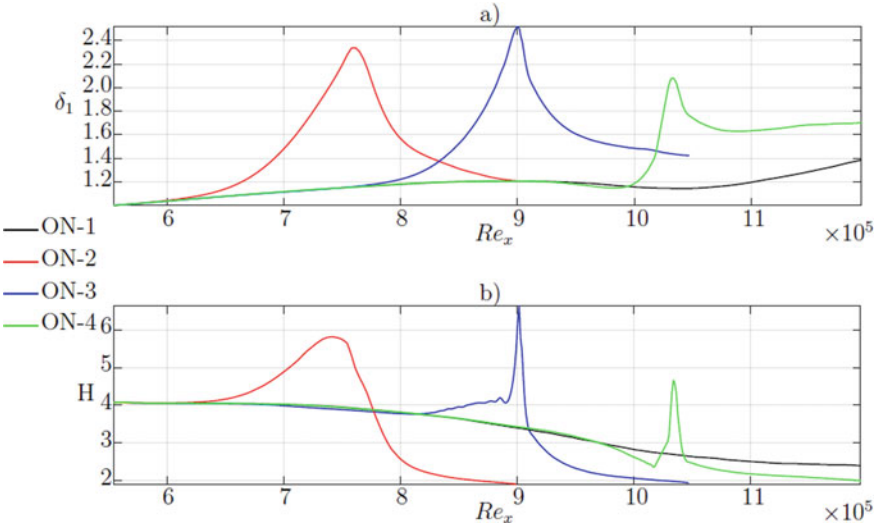

Fig. 84 Compressible displacement thickness (**a**) and shape factor (**b**) distributions for the laminar (red solid line—case ON-2), transitional (blue solid line—case ON-3) and turbulent (green solid line—case ON-4) interactions. The ZPG boundary-layer (black solid line—case ON-1) is also plotted

case, due to the TBL downstream of the impingement that is always significantly thicker than the case without shock.

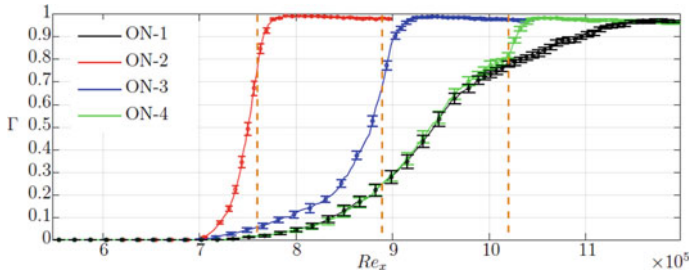

Fig. 85 DNS span averaged intermittency distributions (with error bars due to the threshold sensitivity) for the laminar (red solid line—case ON-2), transitional (blue solid line—case ON-3) and turbulent (green solid line—case ON-4) interactions. The ZPG boundary-layer (black solid line—case ON-1) is also plotted. The vertical orange dashed lines indicate the shock impinge-ment locations

Intermittency Calculation

Definition B is used to calculate the intermittency distributions for the laminar (red solid line), transitional (blue solid line) and turbulent (green solid line) in Fig. 85, where the sensitivity of the distributions to the threshold ($5 \times 10^{-5} < f < 7 \times 10^{-5}$) is indicated by the error bars. Similarly to what was observed from the skin friction and shape factor distributions, the intermittency distributions show a sharp increase towards unity downstream of the impingement location due to the turbulent character of the boundary-layer.

Upstream of the impingement, the effect of the shock-wave differs significantly depending on the interaction type. For the laminar interaction, the boundary-layer quickly switches from being laminar to turbulent when passing across the shock and this causes a very localised change of the intermittency. The transitional interaction affects the boundary-layer for a longer upstream extent and the increase of intermittency is more gradual. Although the boundary-layer is marginally separated, the presence of the interaction changes the instability of the boundary-layer and the Γ distribution deviates from the ZPG distribution. This also happens for the turbulent case but with less significant consequences since the size of the interaction is much smaller. The upstream response of the boundary-layer to the turbulent interaction is almost negligible and the major effects are only visible downstream of the impingement.

References

1. T.S.C. Davidson, H. Babinsky, An investigation of interactions between normal shocks and transitional boundary layers—control ID 1889354. *44th AIAA Fluid Dyn. Conf.*, no. June, pp. 1–16 (2014)
2. S.P. Colliss, Vortical structures on three-dimensional shock control bumps (2014)
3. N. Titchener, S. Colliss, H. Babinsky, On the calculation of boundary-layer parameters from discrete data. Exp. Fluids **56**(8), 1–18 (2015)
4. C. Sun, M.E. Childsf, A Modified Wall Wake Velocity Profile for Turbulent Compressible Boundary Layers, no. June, pp. 7–9 (1973)
5. T.B. Layer, Explicit Expression for the Smooth Wall Velocity Distribution in a Turbulent Boundary Layer, no. June, pp. 655–657 (1979)
6. T.S.C. Davidson, H. Babinsky, Influence of Boundary-Layer State on Development Downstream of Normal Shock Interactions, pp. 10–12
7. L.U. Schrader, L. Brandt, C. Mavriplis, D.S. Henningson, Receptivity to free-stream vorticity of flow past a flat plate with elliptic leading edge. J. Fluid Mech. **653**, 245–271 (2010)
8. J. Ackeret, F. Feldmann, N. Rott, Investigations of compression shocks and boundary layers in gases moving at high speed, *NACA Rep.*, no. 1113 (1947)
9. J.W. Kooi, Experiment on transonic shock wave boundary layer interaction, *AGARD Flow Sep.* (1975)
10. W.G. Sawyer, C.J. Long, A study of normal shock-wave turbulent boundary-layer interactions at mach numbers of 1.3, 1.4 and 1.5, *Tech. Rep. 82099, NASA* (1982)
11. S. Pirozzoli, P. Orlandi, M. Bernardini, The fluid dynamics of rolling wheels at low Reynolds number. J. Fluid Mech. **706**(July), 496–533 (2012)
12. S. Pirozzoli, M. Bernardini, F. Grasso, Direct numerical simulation of transonic shock/boundary layer interaction under conditions of incipient separation. J. Fluid Mech. **657**, 361–393 (2010)

13. S. Pirozzoli, Generalized conservative approximations of split convective derivative operators. J. Comput. Phys. **229**(19), 7180–7190 (2010)
14. M. Bernardini, S. Pirozzoli, A general strategy for the optimization of Runge-Kutta schemes for wave propagation phenomena. J. Comput. Phys. **228**(11), 4182–4199 (2009)
15. E.A. Fadlun, R. Verzicco, P. Orlandi, J. Mohd-Yusof, Combined immersed-boundary finite-difference methods for three-dimensional complex flow simulations. J. Comput. Phys. **161**(1), 35–60 (2000)
16. M.D. de Tullio, P. De Palma, G. Iaccarino, G. Pascazio, M. Napolitano, An immersed boundary method for compressible flows using local grid refinement. J. Comput. Phys. **225**(2), 2098–2117 (2007)
17. M. Alam, N.D. Sandham, Direct numerical simulation of 'short' laminar separation bubbles with turbulent reattachment. J. Fluid Mech. **410**, 1–28 (2000)
18. P.R. Spalart, M.K. Strelets, Mechanisms of transition and heat transfer in a separation bubble. J. Fluid Mech. **403**, 329–349 (2000)
19. S. Pirozzoli, M. Bernardini, F. Grasso, Characterization of coherent vortical structures in a supersonic turbulent boundary layer. J. Fluid Mech. **613**, pp. 205–231 (Oct. 2008)
20. S. Pirozzoli, F. Grasso, Direct numerical simulation of impinging shock wave/turbulent boundary layer interaction at M = 2.25, *Phys. Fluids* **18**(6) (2006)
21. P. Moin, K. Mahesh, Direct numerical simulation: a tool in turbulence research, Annu. Rev. Fluid Mech. **30**(1), pp. 539–578 (Jan. 1998)
22. J. Delery, J.G. Marvin, Shock wave—boundary layer interactions (1986)
23. E. Katzer, On the lengthscales of laminar shock/boundary-layer interaction, **206** (1989)
24. B.I. Greber, R.J. Hakkinen, L. Trilling, laminar boundary layer oblique shock wave interaction on flat and curved plates 1, **33**, pp. 312–331
25. R. Dp, B. Or, R. Jenson, Triple-deck solutions for viscous supersonic and l o w past corners hypersonic f, **89** (1978)
26. D.R Chapman, D.M Kuehn, H.K Larson, Investigation of separated flows in supersonic and subsonic streams with emphasis on the effect of transition (1957)
27. R.H.M. Giepman, F.F.J. Schrijer, B.W. van Oudheusden, High-resolution PIV measurements of a transitional shock wave–boundary layer interaction. Exp. Fluids **56**(6), 1–20 (2015)
28. R.H.M. Giepman, F.F.J. Schrijer, B.W. van Oudheusden, Infrared thermography measurements on a moving boundary-layer transition front in supersonic flow. AIAA J. **53**(7), 2056–2061 (2015)
29. S. Dhawan, R. Narasimha, Some properties of boundary-layer flow during the transition from laminar to turbulent motion. J. Fluid Mech. **3**(1951), 418–453 (1958)
30. P.R. Spalart, S. Deck, M.L. Shur, K.D. Squires, M.K. Strelets, A. Travin, A new version of detached-eddy simulation, resistant to ambiguous grid densities. Theor. Comput. Fluid Dyn. **20**(3), 181 (2006)
31. P. Spalart, S. Allmaras, A one-equation turbulence model for aerodynamic flows. *AIAA*, **439** (1992)
32. F.R. Menter, Two-equation eddy-viscosity turbulence models for engineering applications, **32**(8) (1994)
33. K.-Y. Chien, Predictions of channel and boundary-layer flows with a low-reynolds-number turbulence model. AIAA J. **20**(1), pp. 33–38 (Jan. 1982)
34. R. Bourguet, M. Braza, G. Harran, R. El Akoury, Anisotropic organised eddy simulation for the prediction of non-equilibrium turbulent flows around bodies. J. Fluids Struct. **24**(8), 1240–1251 (2008)
35. D.M. Dawson, S.K. Lele, J. Bodart, Assessment of wall-modeled large eddy simulation for supersonic compression ramp flows. In *49th AIAA/ASME/SAE/ASEE Joint Propulsion Conference*, American Institute of Aeronautics and Astronautics (2013)
36. S. Hickel, E. Touber, J. Bodart, J. Larsson, A parametrized non-equilibrium wall-model for large-eddy simulations (2015)
37. M. Shur, P. Spalart, M. Strelets, A. Travin, A hybrid RANS-LES approach with delayed-DES and wall-modelled LES capabilities. Int. J. Heat Fluid Flow **29**, 1638–1649 (2008)

38. E. Touber, N.D. Sandham, Low-order stochastic modelling of low-frequency motions in reflected shock-wave/boundary-layer interactions. J. Fluid Mech. **671**, 417–465 (2011)
39. L. Agostini, L. Larchevêque, P. Dupont, J. Debiève, J.-P. Dussauge, Zones of influence and shock motion in a shock/boundary-layer interaction. AIAA J. **50**(6), 1377–1387 (2012)
40. P. Durbin, X. Wu, Transition Beneath Vortical Disturbances (2007)
41. L. Agostini, L. Larchevêque, P. Dupont, L. Agostini, L. Larchevêque, P. Dupont, Mechanism of shock unsteadiness in separated shock/boundary-layer interactions Mechanism of shock unsteadiness in separated shock/boundary-layer interactions, **126103** (2015)
42. J. Riou, E. Garnier, C. Basdevant, Compressibility effects on the vortical flow over a 65° sweep delta wing. Phys. Fluids **22**(3), 2–13 (2010)
43. E. Garnier, Stimulated Detached Eddy Simulation of three-dimensional shock/boundary layer interaction, pp. 479–486 (2009)
44. P. Roe, Approximate riemann solvers, parameter vectors, and difference schemes. J. Comput. Phys. **43**(2), pp. 357–372 (Oct. 1981)
45. F. Ducros et al., Large-eddy simulation of the shock/turbulence interaction, **549**, pp. 517–549 (1999)
46. E. Lenormand, P. Sagaut, Subgrid-scale models for large-eddy simulations of compressible wall bounded flows, **38**(8) (2000)
47. C.W. Gear, *Numerical Initial Value Problems in Ordinary Differential Equations* (Prentice Hall PTR, Upper Saddle River, NJ, USA, 1971)
48. R.J. Volino, M.P. Schultz, C.M. Pratt, Conditional sampling in a transitional boundary layer under high freestream turbulence conditions. J. Fluids Eng. **125**(1), pp. 28–37 (Jan. 2003)
49. S.P. Schneider, Improved methods for measuring laminar-turbulent intermittency in boundary layers. Exp. Fluids **18**(5), 370–375 (1995)
50. H. Babinsky, J.K. Harvey, Shock Wave-Boundary-Layer Interactions (2011)